


UNIVERSITÀ DEGLI STUDI DI MILANO &
UNIVERSITÀ CATTOLICA DEL SACRO CUORE

SCUOLA DI DOTTORATO IN
FISICA, ASTROFISICA E FISICA APPLICATA

DIPARTIMENTO
MATEMATICA E FISICA

DOTTORATO DI RICERCA IN
FISICA, ASTROFISICA E FISICA APPLICATA
Ciclo XXIII

Growth and characterization of epitaxial and cluster-assembled Cr-N doped TiO_2 with enhanced visible-light photoactivity

Settore scientifico disciplinare FIS/03

Tesi di Dottorato di:
Mirco Chiodi
Matricola: R07881

Coordinatore: Prof. Marco Bersanelli
Tutore: prof. Luca Gavioli

A.A. 2009-2010

to anyone who may be reading this,

and especially to myself

"An expert is a man who has made all the mistakes which can be made in a very narrow field"

- Niels Bohr

"If I could explain it to the average person, I wouldn't have been worth the Nobel Prize"

"The first principle is that you must not fool yourself and you are the easiest person to fool."

- Richard Feynman

TABLE OF CONTENTS

1.1 Introduction

The current global energy consumption is around 13 terawatts (TW) per year and most of it comes from fossil fuel [Slaoui2007, DOE2005]. With this consumption rate, the reserves of oil, natural gas and coal will last only for 30, 60 and 200 years, respectively [Dresselhaus2001]. Unfortunately, the demand of energy will grow quickly and is forecast to reach a value of 30 TW by 2050 [Slaoui2007, DOE2005], which means that the energy sources will deplete even sooner. Although there is no worry of losing energy supplies immediately, the dominance of fossil fuel as energy supply has to be changed eventually. One of the biggest concerns for our society is to find alternative energy sources before fossil fuels are depleted.

Both nuclear power and solar power have the potential to provide huge amount of energy, but nuclear power is limited by mineral isotope conserves and safety concerns about nuclear reactions. It appears that solar energy would be the only energy source with the potential of fulfilling the increasing demand of energy in the long run.

The Sun supply the earth surface with ~125000 TW (i.e. $1.25 \cdot 10^{17}$ Watts) annually [Slaoui2007], which greatly exceeds the capacity of any energy resource on earth. The current annual global energy consumption only accounts for the amount of energy delivered to the earth by the sun in 1 hour. Therefore, solar energy has the potential to meet the energy demand of human society. However, the solar energy is quite unevenly distributed on the surface of the earth and efficient collection is still a technological challenge. The widely used approaches to capture solar energy are summarized in Fig.1. The major strategies to utilize solar energy are to convert the incident sunlight into either electricity or chemical fuels. Two major techniques are available to generate electricity from sunlight. The first technique involves direct conversion of incident photons into electricity,[Slaoui2007] which can be achieved through device called photovoltaic (PV), or more commonly known as solar cells. The second route uses the heat from the sun to generate electricity with the help of thermoelectric (TE) devices [Crabtree2007]. Besides electricity generation, sunlight is

also considered to be an energy source to provide chemical fuels. Biological systems exploit this fact through natural photosynthesis. With the aid of solar light, semiconductor photocatalysts are also able to produce chemical fuels through heterogeneous chemical reactions on the surface of these materials [Nozik1996, Linsebigler1995].

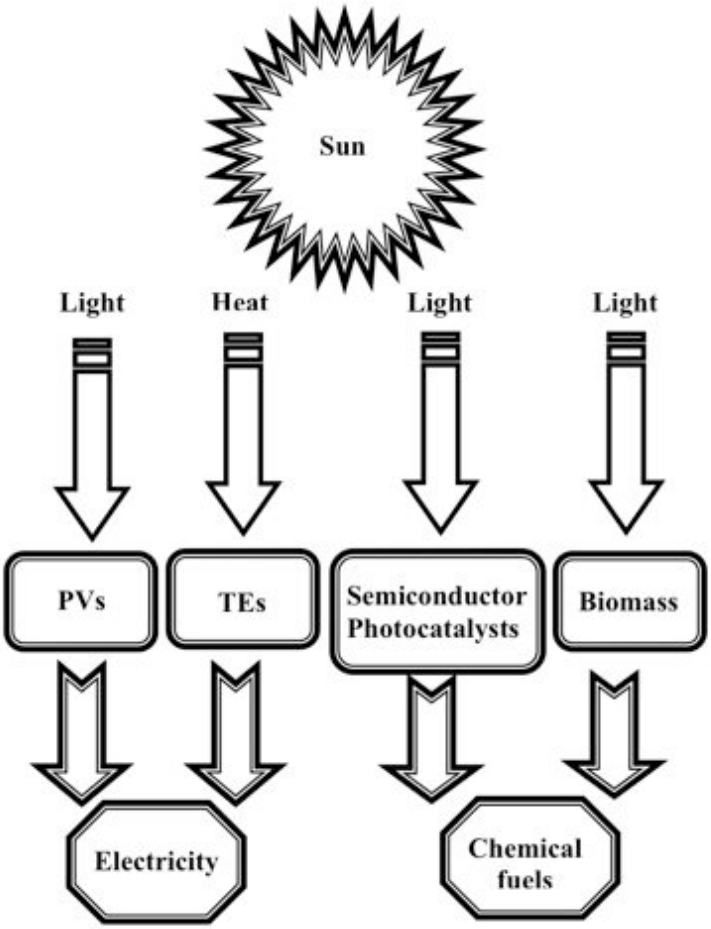

Figure 1 – Schematic representation of currently used solar energy conversion approaches (PVs= Photovoltaics and TEs= Thermoelectrics)

Even if solar energy is free and abundant, photovoltaic technology represents only around 0.04% of the fuel share of world's total primary energy supply [IEA-OECD2007]. Nowadays, the most widely used PV solar cells are silicon wafer-based solar cells (thick cells of around 150–300 nm made of crystalline or amorphous silicon). This technology,

classified as the first-generation of photovoltaic cells, accounts for more than 86% of the global solar cell market. The second generation of photovoltaic materials is based on the introduction of a series of thin film layers (1–2 nm each) of semiconductor materials. More specifically, they use thin epitaxial deposits of semiconductors on lattice-matched wafers. These cells comprise around 90% of the market space but only a small segment of the global PV market. Unfortunately, although a lower manufacturing cost is achieved, it also involves low conversion efficiencies.

The main limitation to a progressive substitution of fossil fuels by solar energy is the cost of the energy conversion devices. In fact, even if continuous advances in PV have made its cost fall below 0.2 – 0.3 $/kWh in 2007, the cost of coal-based electricity is still far below that value: 0.04 $/kWh [Slaoui2007]. Undoubted, solar-based devices still need to improve significantly to compete with machines powered by fossil fuels. On the other hand, currently available approaches to produce chemical fuels by using solar energy are not able to make use of solar energy efficiently: the most of semiconductor photocatalysts can only utilize less than 5% of the energy from sunlight. Therefore, there is a constantly increasing number of research groups studying possible ways to enhance the global efficiency of photo-active materials for energy conversion applications. Among the others, titanium dioxide TiO_2 proved to be one of the most promising for several photo-assisted applications such as photovoltaics and photocatalysis [Diebold2003].

1.2 Titanium dioxide (TiO_2)

1.2.1 General remarks

Titanium dioxide (TiO_2) belongs to the family of transition metal (TM) oxides. In the beginning of the 20th century, industrial production started with titanium dioxide replacing toxic lead oxides as pigments for white paint. At present, the annual

production of TiO_2 exceeds 4 million tons [Natara1998]. It is used as a white pigment in paints (51% of total production), plastic (19%), and paper (17%), which represent the major end-use sectors of TiO_2. The consumption of TiO_2 as a pigment increased in the last few years in a number of minor end-use sectors such as textiles, food (it is approved in food-contact applications and as food coloring (E-171) under a EU legislation on the safety of the food additives [Philips1997]), leather, pharmaceuticals (tablet coatings, toothpastes, and as a UV absorber in sunscreen cream with high sun protection factors [Schultz2002] and other cosmetic products), and various titanate pigments (mixed oxides such as $ZnTiO_3$ [Cord1971], $ZrTiO_4$ [Parker1990], etc).

TiO_2 has received a great deal of attention due to its chemical stability, non-toxicity, low cost, and other advantageous properties. As a result of its high refractive index, it is used as anti-reflection coating in silicon solar cells and in many thin-film optical devices [Macleod1986]. TiO_2 is successfully used as gas sensor (due to the dependence of the electric conductivity on the ambient gas composition [Kumazawa1999]) and is utilized, for example, in the determination of oxygen [Logothetis1980] and CO [Savage2001] concentrations at high temperatures (>600°C). Due to its compatibility with the human body, TiO_2 is used as a biomaterial (as bone substituent and reinforcing mechanical supports) [Poluncheck2000].

TiO_2 is also used in catalytic reactions acting as a promoter, a carrier for metals and metal oxides, an additive, or as a catalyst. Reactions carried out with TiO_2 catalysts include selective reduction of NO_x to N_2 [Vedrine2000], effective decomposition dioxins and chlorinated compounds [Weber1999], hydrogen production by gas shift production [Boccuzzi2002], CO oxidation by O_2 [Fan2003] and NO_2 storage [Despres2003]. Rutile TiO_2 is investigated as a dielectric gate material for MOSFET devices as a result of its high dielectric constant ($\varepsilon > 100$) [Li2000] and doped anatase films might be used as a ferromagnetic material in spintronics [Chambers2001]. In batteries, the anatase form is used as an anode material in which lithium ions can intercalate reversibly [Kavan1999]. For solar cell applications, the anatase structure is usually preferred over the rutile structure, as anatase exhibits a higher electron mobility, lower dielectric constant, lower

density, and lower deposition temperature. Nanostructured TiO_2 is extensively studied in the field of solar cells. Other photochemical and photophysical applications include photolysis of water, light-assisted degradation of pollutants, specific catalytic reactions, and light-induced superhydrophilicity. This list of applications is far from complete and new ideas concerning the possible use of TiO_2 have been appearing regularly.

1.2.2 Crystal structures and properties

There are three major types of TiO_2 structures: rutile, anatase and brookite. Other structures exist as well, for example cotunnite TiO_2 has been synthesized at high pressures and resulted to be one of the hardest polycrystalline materials known [Dubrovinsky2001]. However, only rutile and anatase play any role in the applications of TiO_2 and appear to be of any interest for our study.

The structures of both rutile and anatase can be discussed in terms of TiO_2^{6-} octahedrals [Carp2004]. In fact anatase can be regarded as being built up from octahedrals connected by their vertices, while in rutile the edges are connected (see Fig.2).

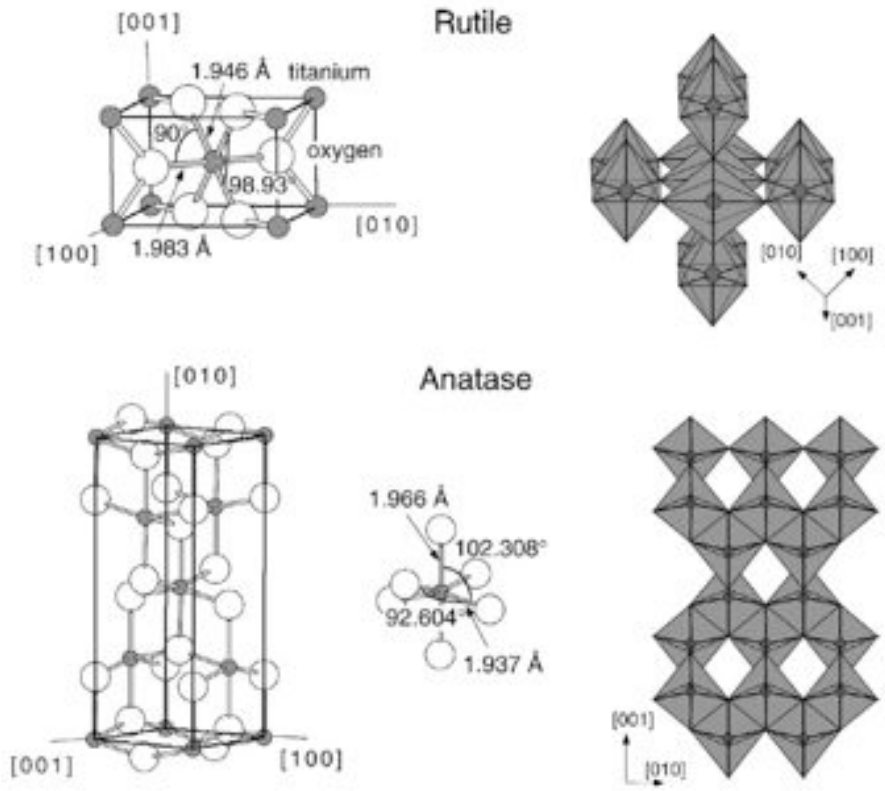

Figure 2 – Bulk structures of rutile and anatase. Slightly distorted octahedral are the basic building blocks for both structures, as can be seen on the right side.

Thermodynamic calculations predict that rutile is the most stable phase at all temperatures [Norotsky1967]. Nonetheless, the thermodinamical stability of the other crystal structures is very similar, suggesting that the metastable polymorphs are almost as stable as rutile at standard pressures and temperatures. This also implies that anatase is kinetically stable, i.e. its transformation into rutile at room temperature is so slow that practically does not occur. At macroscopic scale, the transformation reaches a measurable speed only beyond 600°C [So2001]. Moreover, a size-dependence of the stability of these two TiO_2 structures has been reported [Zhang2000]. At the same temperature, rutile is the most stable phase for larger nanocrystals (i.e. above 35 nm in size), while anatase is the most stable for smaller ones (below 11 nm). Such behavior has been explained as originating from surface-energy effects (surface free energy and

surface stress, which depend on the particle size) [Zhan1998]. It has been frequently reported that these two structures exhibit also different activities for photocatalytic reactions. But the precise reasons for differing photoactivities have not been elucidated in detail yet [Fujishima2008, Diebold2003].

The anatase-to-rutile conversion has been studied extensively, because the TiO_2 phase is one of the crucial parameters determining the use as a photocatalyst, catalyst or ceramic membrane material [Kumar1999, Linsebigler1995, Kumar1993]. This transformation, achieved by increased temperature (or pressure), is influenced by several factors, such as:

Concentration of lattice and surface defects, which mainly depend on the synthesis method and the eventual presence of dopants [Chao2003, Sali2009]. An increase of defects, such as oxygen vacancies, enhances the rutile transformation rate, as they act like nucleation sites. Moreover, the stoichiometry of TiO_2 can be controlled by the nature, amount and lattice-adopted positions of impurities. Interstitial ions decrease the concentration of oxygen vacancies and inhibit the transformation, whereas substitutional cations, depending on their oxidation state, can inhibit or accelerate the transformation. Ions with valency less than four and having small radius in substitutional positions (e.g., Cr^{3+}, Cu^{2+}, Co^{2+}, Li^{+}, Fe^{3+}, Mn^{2+}) are found to increase the oxygen vacancy concentration, which presumably reduces the strain energy, which must be overcome before a structural rearrangement can occur [Karvinen2003]. On the other hand, Sa Li recently reported a quite surprising rutile-to-anatase conversion at temperatures beyond 500 °C upon TM doping, suggesting that the more work is still needed to fully characterize the role played by metallic dopants inside the different TiO_2 lattices.

Particle size. From a physical point of view, the conversion temperature and the rate of transformation depend on how fast the primary particles in the

anatase phase sinter together to reach the critical size [Wang1999]. From circumstantial evidence, it is expected that the critical nucleus size of rutile crystallites is at least three times larger than that of anatase. This means that if sintering of anatase particles is retarded by a suitable technique (e.g., synthesis methods [Izutsu1997], or addition of certain compounds like ZrO_2 or SiO_2 [Zhang2002], which prevent anatase particles from adhering together), the probability of reaching the critical nucleus size is lowered, delaying the transformation, and stabilizing anatase at high temperatures. On the other hand, smaller grain sizes are usually associated with higher specific surfaces. In these conditions, the total boundary energy of the TiO_2 powder increases, the driving force for rutile grain growth increases, and the conversion of anatase to rutile is promoted. Once the critical particle size is achieved using nanosized anatase as starting material, the transformation reaches a measurable speed at lower temperatures (T>400°C) [Gouma1999].

Some of the most important bulk properties of TiO_2 are presented in Table A.

Crystal structure	System	Space group	Lattice constants (nm)			
			a	*b*	*c*	*c*/*a*
Rutile	Tetragonal	D_{4h}^{14}-$P4_2/mmm$	0.4584	–	0.2953	0.644
Anatase	Tetragonal	D_{4h}^{19}-$I4_1/amd$	0.3733	–	0.937	2.51
Brookite	Rhombohedral	D_{2h}^{15}-Pbca	0.5436	0.9166	–	0.944
Density (kg/m^3)						
Rutile	4240					
Anatase	3830					
Brookite	4170					
Dielectric properties	Frequency (Hz)	Temperature (K)	Dielectric constant			
Rutile, perpendicular to optical *c*-axis	10^8	290–295	86			
Rutile, parallel to optical *c*-axis	–	290–295	170			
Rutile, perpendicular to optical *c*-axis	10^4	298	160			
Rutile, along *c*-axis	10^7	303	100			
Anatase, average	10^4	298	55			
Band gap (eV)						
Rutile	3.05					
Anatase	3.26					
Refractive index	n_g	n_p				
Rutile	2.9467	2.6506				
Anatase	2.5688	2.6584				
Brookite	2.809	2.677				

Table A – Some of the most notable bulk properties of the main TiO_2 polymorphs (anatase, rutile and brookite) [Carp2004]

1.2.3 Electronic properties

In a solid, the energy distribution of electronic levels is described by the band model. A large number of electronic levels is formed as the atomic orbitals interact with each other. The resulting electronic levels are closely packed, forming a continuum often referred as electronic bands [Eyring1970]. The band in which electrons are free to flow and conduct electricity is called the conduction band (CB) and the levels completely

occupied by the electrons are the valance band (VB). The energy difference between these bands is called the bandgap, E_g. A schematic diagram of the electronic structure of an insulator, a semiconductor and a conductor is given in Fig.3.

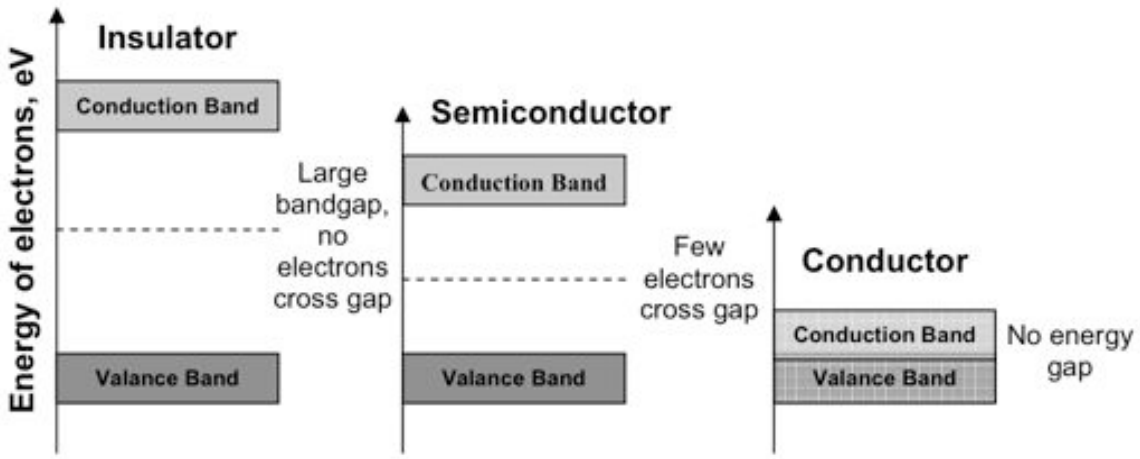

Figure 3 – Typical band structures exhibited by insulators (left), semiconductors (center) and metals (right).

In metals, there is a continuum of electronic states and valance electrons move freely to conduct electricity. A bandgap exists between the *VB* and the *CB* in semiconductors and insulators. The large bandgap in insulators does not allow electrons injection into the *CB* and electrons in a completely filled band do not conduct electricity. Semiconductors, however, absorb light below the fundamental absorption edge (λ_g) to inject electrons into the *CB,* simultaneously generating holes (electron deficiencies) in the *VB*. The fundamental interband absorption wavelength λ_g can be related to the bandgap energy through this empirical relationship [Grätzel1989]:

$$\lambda_g \text{ (nm)} = 1240/E_g \text{ (eV)}$$

Thus, the E_g of a semiconductor can be determined by means of optical absorption,

measuring at which wavelength the photons start to be absorbed by the system due to the fundamental interband excitation.

The presence of impurities, such as different atomic species injected inside the original semiconductor matrix, or structural defects (i.e. vacancies, dislocations. grain boundaries, etc.) can perturb the electronic structure possibly donating electrons to the *CB* [Morrison1980]. These perturbations give rise to new energy levels to produce *n*-type and *p*-type semiconductors. In an *n*-type semiconductor, electrons are the majority carrier, while in a *p*-type semiconductor holes are the majority carrier. TiO_2 (like, for example, ZnO, WO_3 and Fe_2O_3,) is naturally an *n*-type semiconductor while Cu_2O, NiO or Cr_2O_3 are naturally *p*-type semiconductors. In general this property can be partially modified introducing selected atomic impurities to tune the electronic structure of the semiconductor, this procedure is know as *doping* [Lindgren2004]. The bandgap values of some semiconductors are presented in Fig.4.

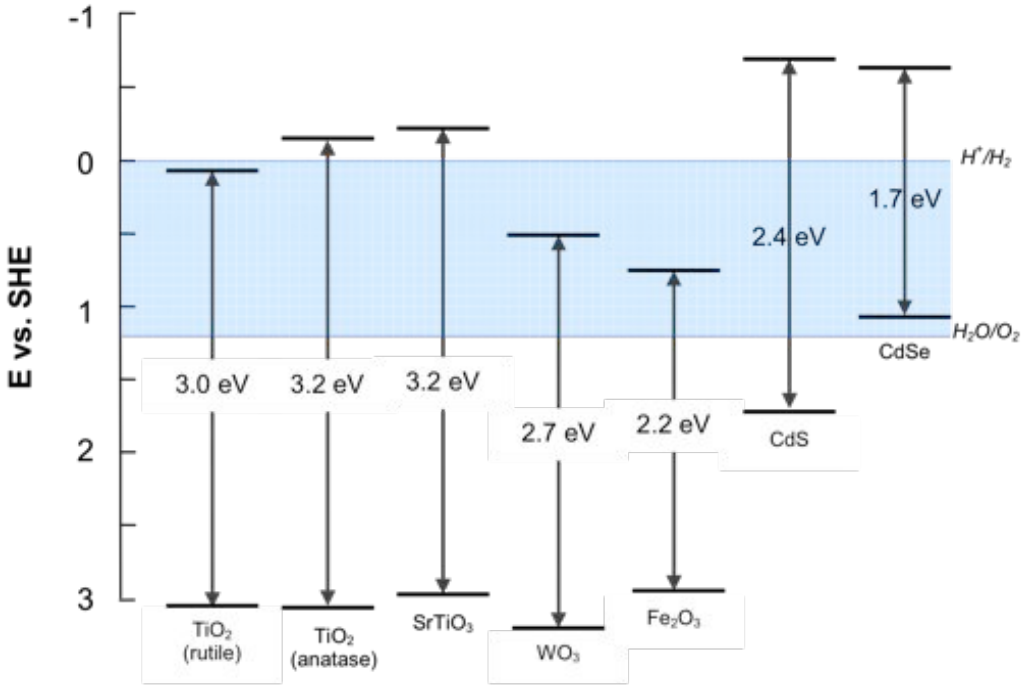

Figure 4 – Band gap values of various semiconductors. The band gap of anatase TiO_2 is approximately 0.2 eV larger than that of rutile.

As can be seen in Fig.4, both anatase and rutile TiO_2 allotropic forms possess a band gap of approximately 3 eV. This means that the fundamental optical excitation requires wavelengths shorter than ~400 nm, i.e. UV radiation. Hence, any possible photo-activated process involving the use of TiO_2 would be able to gather only photons in the UV part of the solar spectrum (Fig.5), essentially wasting the entire visible portion of the solar spectrum. Unfortunately, the UV portion is an extremely small fraction of the total radiation arriving on the Earth's crust (see red spectrum in Fig.5). Therefore, extending (even slightly) the absorption capabilities of TiO_2 into the visible region would dramatically increase the efficiency of any possible photo-active device.

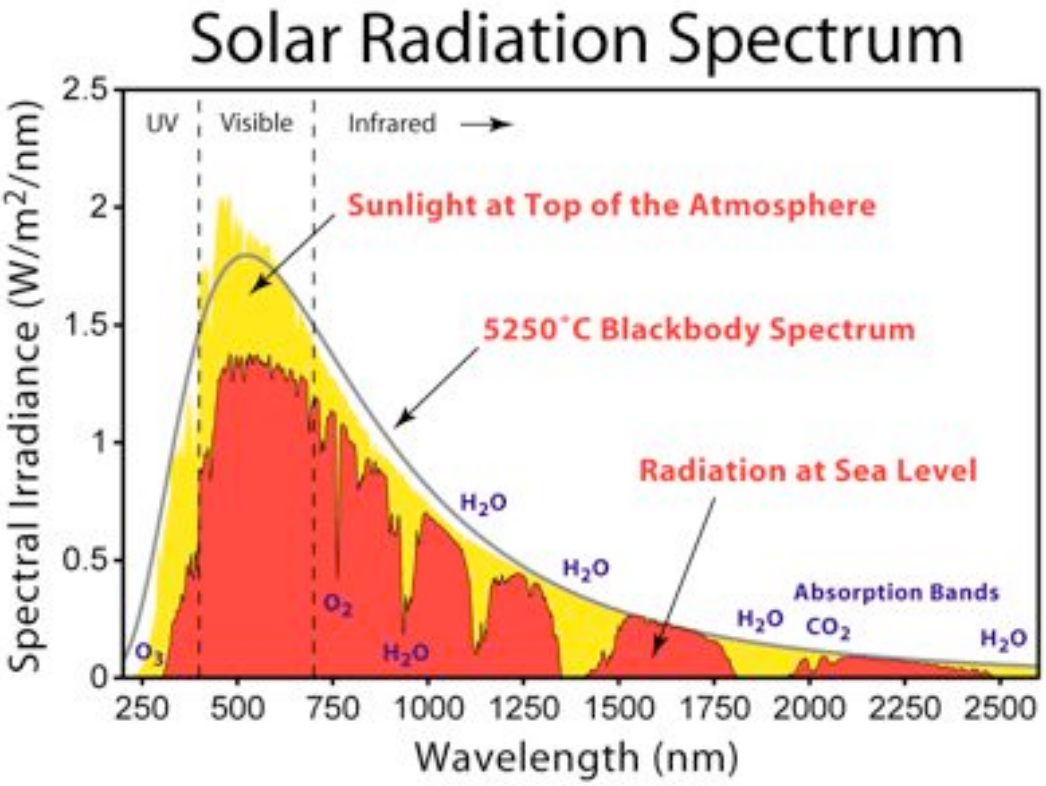

Figure 5 – Solar spectrum as measured outside Earth's atmosphere (yellow area) and on the Earth's crust (red spectrum) along with a calculated emission spectrum of a black body at 5250°C.

1.3 Photo-activated processes in TiO_2

1.3.1 General remarks

As we already mentioned before, all photoinduced phenomena are activated by an input of super-band gap energy to the semiconductor TiO_2. Absorption of a photon with enough energy leads to a charge separation due to an electron promotion to the conduction band and a generation of a hole (h^+) in the valence band. If the electrons are used in an outer circuit to perform work, we speak about a photovoltaic solar cell. On the other hand, photocatalysis is a well-known process and is mostly employed to degrade or transform (into less harmful substances) organic and inorganic compounds and even microorganisms. The recently discovered wettability, termed by Fujishima [Fujishima2000] as '*superhydrophilicity*', presents a large range of applications in cleaning and anti-fogging surfaces. The detailed material properties required for enhanced efficiency are different from each other. For enhanced photocatalysis, deep electron traps and high surface acidity are needed to lengthen the lifetime of photoexcited electrons and holes and to ensure better adsorption of organic substances on the surface. Meanwhile, low surface acidity and, most of all, a large quantity of Ti^{3+} is essential for hydrophilic surface conversion. These differences are related to the fact that photocatalysis is more likely to be sensitive to bulk properties, while hydrophilicity can be defined as an interfacial phenomenon. In the following sections, we will give an introductory paramount of the above-mentioned photoinduced processes.

1.3.2 Photovoltaic cells

Photovoltaic (PV) cells can produce electricity from the sunlight. They can be composed of various compounds, but all cells are based on semiconductors. Electrons can be promoted from the (occupied) VB to the (empty) CB when photons with energies

higher than the band gap are absorbed. These excited electrons can be extracted to an outer circuit where they can perform work. Without a driving force, the lifetime of the excited electron–hole pairs is too short to be used effectively, moreover, the spectral mismatch between the solar radiation and the semiconductor's absorption capability can be an important factor limiting the cell's performance. To solve both these problems, dopants are often introduced in the semiconductor.

Small levels of foreign elements are added to the semiconductor, which increase the conductivity as either the conduction band is partly filled with electrons (n-type doping) or the valence band is partly emptied (which equals partly filled with holes: p-type doping).

At present, most commercial solar cells consist of silicon. Although they exhibit quite a high efficiency, they have a number of serious drawbacks. Because of the low doping concentrations (ppm level) needed for efficient p–n junctions, extremely high-purity silicon is required. Furthermore, encapsulation to prevent oxidation in air is necessary. These factors lead to the price of solar electricity being about five times that of electricity based on fossil fuels. Other types of high-purity semiconductor solar cells with even higher efficiencies, like GaAs, are more expensive and sometimes contain hazardous and/or rare elements. These types of cells are mostly used in space applications. The highest theoretical efficiency for single crystalline silicon solar cells is 31%, due to unavoidable spectral mismatch, resistances and recombination losses. Stacks of different solar cell materials (i.e., tandem or multi-junction cells) could increase this efficiency to higher values. Research on Si-based solar cells is directed towards higher efficiencies, upscaling of production, and development of amorphous and thin-film devices.

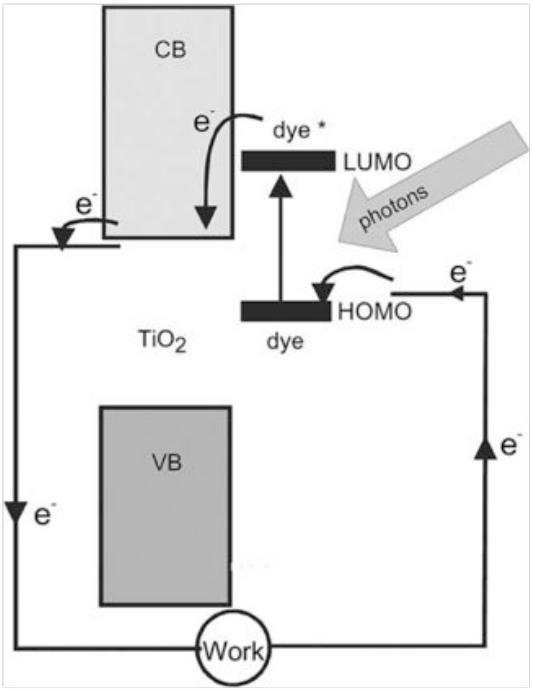

Figure 6 - Working principle of a hybrid solar cell. Photons are absorbed by the dye and an electron is excited to the LUMO level. This electron can be injected into the CB of the TiO2. The electron can be collected and perform work in the external circuit. It is transported back to regenerate the dye and to close the circuit

A different approach to realize cheap solar cells is the use of organic chromophores. In these so-called organic or hybrid solar cells, a wide band gap semiconductor, mostly an oxide like titanium dioxide or zinc oxide, is combined with a light-absorbing dye, which injects electrons into the conduction band of the metal oxide upon excitation with visible light (Fig.6). To close the current circuit and to regenerate the oxidized dye molecule, an electron has to be provided to the system. The principle of combining a visible light-absorbing species with a wide band gap semiconductor is called "sensitization". Most organic dyes can be treated both as semiconductors with narrow bands and as molecular compounds. If regarded as molecular compounds, excitation takes place between the highest occupied molecular orbital (HOMO) and the lowest unoccupied molecular orbital (LUMO).

Flat film solar cells made of wide band gap (oxide) semiconductors in combination with

organic compounds have a low efficiency (mostly less than 1%) [Serrano2009]. This is caused by the fact that organic materials tend to have a high resistivity, which leads to ohmic losses. The organic films must be thick enough to absorb enough light, but only a very narrow region near the interface between organic dye and inorganic semiconductor is found to be active, as excitons can only move a limited distance before they recombine. If the internal electrical field does not separate them fast enough, they will be lost. The exciton diffusion length is in the order of 5–20 nm for most organic compounds [VanderZenden2004].

A different approach is to apply a different morphology. In 1991, O'Regan and Gratzel reported the first organic solar cell with high efficiency (8%) [Oregan1991]. In this so-called Gratzel-type or dye-sensitized cell, anatase TiO_2 is used in nanocrystalline form, to which organic dye molecules are covalently attached with monolayer coverage. The use of nanostructured TiO_2 overcomes the problem of high resistance, since only a monolayer of dye is used (Fig.7). At the same time, the increased surface area ensures enough dye-absorption to absorb all the light and provides short-range contact between dye and oxide. A drawback of this device is, however, the need of a liquid electrolyte for regeneration of the oxidized dye molecules after electron injection. This leads to the risk of leakage or even explosion, which is not desirable in commercial devices. The electrolyte also suffers from degradation problems. Nowadays, a laboratory efficiency of 12% is reached [Serrano2009], but commercial application of these kinds of cells is still in the initial stage.

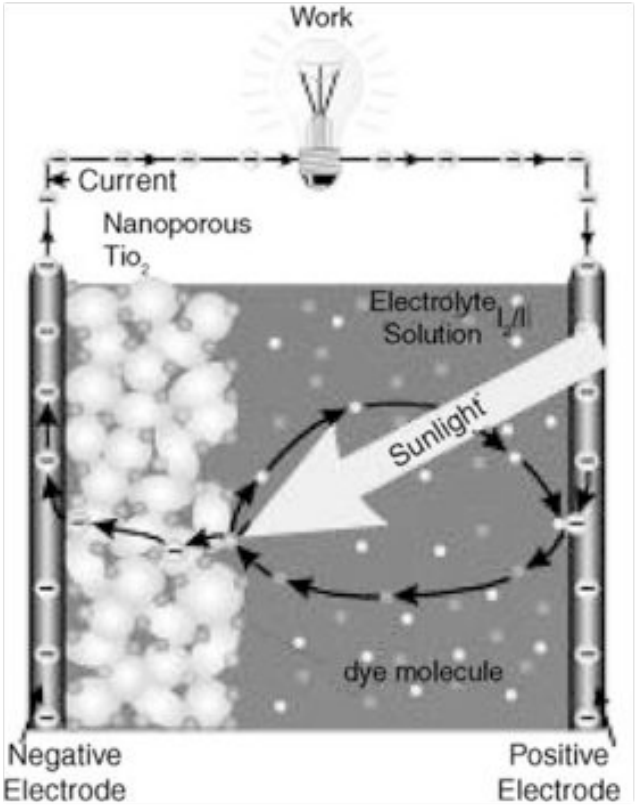

Figure 7 – Scheme of a dye-sensitized solar cell. The working principle is similar to an hybrid solar cell (Fig.6). See text for details

Much effort is being directed towards the development of similar nanostructured heterojunctions that can function without a liquid electrolyte. An ion-conducting polymer or a transparent hole-conducting material can replace the liquid. Another possibility is to use dyes that combine both functions and not only absorb light and inject electrons, but can also transport holes [Breeze2001]. Although organic substances exhibit, in general, much lower hole mobilities than inorganic compounds, semiconducting polymers have been shown to approach these high values and are suitable for utilization in these cells [Handbook].

Some excellent review articles about TiO_2-based photovoltaic cells have appeared in recent years [Nelson2002, Carp2004].

1.3.2 Photocatalysis

Overall, photocatalyzed reactions may be summarized as follows:

$$(\mathrm{Ox}_1)_{\mathrm{ads}} + (\mathrm{Red}_2)_{\mathrm{ads}} \xrightarrow[h\nu > E_g]{\text{semiconductor}} \mathrm{Red}_1 + \mathrm{Ox}_2$$

Depending on whether the sign of Gibbs free energy variation (ΔG_0) is negative or positive, the semiconductor-sensitized reaction may be an example of photocatalysis or photosynthesis, respectively.

For a semiconductor photocatalyst to be efficient, the different interfacial electron processes involving e^- and h^+ must compete effectively with the major deactivation processes involving e^- - h^+ recombination, which may occur in the bulk or at the surface.

Ideally, a semiconductor photocatalyst should be chemically and biologically inert, photocatalytically stable, easy to produce and to use, efficiently activated by sunlight, able to efficiently catalyze reactions, cheap, and without risks for the environment or humans. Titanium dioxide (with sizes ranging from clusters to colloids to powders and large single crystals) is close to being an ideal photocatalyst, displaying almost all the above properties. The single exception is that it does not absorb visible light.

Both crystal structures, anatase and rutile, are commonly used as photocatalyst, with anatase showing a greater photocatalytic activity [Diebold2003] for most reactions. It has been suggested that this increased photoreactivity is due to anatase's slightly higher Fermi level, lower capacity to adsorb oxygen and higher degree of hydroxylation (i.e., number of hydroxy groups on the surface) [Gerischer1992]. Reactions in which both crystalline phases have the same photo-reactivity or rutile a higher one [Mills2003] are also reported.

The disagreement of the results may lie in the intervening effect of various coexisting factors, such as specific surface area, pore size distribution, crystal size, and preparation methods, or in the way the activity is expressed. The behavior of Degussa P25 commercial TiO_2 photocatalyst, consisting of an amorphous state together with a

mixture of anatase and rutile in an approximate proportion of 80/20, is for many reactions more active than both the pure crystalline phases [Ohno2001]. The enhanced activity arises from the increased efficiency of the electron–hole separation due to the multiphase nature of the particles [Gerischer1992].

Efforts have been made to improve the photocatalytic activity of TiO_2. In this respect, the research can be divided into two categories: (a) to increase the photoactivity of TiO_2 in the near UV portion; (b) to shift the absorption band gap edge to the red in order to enhance activity in the visible portion of the spectrum. The latter is the path we will follow in our work.

1.4 Improving photo-activated reactions

1.4.1 Doping TiO_2

Doping the semiconductor with various transition metal ions may lead to an enhanced efficiency of the photocatalytic systems [Diebold2003, Carp2004]. Nonetheless, the underlying physical mechanisms of the enhanced photoactivity in doped semiconductors are not always fully understood.

TiO_2 particles can be substitutionally or interstially doped with different cations, forming mixed oxides or a mixture of oxides. The dominant parameters include the character and concentration of dopants and the applied thermal treatment [Palmisano1994].

The effect of metal ion dopants on the photocatalytic activity is a complex issue. The total induced alteration of the photocatalytic activity is made up from a sum of changes which occur in:

- the light-absorption capability of the TiO_2 photocatalyst;
- adsorption capacity of the substrate molecules at the catalyst's surface;
- interfacial charge transfer rate.

Many controversial results are reported in literature since even the method of doping leads to different morphological and crystalline properties of the photocatalyst. Impregnation, co-precipitation, co-deposition or sol–gel methods are usually used to introduce dopants [Carp2004]. The dopants content therefore directly influences the rate of e^-/h^+ recombination, which is reflected in:

$$W = (2\varepsilon\varepsilon_0 V_s / eN_d)$$

where W is the thickness of the space-charge layer, ε is the static dielectric constant of the semiconductor, ε_0 is the static dielectric constant in vacuum, V_s is the surface potential, N_d is the number of dopant donor atoms, and *e* is the electron charge. When W approximates the penetration depth of the light into the solid (l=1/a, where a is the light absorption coefficient at a given wavelength), all the absorbed photons generate e^-/h^+ pairs that are efficiently separated. As the concentration of the dopants increases, the space-charge region becomes narrower; the electron–hole pairs within the region are efficiently separated by the large electric field before recombination. On the other hand, when the concentration of doping is high, the space-charge region becomes very narrow and the penetration depth of light into TiO_2 greatly exceeds the space-charge layer. The recombination of photogenerated electron–hole pairs in the semiconductor therefore increases, because there is no driving force to separate them. Consequently, there is an optimum concentration of dopant ions to make the thickness of space charge layer substantially equal to the light penetration depth. For small colloidal particles, however, there is nearly no band-bending and the electrical field is usually small; so high dopant levels are needed to produce significant potential difference (permanent electric field) between the surface and the center of particles to separate photoinduced electron–hole pair efficiently [Hagfeldt1995].

Due to the fact that doping ions act as trapping sites, they can influence the lifetime of charge carriers. Usually, they enhance the recombination of photogenerated electrons and holes, and therefore do not allow reactions to proceed with any noticeable effect either under ultraviolet or visible light [Yuan2002]. P-type doping is obtained by

dissolving heterocations of valencies lower than that of Ti^{4+} (Al^{3+}, Cr^{3+}, Ga^{3+}, Ln^{3+}) in the TiO_2 lattice, while n-type doping is obtained by heterocations of valencies higher than +4 (Nb^{5+}, Ta^{5+}, Sb^{5+}). The inhibition effect is ascribed to an increase in the electron–hole recombination rate. More precisely, p-type dopants act as acceptor centers, which trap photoelectrons and, once negatively charged, attract holes, thus forming recombination centers [Hermann1984]. On the opposite, n-type dopants act as donor centers. By increasing the concentration of conduction electrons, they also favor the electron–hole recombination, which is detrimental for the photoefficiency.

Fe^{3+}, Ru^{3+}, Os^{3+}, and Gd^{3+} represent a special position between the metallic dopants. These four metal ions have a half-filled electronic configuration (d^5 and f^7) that is known to be more stable. When these metallic ions trap electrons, the half-filled electronic configuration is destroyed and their stability decreases. The trapped electrons can easily be transferred to oxygen adsorbed on the surface of the catalyst and the metallic ions return to the original stable half-filled electron structure. This might promote charge transfer and efficient separation of the electrons and holes by shallow trapped electrons. The prerequisite for an effective dopant involves the possibility of charge detrapping and migration to the surface.

Codoping may represent a viable way to improve the charge separation. Mono-crystalline TiO_2 codoped with Eu^{3+} and Fe^{3+} in an optimal concentration (1 at% Fe^{3+} and 0.5 at% Eu^{3+}) shows a co-operative effect, which significantly increases the photocatalytic degradation of chloroform in solution (five times compared to pure nanocrystalline TiO_2 and about two to six times compared to Fe^{3+} or Er^{3+} doped separately, respectively). Fe^{3+} serves as a hole trap and Eu^{3+} as an electron trap, speeding up the anodic and the cathodic processes.

The main objective of doping is to induce a decrease of the band gap or introduction of intra-band gap states, which results in more visible light absorption. Several papers deal with this subject, and titania is doped with different metal ions like: alkaline earth (Ca^{2+}, Sr^{2+} and Ba^{2+}), transition metal ions (Fe^{3+}, Cr^{3+}, Co^{3+}, Mo^{5+}) and rare earth ions (La^{3+}, Ce^{3+}, Er^{3+}, Pr^{3+}, Gd^{3+}, Nd^{3+}, Sm^{3+}) using different preparation techniques [Diebold2003,

Carp2004]. Substitution of Ti^{4+} by d^n metallic ions in the TiO_2 lattice creates allowed energy states in the band gap of TiO_2, which may induce photoactive transitions in the visible light, due to an excitation of an electron from this energy level into the TiO_2 conduction band.

The shift of the absorption edge in metal-ion doped systems may have a complex origin. It may be due to homogeneous substitution of Ti^{4+} or to segregated M_xO_y clusters [Xu2002]. Generally, if the absorbance shifts depend on the concentration of the dopant, it may be attributed to metal ion incorporation (until a critical limit that depends on the solubility of the dopant in TiO_2 is reached). If the shift depends on the annealing temperature, it may be attributed to the formation of metal clusters. While the origin of the shift may not be of crucial importance with respect to the optical applications of these systems (e.g., optical filters), it can be crucial for their photocatalytic activity. In fact, many reports about metal doping of TiO_2 (bulk and thin films) do not take these two different causes for the shift of the absorption edge into account.

Since surface sites can also be occupied by metal ion dopants, the surface properties as well as the point zero charge (PZC)* value may be altered by doping. These changes depend both on the type and amount of the dopant. Consequently, a modification of adsorption properties takes place. Lanthanide ions are known for their ability to form complexes with various Lewis bases (e.g., acids, amines, aldehydes, alcohols, thiols, etc.) through interaction of these functional groups with the f-orbitals of the lanthanides [Diebold2003, Carp2004]. Rare earth-doped TiO_2 photocatalysts present an improved NO_2 adsorption, and an enhancement of saturated adsorption capacity and adsorption equilibrium constants (compared to bare TiO_2) for several organic molecules is reported [Carp2004]. At the same time, doping with lanthanide ions could improve the photo-electrochemical properties and increase the photocurrent response and the incident

* In physical chemistry, the Point of Zero Charge (PZC) for a given material immersed into an electrolyte solution, is the pH at which the surface has a net neutral charge.

monochromatic photon current conversion efficiency in the range 300–400 nm [Wang1999].

A more efficient use of solar light (up to 20–30%) is realized with metal-implanted TiO_2 systems (Fe-doped titania, for example), in which the electronic state of the TiO_2 catalysts is modified due to the strong and long distance interactions (but without changes in the chemical properties of the surfaces) [Diebold2003]. Such photocatalysts initiate photocatalytic reactions effectively not only with UV but also with visible light irradiation (>400 nm). The extent of the red shift depends on the amount and type of metal ions implanted, following the general sequence: V > Cr > Mn > Fe > Ni [Carp2004]. As a result, under outdoor solar irradiation at ordinary temperatures, a photocatalytic activity several times higher than the original TiO_2 catalyst is registered for V or Cr ion-implanted TiO_2 [Zhang2004].

Another approach to induce visible light activated TiO_2 photocatalysis is by substituting oxygen with anions (N^{3+}, C^{4+}, S^{4+}, F, ..) which leads to a band gap narrowing. Films and powders of $TiO_{2-x}N_x$ have an improvement over bare TiO_2 under visible light (wavelength <500 nm) [Asahi2001]. Therefore, many techniques have been used to produce visible light active $TiO_{2-x}N_x$ photocatalyst such as precipitation, sol gel, dip-coating, ion implantation, etc [Carp2004]. Fluorine doping causes red shifts in the absorption edge and bromide-chlorine codoped nano-TiO_2 cause a shift of the adsorption edge from 410 to 425 nm [Luo2004]. Codoping of N and F in TiO_2 to $TiO_xN_yF_z$ leads to a band gap absorption edge of 570 nm and is shown to be effective for water oxidation. Chemically modified carbon-substituted TiO_2 absorbs light at wavelengths below 600 nm [Khan2002]. Therefore, this photocatalyst ensures high photocurrent densities and photoconversion efficiencies with several different dopants [Carp2004]. Hence, an accurate doping appears to be a promising route to obtain a higher efficiency in both photovoltaic and photocatalytic processes.

1.4.2 Final remarks and thesis outline

As we outlined above, TiO_2 is an extremely promising material due to its versatility, low cost and environmental compatibility. It possesses the capabilities to radically change the energy-production world; nonetheless several issues still limit its actual use in commercial devices. First of all its large band-gap hampers the possibility to harvest the visible part of the solar spectrum.

In this thesis we face this problem proposing two different approaches. The first involves the use of *cluster-assembled* TiO_2, whose deposition and characterization will be discussed in Chap. 3. We will then describe how such nanostructured films could be doped with nitrogen impurities (Chap.3) or even codoped, injecting both nitrogen and chromium atoms at the same time during the film synthesis (Chap.4). We will thoroughly analyze the variations emerging upon doping by using x-ray and optical spectroscopies. We will then carry out a similar characterization for a high-quality, epitaxial Cr-N codoped TiO_2 system (Chap.5). Finally, we will compare the results obtained on the cluster-assembled films and the epitaxial ones, in order to enlighten the possible drawbacks or advantages related with the two different nanometric structures.

References

[Slaoui2007] Slaoui A. and Collins R.T., *MRS Bulletin* **32**, 211 (2007).

[US-DOE2005] US - D. O. E. Office of Science, (2005).

[Dresselhaus2001] Dresselhaus M.S. and Thomas I.L., *Nature* **414**, 332 (2001).

[Crabtree2007] Crabtree G.W. and Lewis N.S., *Phys. Today* **60**, 37 (2007).

[Nozik1996] Nozik A.J. and Memming R., *J. Phys. Chem.* **100**, 13061 (1996).

[Linsebigler1995] Linsebigler A.L., Lu G., John J. and Yates T., *Chem. Rev.* **95**, 735 (1995).

[IEA-OECD2007] IEA, OECD. Renewables in global energy supply: an IEA facts sheet; 2007.

[Diebold2003] Diebold. U., *Surf. Sci. Rep.* **48**, 53 (2003).

[USGeologicalS] US Geological Survey Minerals Yearbook, 2002

[Natara1998] Natara N.C., Funaga N. and No M.G. *Thin Solid Films* **322**, 6 (1998).

[Philips1997] Philips L.G., Barbano D.M. *J. Diary Sci*. **80,** 2726 (1997).

[Schultz2002] Schulz J. et al., *Adv. Drug Deliv. Rev.* **54,** 157 (2002).

[Cord1971] Cord A.T. and Saunder H.F., *US Patent No.* ***273019***, (1971).

[Parker1990] Parker F.J., *J. Am. Ceram. Soc.* **73,** 929 (1990).

[Thompson1995] Thompson R. *Industrial inorganic chemicals; production and uses.* The Royal Society of Chemistry, (1995).

[Griebler1998] Griebler W.D., Hocken J. and Schulte K. *ECJ* **1–2,** H (1998).

[Macleod1986] Macleod H.A. *Thin film optical filters. 2nd ed.*, New York: MacMillan, 370 (1986).

[Kumazawa1999] Kumazawa N. et al., *J. Electrochem. Chem.* **472**, 137 (1999).

[Logothetis1980] Logothetis E.M. *Ceram. Proc. Eng. Sci.* **1**, 281 (1980).

[Savage2001] Savage N et al., *Sens. Act. B* **79**, 17 (2001).

[Poluncheck2000] Poluncheck L. et al., *Biomaterials* **21**, 539 (2000).

[Vedrine2000] Vedrine J.C., Bond G.C. and Forzatti P., *Catal. Today* **56**, 339 (2000).

[Weber1999] Weber R., Sakurai T. and Hagenmaier H., *Appl. Catal. B* **20**, 249 (1999).

[Boccuzzi2002] Boccuzzi F. et al., *Catal. Today* **75**, 169 (2002).

[Fan2003] Fan L. et al., *Appl. Catal. A* **246**, 87 (2003).

[Despres2003] Despres J. et al., *Appl. Catal. B* **43**, 389 (2003).

[Li2000] Li C. et al., *Nucl. Instrum. Meth. Phys. Res. B* **169**, 21 (2000).

[Chambers2001] Chambers S.A. et al., *Appl. Phys. Lett.* **79**, 3467 (2001).

[Kavan1999] Kavan L., FAttakhova D. and Krtil P., *J. Electrochem. Soc.* **146**, 1375 (1999).

[Dubrovinsky2001] Dubrovinsky L.S. et al., *Nature* **410** 653 (2001).

[Carp2004] Carp O. et al., *Prog. Sol. St. Chem.* **32**, 33 (2004).

[Norotsky1967] Norotsky A., Jamieson J.C. and Kleppa O.J. Science **158,** 338 (1967).

[So2001] So W.W., Park S.B., Kim K.J., Shin C.H. and Moon S.J., *J. Mater. Sci.* **36,** 4299 (2001).

[Zhang2000] Zhang H. and Banfield J.F., *J. Phys. Chem. B* **104**, 3481 (2000).

[Zhang1998] Zhang H. and Banfield J.F., *J Mater Chem* **8**, 2073 (1998).

[Fujishima2008] Fujishima A. et al., *Surf. Sci. Rep.* **63**, 515 (2008).

[Kumar1999] Kumar S.R. et al., *Mater. Lett.* **38**, 161 (1999).

[Kumar1993] Kumar K.N.P., Keizer K. and Burrgraaf A.J., *J. Mater. Chem.* **3**, 1141 (1993).

[Chao2003] Chao H.E., Yun Y.U., Xingfang H.U. and Larbot A., *J. Eur. Ceram. Soc.* **23**, 1457 (2003).

[SaLi2009] Sa Li and Jena P., *Phys. Rev. B* **79**, 201204 (2009).

[Karvinen2003] Karvinen S., *Solid. State. Sci.* **5**, 811 (2003).

[Wang1999] Wang C.C. and Ying J.Y., *Chem. Mater.* **11**, 3113 (1999).

[Izutsu1997] Izutsu H., Nair P.N. and Mizukami F., *J. Mater. Chem*. **7**, 855 (1997).

[Zhang2002] Zhang Y.H. and Reller A., *Mater. Sci. Eng. C* **19**, 323 (2002).

[Gouma1999] Gouma P.I., Dutta P.K. and Mills M.J., *Nanostruct. Mater.* **11**, 1231 (1999).

[Eyring1970] Eyring, H., *Physical Chemistry*, Academic Press Inc. U.S. (1970).

[Gratzel1989] Grätzel M., *Heterogeneous Photochemical Electron Transfer*, CRC Press (1989).

[Morrison1980] Morrison S.R., *Electrochemistry at semiconductor and oxidized metal electrodes*, Springer (1980).

[Lindgren2004] Lindgren T., *In Search of the Holy Grail of Photoelectrochemistry – A Study of Thin Film Electrodes for Solar Hydrogen Generation*, Acta Universitatis Upsaliensis, Sweden (2004).

[Fujishima2000] Fujishima A., Rao T.N. and Tryk D.A., *J. Photochem. Photobiol. C: Photochem. Rev.* **1**, 1 (2000)**.**

[Serrano2009] Serrano E., Rus G. and Garcia-Martinez J., *Renewable and Sustain. En. Reviews* **13**, 2373 (2009).

[VanderZenden] Van der Zanden B., Van de Krol R., Schoonman J. and Goossens A., *Appl. Phys. Lett.* **84**, 2539 (2004).

[Oregan1991] O'Regan B. and Gratzel M., *Nature* **353**, 737 (1991).

[Breeze2001] Breeze A.J., Schlesinger Z. and Carter S.A., *Phys. Rev. B* **64**, 12525 (2001).

[Handbook] *Handbook of oligo- and polythiophenes. Weinheim,* Wiley-VCH (1999).

[Nelson2002] Nelson J., *Curr. Opin. Solid Sate Mater. Sci.* **6**, 87 (2002).

[Gerischer1992] Gerischer H. and Heller A., *J. Electrochem. Soc.* **139**, 113 (1992).

[Mills2003] Mills A., Lee S.K. and Lepre A., *J. Photochem. Photobiol. A: Chem.* **155**, 199 (2003).

[Ohno2001] Ohno T. et al., *J. Catal.* **203**, 82 (2001).

[Palmisano1994] Palmisano et al., *Catal. Lett.* **24**, 303 (1994).

[Hagfeldt1995] Hagfeldt A. and Gratzel M, *Chem Rev* **95**, 49 (1995).

[Yuan2002] Yuan Z.H., Jia J.H. and Zhang L., *Chem Phys.* **73**, 323 (2002).

[Hermann1984] Hermann J.M. et al., *Chem. Phys. Lett.* **108**, 618 (1984).

[Xu2002] Xu A.W. et al., *J. Catal.* **207**, 151 (2002).

[Wang1999] Wang Y.Q. et al., *Thin solid Films* **349**, 120 (1999).

[Zhang2004] Zhang J.L. et al, *Chin. J. Catal.* **25**, 10 (2004).

[Asahi2001] Asahi et al., Science **293**, 269 (2001)

[Luo2004] Luo H. et al., *Chem. Mater.* **16**, 846 (2004).

[Khan2002] Khan S.U.M. et al., *Science* **297**, 223 (2002).

Introduction

In the following paragraphs we will briefly introduce the most important experimental techniques used in our measurements. This primarily includes X-ray Photoemission Spectroscopy (XPS), sometimes also called Photo-Emission Spectroscopy (PES), Resonant Photo-Emission Spectroscopy (RESPES) and Near-Edge X-ray Absorption Fine Structure (NEXAFS) spectroscopy.

2.1 Experimental techniques

2.1.1 X-ray Photoemission Spectroscopy (XPS-PES)

Photoelectron spectroscopy (PES), which is also often simply called "photoemission", is by now a standard and well-developed technique of special importance in the fields of surface science and condensed-matter physics [1-Fadley1978, 2-Hufner1995], and the fundamental excitation process is indicated in Fig.1.

In PES, a sample is exposed to a source of mono-energetic photons that excite electrons from the sample into free-electron states that can propagate into vacuum. These free electrons, which are termed *photoelectrons*, have different kinetic energies, depending upon their binding energy in the sample. Photoelectrons are produced by the photoelectric effect, which was explained theoretically by Einstein in 1905. The relationship between the photon energy *hv* and the kinetic energy E_{kin} of the photoelectron is given by Einstein's photoelectric equation $E_{kin} = h\nu - E_b^v(k)$, where $E_b^v(k)$ is the binding energy of an electron in the k^{th} level of the atom, as referenced to the vacuum level.

Since electron energy levels are quantized, the kinetic energy distribution of the

photoelectrons consists of a series of peaks, which in first approximation reflects the one-electron energy-level description for the core subshells of the various atoms in the sample, as diagrammatically shown in Fig. 1.

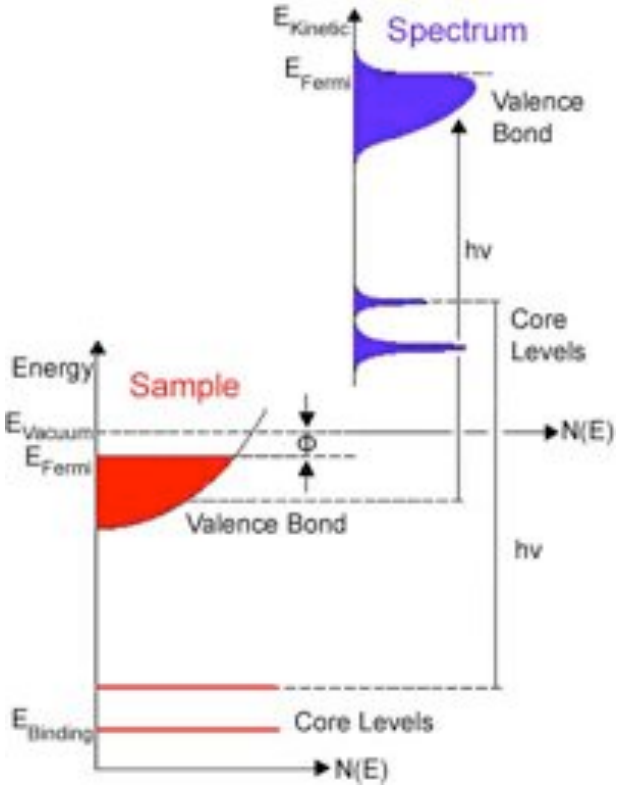

Figure 1 - Simple model of the photoemission process, illustrating the excitation of core and valence level electrons into the continuum by a sufficiently energetic photon. Note that the final excited state atom contains a hole, therefore the atom is finally singly ionized

This description is correct provided we neglect corrections for electron relaxation and other final-state effects associated with the hole that is left behind after photoelectron emission. In the more precise language of contemporary many-body theory, the excitations are really quasiparticle-like, with self-energy corrections being used to determine energy positions in spectra, and a spectral function being used to determine intensities.

From an experimental point of view, the kinetic energy distribution of the

photoelectrons is measured by an electron energy analyzer or spectrometer, as shown schematically in Fig.2, and one usually analyzes the so-called "no-loss" or "coherent" photoelectron peaks in the resulting spectrum that are made up of electrons that have not suffered significant inelastic scattering events.

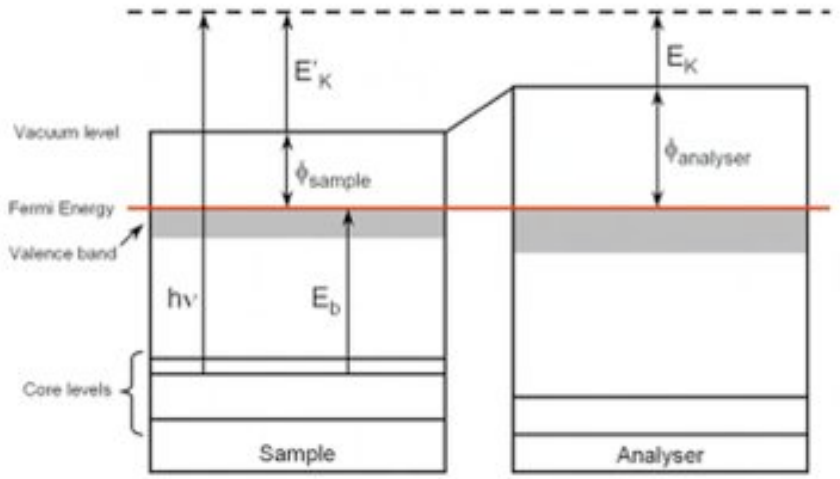

Figure 2 - Sketch of the sample-analyser system in a typical photoemission experiment

Since photoelectron spectra are analyzed primarily in terms of the unscattered or "no-loss" features, photoelectrons from far below the surface region of the sample are heavily attenuated through inelastic processes, and are either not emitted from the sample, or appear as a continuous inelastic background at kinetic energies less than predicted by the Einstein's equation. The inelastic attenuation length for a number of elements is shown in Fig.3.

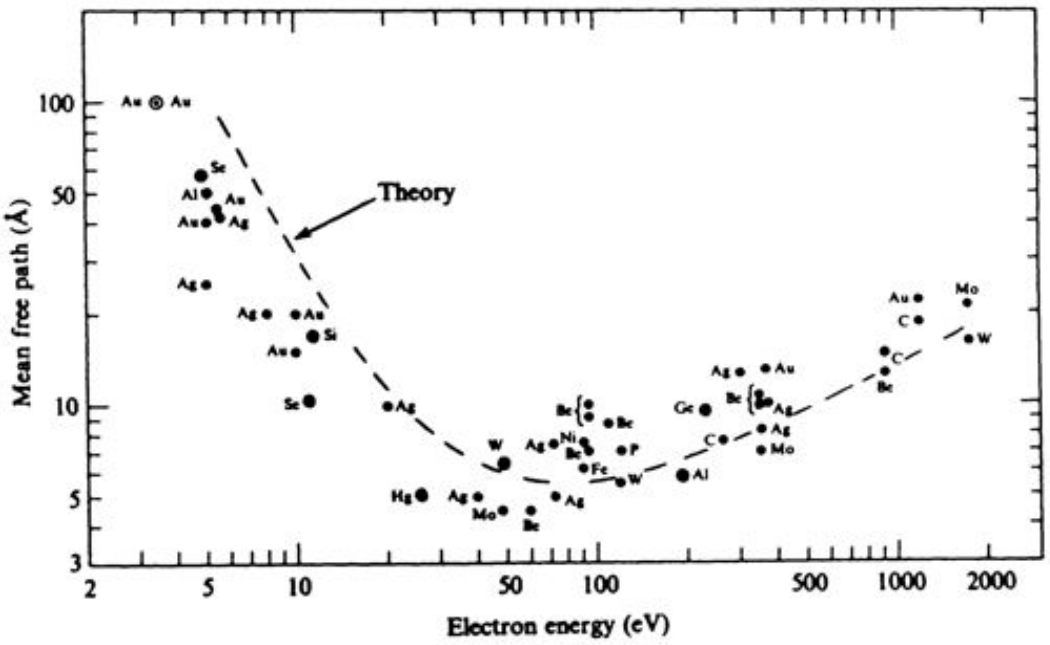

Figure 3 - The so-called "universal curve" for electron attenuation in solids as a function of the electron kinetic energy

Several fundamental aspects of the PES technique warrant mention here:

***Elemental sensitivity*.**

First, the photoemission process allows element specific information to be obtained for a given sample, due to the discrete set of strongly bound core-levels, which uniquely characterize each element in the periodic table (cf. Fig.1).

Chemical-state specificity

Variations of the chemical environment can cause shifts in the binding energies of the core-level electrons, an effect known as the *chemical shift*, thus extending the sensitivity and utility of PS as a powerful technique for surface analysis.

Quantitative information

The core-level photoelectron peak intensities can be directly related via well-known photoelectric cross sections to atomic concentration of the sample, thereby providing qualitative and quantitative information as to sample composition and dopants atomic concentration.

Surface sensitivity

The suitability of PES to surface studies of materials is essentially due to the short inelastic attenuation length of the photoelectrons in the sample, as shown in Fig. 2.3, where the so called "universal curve" for electron attenuation lengths in a large number of elemental samples as a function of electron kinetic energy is shown [3-Seah1979, 4-Powell1994].

Band structure and dispersions

Photoelectrons emitted from the weakly bound valence levels can also be studied, permitting the direct measurement of energy bands and other more complex properties related for example to magnetism and strongly correlated materials via the more correct quasiparticle picture [2-Hufner1995, 5-Schattke2003].

Auger spectroscopy and structures

A photoelectron spectrum may also contain photon-induced *Auger* electrons that result from secondary processes involving non-radiative decays of core holes. Auger electrons can be discerned from the "no-loss" photoelectrons by having constant kinetic energies regardless of photon energy, this aspect of PES will be exploited in Chap.3.

Many body effects

As noted already, photoelectron spectra can show signatures of many-body processes in solids. When the system is in an excited state, an amount of energy equal to the difference between the excited state and the ground state energies is subtracted from the energy of the outgoing photoelectron, which thus is detected at higher binding energy, giving rise to secondary peaks called satellites [1-Fadley1978, 2-Hufner1995].

Another aspect that we want to outline is the energy balance in a photoemission process. The kinetic energy of the photoelectron is determined by the photon energy and the initial and final state energies of the system. Note that if the (usually charge-neutral) *N*-electron system is initially in the ground state, after the photoemission process, it can be left in some excited state of the singly charged *N-1*-electron system produced. For an atom or a molecule, the energy conservation relationship can be very generally written as

$$h\nu + E_0^N = E_{kin}^{'} + E_n^{N-1} \tag{2.1}$$

with the energies being referenced to the vacuum level, and where

$h\nu$ = photon energy

E_0^N = ground state of the initial N-particle system

E_n^{N-1} = the final nth excited state of the *N-1*-particle system

$E_{kin}^{'}$ = kinetic energy of the photoelectron just as it leaves the spatial region affected by the potential of the sample

Since $E_{kin}^{'}$ is a positive quantity, for the photoemission process to be possible the photon energy hn must exceed a threshold energy which is given by

$$E_b^V = h\nu - E_{kin}^{'} = E_n^{N-1} - E_0^N \tag{2.2}$$

This quantity, $E_n^{N-1} - E_0^N$, is by definition the *binding energy* of the photoelectron and, in the case of atoms, the lowest binding energy coincides with the *first ionization*

potential. We also note here that it is common to assume that the excitation process is dipolar in character, so that the usual dipole selection rules apply, but we do not state these explicitly here.

While for the case of atoms or molecules the energies are referenced to the vacuum level, in the case of solids it is customary to refer energies to the *Fermi* level. If ϕ_s denotes the *work function* of the sample, that is, the energy required to bring an electron from the Fermi level to the vacuum level, then Eq. (2.2) can be written as

$$h\nu + E_0^N = E_{kin}^{'} + E_n^{N-1} + \phi_s \,. \tag{2.3}$$

Note that the work function ϕ_s on the right side of Eq. 2.3 is necessary since the kinetic energies are referenced to the vacuum levels. In this case, for the photoemission process to occur, the photon energy hn must exceed a threshold energy, which is now given by

$$h\nu - E_{kin}^{'} = E_n^{N-1} - E_0^N + \phi_s \,. \tag{2.4}$$

The binding energy $E_n^{N-1} - E_0^N$, now referred to the Fermi level, is lower than when referenced to the vacuum level by an amount equal to ϕ_s, and is given by

$$E_b^F = \left(E_n^{N-1} - E_0^N\right)_F = h\nu - E_{kin}^{'} - \phi_s \,, \tag{2.5}$$

where the subscript *F* stresses that the binding energy is referenced to the Fermi level.

We note that there is no contradiction between Eq. 2.2 and Eq. 2.5, as Eq. 2.5 becomes equal to Eq. 2.2 when one sets $\phi_s = 0.$

The sample and the spectrometer are grounded, so that their Fermi levels are set equal. Therefore, one can write

$$h\nu = E_b^V(k) + E_{kin}^{'} = E_b^F(k) + \phi_s + E_{kin}^{'}(k) = E_b^F(k) + \phi_{spect} + E_{kin}(k), \tag{2.6}$$

where $E_{kin}(k)$ is the measured kinetic energy of a photoelectron peak associated with a given level *k* as measured by the spectrometer and ϕ_{spect} is the work function of the

spectrometer, that is, the energy required to bring an electron from the Fermi level to the spectrometer. The spectrometer work function is constant, and can be easily determined by the measurement of the Fermi level of a metal reference sample. Once determined, this quantity can be allowed for in all the data.

The usefulness of PES as a technique to investigate many body interaction in solids and, more specifically, in strongly correlated materials is fully appreciated when one notices that the expression for the binding energy (either referred to the vacuum or the Fermi level) involves the difference between the energy E_n^{N-1} of the final excited state of the *(N-1)*-particle system (with one electron missing), and the energy E_0^N of the ground state of the initial *N*-particle system. Therefore, from a PES measurement one can get information about the excitation energies of the system left behind upon the photoemission process, thus revealing some of the many body excitations, which are characteristic of the response of a system to the incoming light perturbation [5-Schattke2003].

2.1.2 Resonant Photoelectron Spectroscopy (RESPES)

Resonant photoelectron spectroscopy (RESPES) [6-Allen1992] is a particular case of the photoemission process described above in case of incident photon energy close to an absorption ionization threshold. RESPES is a concrete prove of the quantum mechanical nature of the matter. The enhancement of the PE cross section of valence band states while the energy is tuned across an absorption edge is a manifestation, on a macroscopic scale, of the quantum mechanical interference effect between the direct and indirect photoemission processes from the valence band, the indirect one resulting from the core-hole recombination, as it is clarified in the following of this paragraph. RESPES has been widely exploited since many years as a powerful tool to investigate the character of VB states.

Fig.6 reports the sketch of the processes leading to RESPES. When the incident photon energy is tuned across an absorption threshold of a core level, the transferred energy is just enough to excite an electron from a core level to a bound state in the unoccupied valence band (Fig.6-a). This transition leaves the system in an excited state, which can de- excite via two possible channels.

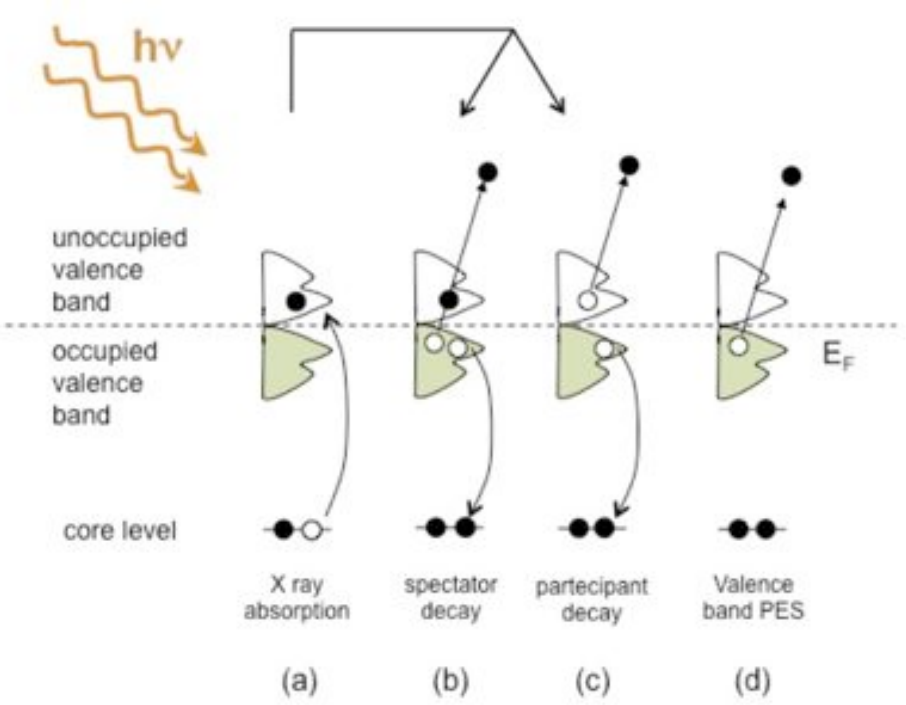

Figure 4 - Schematic energy level diagram of some of the possible electronic excitation and de-excitation processes involved in a RESPES experiment

One channel is shown in Fig.6-b: the excited electron remains in the normally unoccupied levels in the final states, and two valence electrons are removed from the atom via a normal Auger transition. This channel is often called resonant Auger or spectator channel, and leaves the system in a +1 charge state, but is a valence- excited state. The second possibility (the so-called participant channel) is that the excited electron is involved in the Auger process (Fig.6-c); this leaves the system with a single

valence vacancy and a charge of +1. This quantum channel has a final state which is energetically the equivalent of the direct photoemission from the valence band (Fig.6-d). The constructive interference between these two channels gives rise to a massive resonant enhancement of atomic specific valence band states as hv passes through the absorption edge. This fact gives rise to an anomalous increase of the PE cross section of element-specific VB states at constant binding energy. So the total intensity of the RESPES process in given in a representative way by

$$I_{TOT} \propto |PES + CorePES|^2 = |PES|^2 + |CorePES|^2 + Interference$$

where the interference term accounts for the coherence between the two processes of direct and indirect photoemission. It has also been demonstrated [7-Mishra1998] that the temporal matching of the processes as well as energy matching is a requirement for true "resonant photoemission", so that the two processes are coherent and the overall intensity is due to the squaring of the sum of the amplitudes, and not only the summing of the squares of the amplitudes (as it is the case for an incoherent process). Possibly, incoherence would give rise to the loss of photoemission characteristics in the process, with a domination of Auger-like properties, as it will be clarified in the following.

RESPES not only provides a way to access for the electronic properties, but also for the time scale of the charge transfer properties. In this sense, it can be regarded as a pump-and-probe technique, with an intrinsic time scale given by the lifetime of the intermediate (core-hole) state, the so-called core-hole clock. We will give a qualitative explanation of the method based on the charge transfer process, skipping the radiation-less Raman scattering theory which can be found elsewhere [8-Gelmukhanov1999, 9-Agren2000] in the Kramers-Heisenberg formulation.

In Fig.6-b and -c two possible decay channels of the de-excitation process after an x-ray absorption event are shown, when the excited electron remains localized on the excited atom. The resulting behavior, with the clear signature in the dispersion of the peak positions as the photon energy changes (constant binding energy), is termed as Raman-Auger emission or Raman scattering or Raman regime.

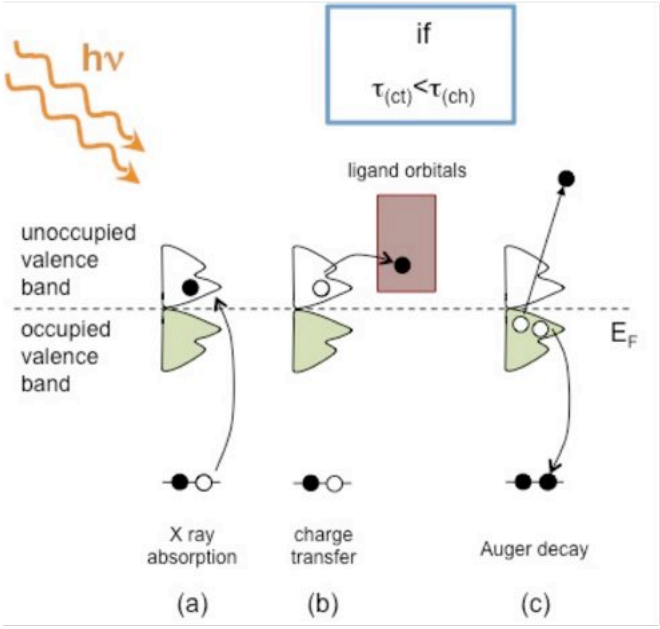

Figure 5 - Schematic view of the charge transfer de-excitation process. After excitation via XAS, the excited electron can hop into ligand (or substrate) orbitals (b) before participating in the core hole recombination process, leaving the atom free to emit via normal Auger modes(c). This delocalization of the excited electron must happen on a characteristic time is shorter than the lifetime of the corresponding core-hole.

If, however, the excited state of the probed atom can overlap with ligand orbitals, there is a finite probability that the excited electron can delocalize before participating in the core hole recombination (see Fig.7-b). At this stage, the system is free to de-excite via a normal Auger decay at constant kinetic energy, leaving the system in a 2+ final local configuration (Fig.7-c, normal Auger regime). This transition is viewed as a change from a one-step coherent to a two-step incoherent process, and would lead to a quenching of the resonant channels in the decay of the intermediate state. The transition between the two regimes is governed by the competition between the time scales corresponding to the core-hole decay (τ_{ch}) and the charge transfer (τ_{ct}) or, in more general terms, the delocalization of the excited core electron in the intermediate state. If $\tau_{ct} < \tau_{ch}$ the electron will hop on the ligand and the system will de-excite via

normal Auger behavior. These rates are not simply constants, but they change throughout the absorption threshold. As was suggested by earlier measurements (for example [10-Karis1996]), the charge transfer time may possibly depend on the intermediate state. This is due to the excitations into orbitals hybridized with the neighboring atoms, which have higher probability of delocalization in a given time. On the other hand, close to the threshold, the core-hole decay time has to be replaced by an "effective scattering time", which depends on the photon energy relative to the absorption edge [8-Gelmukhanov1999, 9-Agren2000].

Considering the excitation by an incoming photon of energy Eγ of an atom from its ground state $|0\rangle$ to all possible intermediate levels $|j\rangle$ of energies E_{j0} and the subsequent decay to a final state $|f\rangle$, the resonant scattering amplitude is given by

$$F_{resonant} = \sum_{j} \frac{\langle f|Q|j\rangle\langle j|Q|0\rangle}{E_\gamma - E_{j0} + i\Gamma}$$

where Q and D are the Coulomb and the dipole operators, respectively, and Γ is the life-time width of the core-hole excited intermediate state. Defining the detuning Ω as the energy difference $E_\gamma - E_{j0}$, one can obtain a scattering time (or effective duration of scattering) as [8-Gelmukhanov1999, 9-Agren2000]

$$\tau_{ct} = \frac{1}{\sqrt{\Omega^2 + \Gamma^2}}$$

where the contribution to scattering is mostly limited to times $t < \tau_{ct}$. For zero detuning, i.e. on the resonance, the effective scattering time is given by the core-hole lifetime Γ^{-1}, whereas the scattering gets faster for larger detuning. It follows immediately that the probability of observing coherent excitation and de-excitation increases with detuning, purely on a quantum mechanical basis as the system will not have sufficient time for relaxation for scattering faster than the charge transfer.

So, within the sudden approximation, RESPES can also probe the degree of localization of resonating states and indirectly the time scale of the charge transfer processes of matter in the femtosecond time regimes, with an intrinsic lifetime scale given by the

lifetime of the intermediate (core-hole) state [9-Agren2000, 11-Bruhwiler2002].

2.1.3 X-ray Absorption Spectroscopy (XAS) and Near-Edge X-ray Absorption Fine Structure (NEXAFS)

When x-rays pass through any material, a fraction of them is absorbed. In fact, a primary source of this absorption in the VUV/soft x-ray regime is just the photoelectric effect mentioned above, which produces a photoelectron in a free state above the vacuum level. Beyond this, absorption of a photon so as to excite an electron from a bound occupied state to a bound unoccupied state can also lead to strong absorption. Indeed, when the photon energy is just sufficient to excite these electrons above the Fermi level, then large increases in absorption occur, with these being known as *absorption edges* or *resonances* or *white lines* (a notational relic from the past practice of recording x-ray transmission with film, in which case an absorption peak showed up as a white line in a wavelength spectrum), and they are associated with different core levels in a given atom.

While other well-known absorption mechanisms exist beyond the photoelectric effect and near-edge absorption, including Compton scattering, pair-production, and nuclear excitation, they are entirely negligible for the photon energies considered in this work (< 2 keV).

X-ray absorption spectroscopy (XAS), in which the detailed form of the core-level absorption edges are recorded in a sample (e.g. by transmission through thin foils, reflection, or total/partial electron-yield measurements [12-degroot1994]), shares the element specificity seen in PES. Because of the relatively deep penetration depths of the photons, XAS is generally considered to be a bulk technique; however, if inelastically scattered secondary electrons are used to detect the absorption, XAS in fact may only reach in to an average depth of 20-30 Å.

Any absorption spectrum is typically divided into two distinct regions, as illustrated in Fig.4: one region is called *near edge*, while the second region from about 100 eV above a given absorption edge and up to as much as 1000 eV further is called *extended*. The study of the absorption spectrum in these two distinct regions gives rise to two spectroscopies, *near edge x-ray absorption spectroscopy* (NEXAFS) or *x-ray absorption near edge spectroscopy* (XANES), and *extended x-ray absorption fine structure* (EXAFS), which provide complementary information about the electronic structure and local atomic positional structure, respectively. We will now focus on the NEXAFS spectroscopy, which is the one used in our experiments.

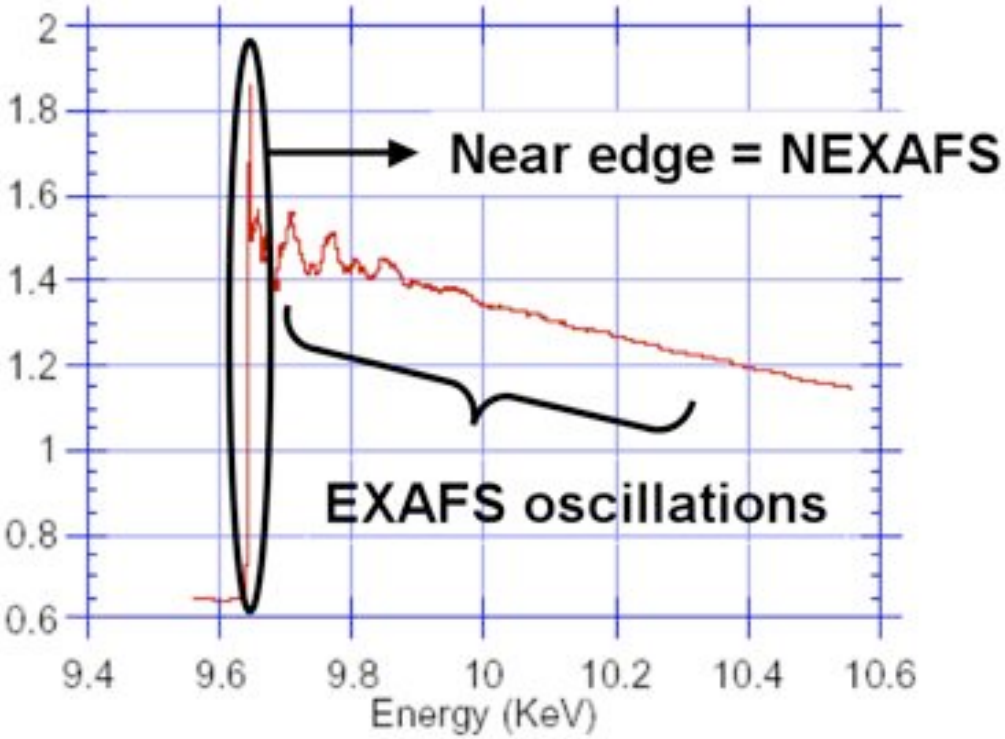

Figure 6 – A typical XAS spectrum showing the near edge region (NEXAFS) and the EXAFS oscillations

The Near Edge X-ray Absorption Fine Structure (NEXAFS) spectroscopy is a widely used

technique giving information about the local structure and the unoccupied electronic states. NEXAFS requires the use of a tunable x-ray source such as a synchrotron. The photon energy is scanned over an interval around the binding energy of a given core level in the sample under investigation. Above a characteristic photon energy (the absorption threshold of a given core level), the core electrons can absorb the incident light and make transitions to empty valence states between E_F and the vacuum level (as sketched in Fig.5). The spectra shown in this thesis have been acquired by measuring the current generated in the sample (total electron yield) while the photon energy was varied across the absorption threshold and above.

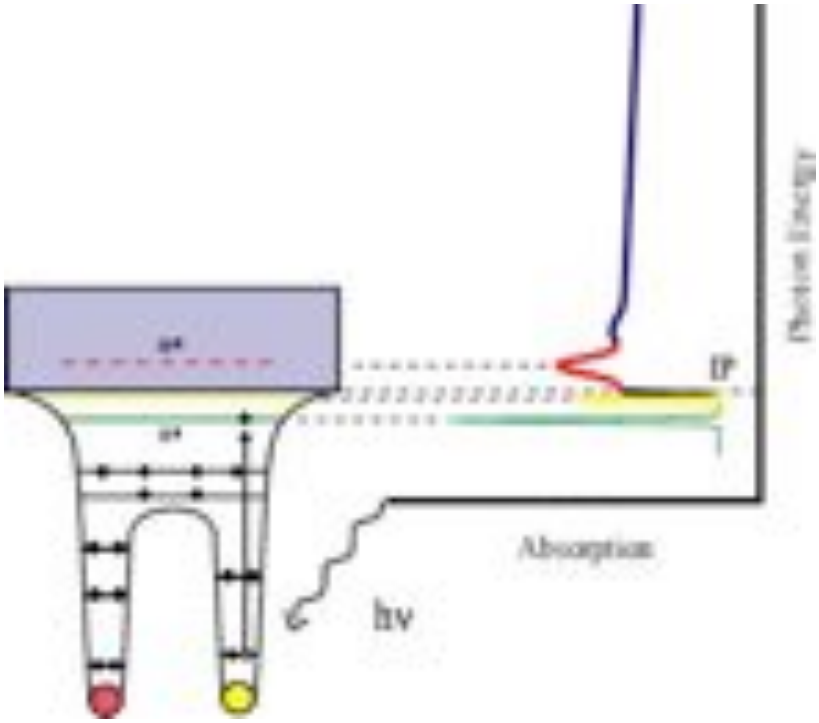

Figure 7 - Schematic energy level diagram of the indicated electronic excitation or de-excitation processes (see the text for the explanation).

The NEXAFS profile is expected to mimic the unoccupied density of states (DOS) $\rho_{empty}(E)$ (where E indicates the binding energy inside the sample) projected onto the excited atomic site via the dipole selection rules2, according to the x-ray absorption

probability $w_{fi}^{XAS}(\hbar\omega)$ given via the Fermi golden rule by

$$w_{fi}^{XAS}(\hbar\omega) \propto |M_{fi}|^2 \, \rho_{empty}(E) \, \delta(E_f - E_i - \hbar\omega)$$

where $\hbar\omega$ is the photon energy

M_{fi} is the matrix element associated to the absorption process

$\delta(E_f - E_i - \hbar\omega)$ accounts for the energy conservation between the initial and the final states.

Within the sudden approximation, the dipole matrix element term is defined as

$$M_{fi} \equiv \langle \phi_f | H_{int} | \phi_i \rangle$$

where ϕ_i and ϕ_f are the wavefunctions associated to the initial and the final states, and H_{int} is the perturbation Hamiltonian due to the interaction with the photon given by

$$H_{int} = \frac{e}{2mc}\left(\vec{A}\cdot\vec{p} + \vec{p}\cdot\vec{A}\right) = \frac{e}{mc}\,\vec{A}\cdot\vec{p},$$

with p the electronic momentum operator and A the electromagnetic vector potential. This can be also re-written as

$$|M_{fi}|^2 \propto |\langle \phi_f | \vec{\epsilon}\cdot\vec{p} | \phi_i \rangle|^2$$

where ε is the unit vector along the polarization direction of the vector potential A (that is parallel to the direction of the electric field E). Much more detailed and accurate descriptions of both the NEXAFS and the EXAFS techniques can be found elsewhere [13-degroot2008, 14-stohr1992].

References

[1-Fadley1978] Fadley C.S., in *Electron Spectroscopy, Theory, Techniques, and Applications*, C.R. Brundle and A.D. Baker (Eds.), Vol. II, Chapter 1, Pergamon Press (1978).

[2-Hufner1995] Hüfner S., *Photoelectron Spectroscopy : Principles and Applications*, Springer-Verlag (Berlin 1995).

[3-Seah1979] Seah M.P. and Dench W.A., *Surf. and Interface Anal.* **1**, 2 (1979).

[4-Powell1994] Powell C.J., Jabloski A., Tanuma S. and Penn D.R., *J. Electron Spectrosc. Relat. Phenom.* **68**, 605 (1994).

[5-Schattke2003] Schattke W. et al., in *"Solid-State Photoemission and Related Methods: Theory and Experiment"*, Chapter 1, Eds. W. Schattke and M.A. Van Hove, Wiley-VCH Verlag, Berlin (2003).

[6-Allen1992] Allen J. W., in *Synchrotron Radiation Research: Advances in Surface and Interface Science*, edited by R. Z. Bachrach (Plenum Press, New York, 1992), Vol. 1.

[7-Mishra1998] Mishra S.R. et al., *Phys. Rev. Lett.* **81**, 1306 (1998).

[8-Gelmukhanov1999] Gelmukhanovand F. and Agren H., Phys.Rep. **312**, 87 (1999).

[9-Agren2000] Agren H. and Gelmukhanov F., *J. El. Spectr. Rel. Ph.* **110**, 153 (2000).

[10-Karis1996] Karis O. et al., *Phys. Rev. Lett.* **76**, 1380 (1996).

[11-Bruhwiler2002] Bruhwiler P.A., Karis O. and Martensson N., *Rev. Mod. Phys.* **74**, 703 (2002).

[12-degroot1994] de Groot F.M.F., *J. Electron Spectrosc. Relat. Phenom.* **67**, 529 (1994).

[13-degroot2008] de Groot F.M.F. and Kotani A., in *Core level spectroscopy of solids*, CRC Press, (2008).

[14-stohr1992] Stohr J., in *NEXAFS Spectroscopy*, Springer-Verlag Berlin-Heidelberg (1992).

3.1 Introduction

Nanotechnology plays a fundamental role not only in science, research and development but also in everyday life, as more and more products based on nanostructured materials are introduced to the market.

The strong interest towards nanomaterials stem from their unique physical and chemical properties and functionalities that often differ significantly from their bulk counterparts. Many of these unique properties are extremely promising for emerging technological applications such as nanoelectronics, nanophotonics, biomedicine, information storage, communication, protective coatings, catalysis and energy conversion [HandbookNanoscience2007].

It is commonly agreed that nanotechnology deals with materials whose characteristic scale is limited to the nanometer range (1-100 nm). This characteristic scale could be a particle diameter, grain size, layer thickness, or width of a conducting line on an electronic chip. Based on which one is the nanometric dimension, we can refer, for instance, to atomic wires (1-D nanostructures), thin films (2D nanostructures), nanoparticles, nanotubes, nanowires or nanoclusters (3-D nanostructures).

However, the real "key" to nanotechnology is the nanofabrication, i.e. the ability to actually *produce* various nanostructures and to *control* their macroscopic properties through a fine control of their nanometric constituents. In the last decades, several techniques have been exploited in order to produce nanostructures: scanning probe manipulation for single atoms or molecules, Molecular Beam Epitaxy (MBE) for thin film growth, driven self-assembly processes of several atomic and molecular layers, sol-gel processing, chemical vapor deposition and target sputtering for clusters deposition [Nanofabrication2008].

Clusters are essentially aggregates of atoms containing from a few up to thousands of atoms. As typical for many nanostructures, their small size makes their properties differ significantly from those of the corresponding bulk phase. These differences result from the fact that the number of atoms on a cluster's surface is a substantial fraction of the

number of atoms forming the cluster itself. Hence, the Surface-to-Volume Ratio (SVR) is dramatically higher for clusters compared to ordinary bulk-like samples, usually making them extremely more reactive. On the other hand, one should also consider the much smaller volume confining the electrons in the cluster with respect to the solid state. This implies that the electrons in the clusters will fill discrete levels, instead of having the band distribution typical of the solid.

Discerning when a cluster becomes big enough (i.e. contains a sufficient number of atoms) to behave like a solid is not a trivial point. This is because, most of the time, different properties of clusters and bulk materials "converge" at a different rate. Ideally, one would like to know the precise behavior of a given property (cluster geometry, ionization potential, melting temperature, etc.) as the number of atoms in the clusters increases one by one. These questions have motivated the development of experimental techniques that are able to finely control the growth small clusters.

In the last two decades, one of the most fertile techniques used to prepare nanoclusters films has been the Supersonic Cluster Beam Deposition (SCBD) [Milani1999]. For example, energetic cluster beam deposition has been used to produce high-quality coatings [Yamada1998], surface smoothing, and microstructuring [Henkes1995] and for shallow implantation [Yamada1998]. On the other hand, low-energy cluster-beam deposition has been used to produce nanostructured thin films retaining "memory" of the precursors, allowing a fine tunability of its physical and chemical properties [Barborini2005]. In the last years, SCBD has been successfully used to grow clusters of various elements and compounds (C, Pd, TiO_2, Fe_2O_3, WO_3, PdO_x [Wegner2006, Barborni2008, Chiodi2009, Barborini2005, Cassina2009]) with a high control of the nanometric constituents.

In this chapter we will describe the SCBD apparatus used to produce a TiO_x cluster beam and how the cluster source can be used to grow nanostructured doped and undoped TiO_x films in UHV conditions. We will then characterize the as-grown films showing how their cluster-assembled nature modifies their physical and chemical properties.

3.2 Supersonic Cluster Beam Deposition

The Supersonic Cluster Beam Deposition apparatus used to deposit the nanocluster films analyzed in this thesis is schematically depicted in Fig. 1. The source consists of essentially three different components. The first is the Pulsed Microplasma Cluster Source (PMCS), where the clusters are first created. The PMCS is connected to the expansion chamber, where the cluster beam is collimated and focused and, finally, the clusters reach a differential vacuum chamber that is used to connect the SCBD apparatus to a UHV deposition chamber.

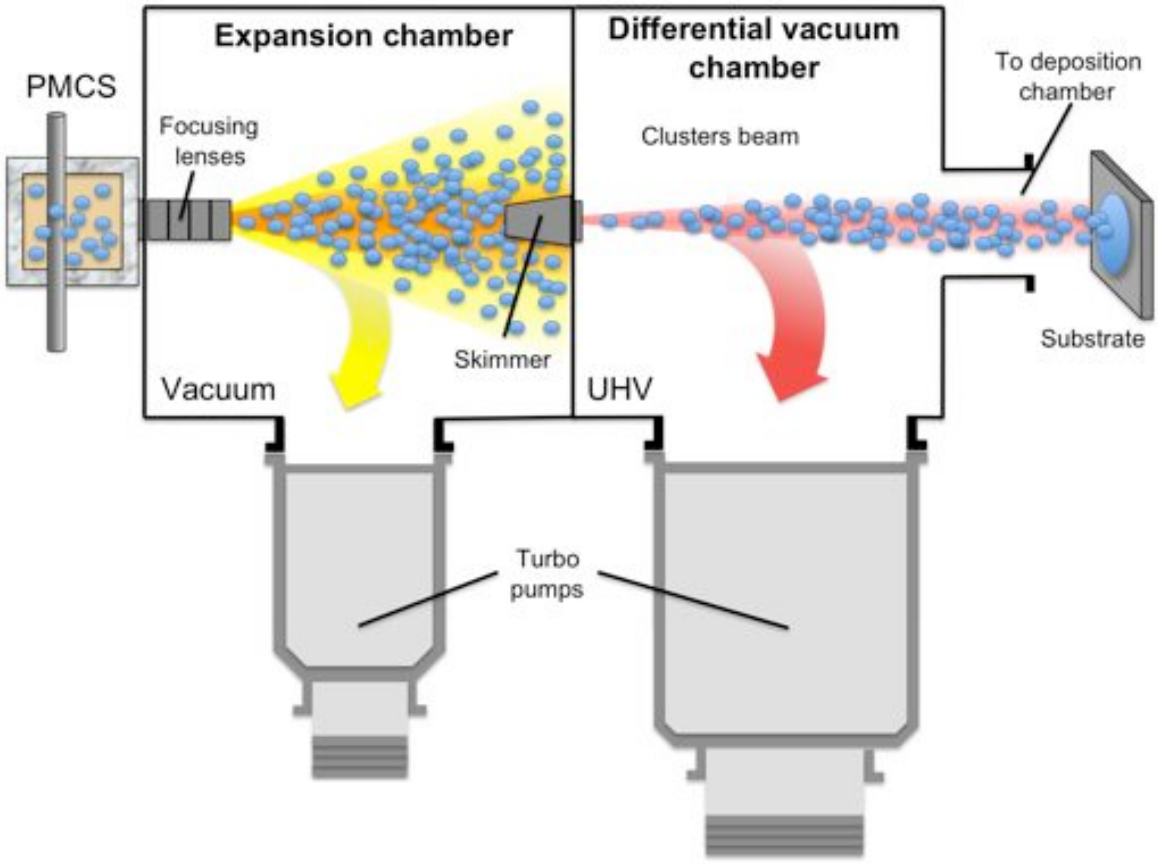

Figure 1 - Schematic representation of the cluster beam deposition apparatus.

The PMCS consists of a ceramic body with a channel drilled to intersect perpendicularly a larger cylindrical cavity. This channel hosts a high purity (99.999%+) rod of the material to be vaporized (Ti in our case). A solenoid pulsed valve (General Valve Corp., Series 9) is attached on one side of the cavity, while the other side is equipped with a removable nozzle. This valve allows the operation of the source in a pulsed mode. Even if the operation of a pulsed source could be more complicated compared to a standard continuous one, it presents several important advantages. First, the gas load injected inside the source is significantly reduced, allowing the compatibility with HV and UHV systems. Second, it is possible to finely control the gas pressure in the source region, where the cluster aggregation takes places. Third, the intensity of a pulsed molecular beam can be significantly higher than that of a continuous source operating in similar conditions (up to 1000 times higher) [Wegner2006].

The basic working principle of the PMCS is illustrated schematically in Fig. 2. It consists of a pulsed injection of an inert gas (He in our case) into the cavity, directed against the target. The solenoid valve, backed with a pressure of several bars, delivers the gas pulses with an opening time of a few hundreds of microseconds. The gas is then ionized by a high voltage, high intensity (~1000 V, 1000 A) pulsed discharge fired between the target rod (acting as a cathode) and the body of the source (anode). The discharge usually lasts a few tens of microseconds, and produces the ablation of the rod. The vaporized titanium atoms are quenched by the helium gas and condense into clusters. The cluster-helium mixture expands out from the source body through a nozzle to form a seeded supersonic beam. The velocity of the carrier gas is about 2000 m/s at the time the first clusters come out from the nozzle, but slows down to ~1000 m/s at the tail of the cluster pulse. A velocity slip of the clusters with respect to the carrier gas is also present, but becomes relevant only for clusters exiting late from the source.

In analogy with the case of laser vaporization sources [Milani1990], the use of a cavity, where the discharge and the aggregation of the clusters occurs, is important for several reasons. The erosion of the cathode does not significantly affect the dynamics of the gas during the expansion. Moreover, the cavity decouples the cathode ablation from the

clusters formation. The stability of the source is substantially improved and the electrode erosion affects mainly the intensity but not the mass distribution of the clusters [Barborini1999].

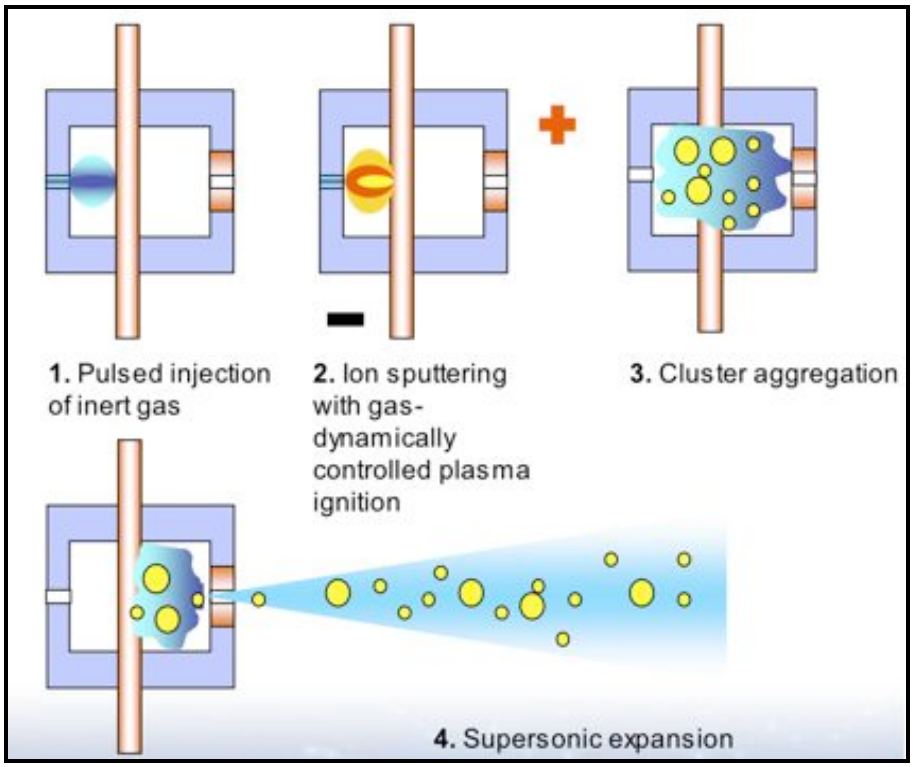

Figure 2 – Functioning scheme of the gas injection, plasma ablation and clusters formation inside the PMCS

The nozzle (see Fig. 3b and c) is constituted of two separate parts: the focuser and the cylindrical nozzle body. The first is a disk, 1.5 mm thick, with eight holes drilled on a circumference close to the disk edge. The second is a 10mm long cylinder whose external diameter matches the one of the focuser (i.e. 12mm), while the internal channel has a diameter of 2 mm. On the disk side facing the cylindrical nozzle, the plane is machined so that a narrow gap (~0.3 mm) is created between the two pieces when they are in contact (see Fig. 3b). As depicted in Fig 3d, this configuration causes

a sudden turn of the cluster-gas mixture flow exiting the PMCS. For suitable gas pressures, the clusters can travel different trajectories from the stream-lines of the carrier gas.

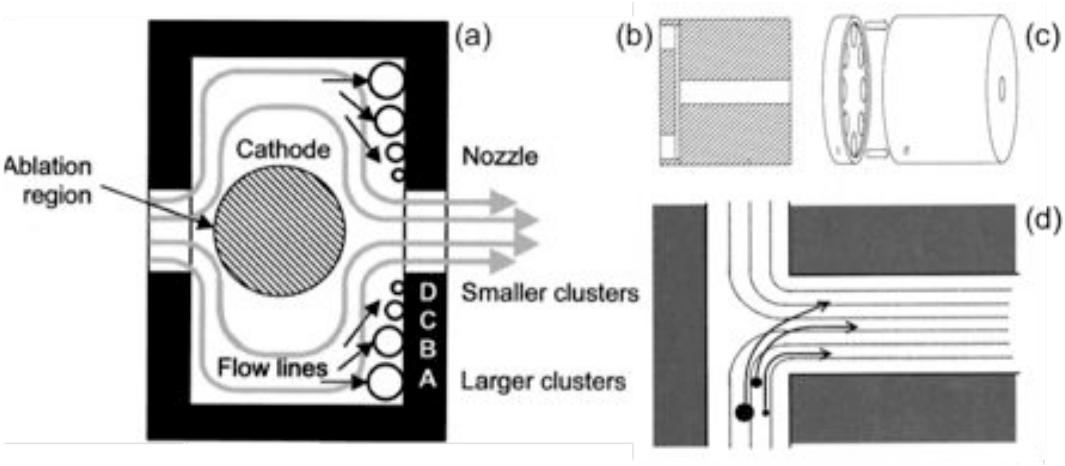

Figure 3 - (a) Cross-section view of the PMCS. Parts (b) and (c) show the focusing nozzle present at the end of the PMCS (cross-section and perspective view, respectively). (d) A sketched view of the focusing mechanism: at a given pressure only clusters with the selected size have trajectories leading to particle concentration close to the nozzle axis. Lighter particles closely follow the flow-lines of the gas, with no concentration effect. Heavier particles diverge after crossing the nozzle axis and eventually collide with the nozzle walls.

This separation is size-dependent, since it is due to the different inertia of the bigger and the smaller clusters (Fig. 4). Thus, the cluster with the selected size can be concentrated close to the beam axis direction using a specific carrier gas pressure injected in the PMCS. For lower pressures the particle trajectories can cross the nozzle axis and then diverge, while for larger pressures the particles are coupled to the gas stream-lines and thus no focusing takes place.

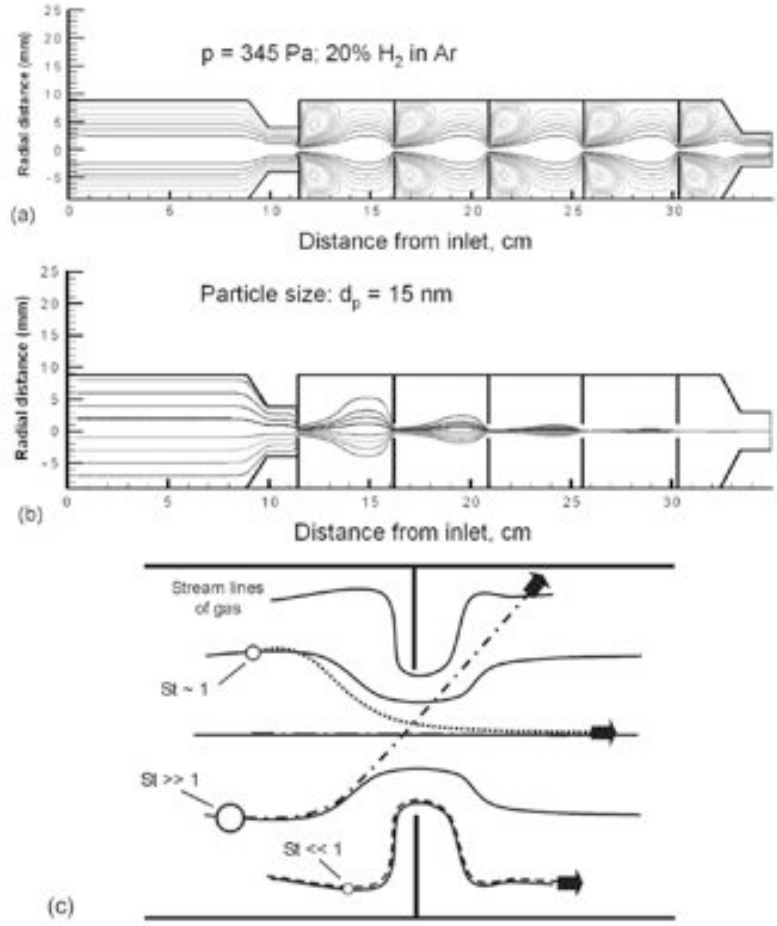

Figure 4 – Simulation of the gas flow (a) and trajectories of 15 nm particles (b) in an aerodynamic lens system according to Gidwani and Di Fonzo et al. [gidwani, difonzo]. The particles are concentrated at the center of the axis of the lens system, forming a beam. (c) Basic principle of aerodynamic size-selection and focusing.

The nozzle is then followed by a series of aerodynamic lens system like the one shown in Fig. 4. This part consists of a series of small apertures that enhance the molecular beam focusing process exploiting the size-dependent separation effect in order to concentrate the clusters of a chosen size in the center of the molecular beam. In fact, the inertia of large particles (St »1 in Fig.4) exceeds the drag action of the gas, separating the particles trajectories from the gas stream-lines and leading to wall collisions. Small particles (St «1) closely follow the flow. Intermediate particles have

trajectories only slightly decoupled from the stream-lines, which are used to concentrate them at the center of the molecular beam [Gidwani, DiFonzo].

At this point, the focused cluster beam enters into the differential pumping chamber through an electroformed skimmer of 2 mm diameter. The nozzle-skimmer distance is 40 mm and the average pressure in the expansion chamber under standard operation conditions is 2.0 – 8.0 10^{-5} mbar, while the pressure on the other side of the skimmer is around 10^{-8} mbar. Finally, this last chamber is connected to the deposition chamber through a gate valve that, once opened, allows the beam to reach the substrate chosen for the cluster-assembled film growth.

In our experiments, the residual oxygen partial pressure present in the PMCS, in the expansion chamber, and in the differential vacuum chamber was enough to partially oxidize the Ti clusters, giving TiO_x clusters (as confirmed by in situ measurements presented in the Chap. 3.3). This is due to the extremely high reactivity of this type of atom, that acts like an efficient getter even when kept in UHV conditions [chiodi2009].

This property has been further exploited to also deposit N-doped TiO_x clusters. Nitrogen dopants were introduced in the source's chamber as both air residual traces inside the PMCS body ($<10^{-3}$ mbar) and impurities diluted into the He flow. This choice had the enormous advantage of easily introducing N species, at the price of a lack in control over the amount of N present in the source when the clusters' aggregation takes place. The results of this simple doping technique are presented in the Chap. 3.4.

3.3 TiO_x nanoclusters on Si

3.3.1 Experimental

Nanostructured titanium oxide films were deposited by supersonic cluster beam deposition using a Pulsed Microplasma Cluster Source (PMCS). TiO_x films were deposited in UHV conditions at RT on both (001)- and (111)-oriented clean silicon surfaces. Before deposition, the Si substrates were cleaned by several flash thermal treatments up to 1000°C in UHV until no impurities were detected by Auger Electron Spectroscopy (AES) and X-ray Photoemission Spectroscopy (XPS), and a sharp Low Energy Electron Diffraction (LEED) pattern appeared [(2x1) and (7x7) LEED pattern, respectively].

The films were characterized *in situ*, right after deposition and/or thermal treatments via AES/XPS and Ultra-violet Photoemission Spectroscopy (UPS). AES spectra were acquired in integral mode using an Omicron Multiscan system, the XPS spectra using a non-monochromatic Mg X-ray source (photon energy= 1253.6 eV), while the UPS bands were obtained using a conventional He discharge lamp (photon energy= 21.2 eV). All the spectra were acquired at RT in normal emission geometry. The films were then annealed at different temperatures up to 1000°C for a period of 10 min. The nominal thickness and the deposition rate were measured *in situ* by a quartz microbalance. The film morphology was also characterized *ex situ* using an Atomic Force Microscope (AFM) (Solver-pro NT-MDT), acquiring the data under nitrogen flow in semicontact mode with nominal tip radius below 10 nm. The AFM was used to measure the actual film thickness at a border of deposited area of the sample surface. This allowed us to evaluate the extrapolated thickness obtained with the microbalance by comparison with the measured film thickness.

3.3.2 Morphological characterization of SCBD TiO_x films

The as-deposited titania film exhibits a uniform and porous morphology. The clusters are well resolved and no signs of fragmentation are evident from the AFM image shown in Fig.2. This is a common feature in SCBD films, regardless the type of compound deposited. In fact, C and PdO_x films deposited with the very same technique exhibit a very similar structure (see Fig.3) [Milani2000,Cassina2009].

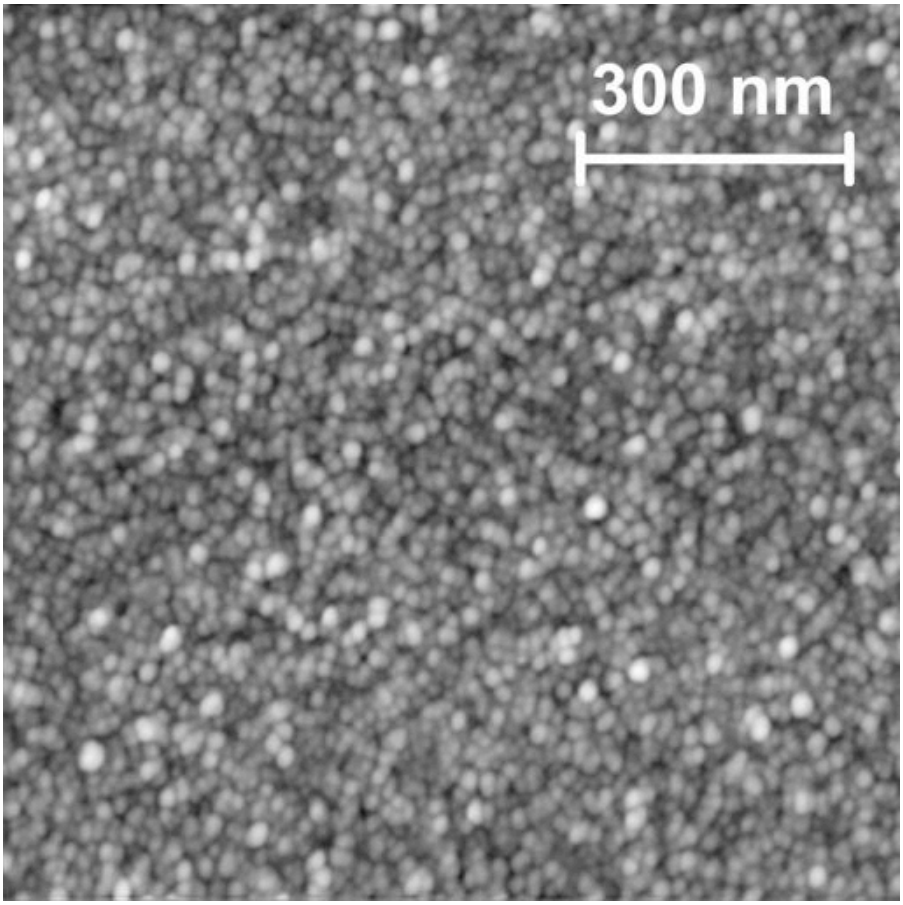

Figure 5 - AFM image of the titania film deposited on Si(001) substrate at room temperature (Area: 1x1 μm^2)

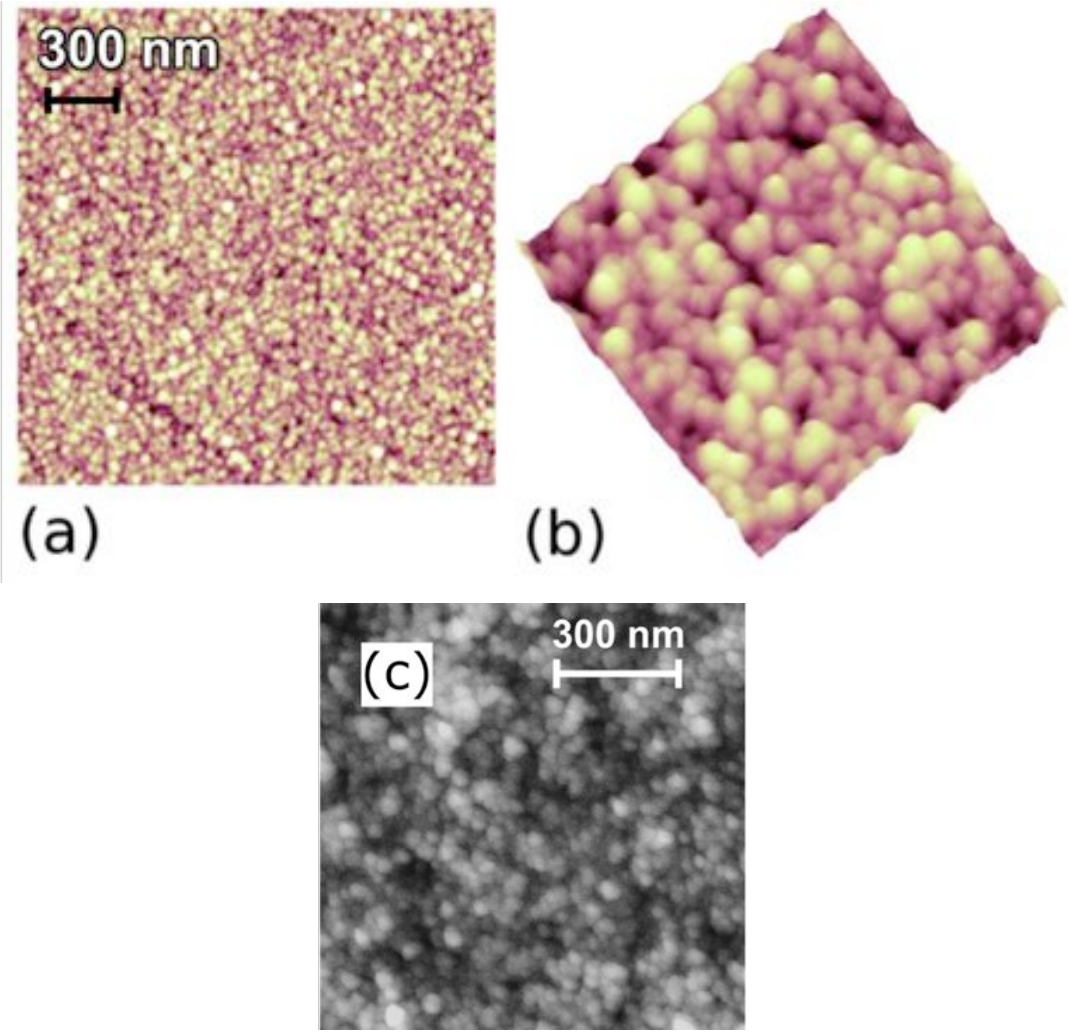

Figure 6 - (a) and **(b)**: AFM images taken on a PdO_x SCBD film (Area (a)= 2x2 μm^2; Area (b)= 500x500 nm^2) [Cassina2009]. **(c)** AFM image of a carbon SCBD film (Area= 1x1 μm^2) [Milani200].

The clusters exhibit an almost circular shape, with an average lateral size of (10.7 ± 2.1) nm, which should be considered as an upper limit since it corresponds to the curvature radius of our AFM tip. The largest cluster size observed is 15 nm. This result confirms that the PCMS can produce a homogenous cluster beam with a narrow size distribution [Milani2000, Barborini1999].

Our measured nanoparticle size is remarkably smaller than what is reported in literature for other titanium and titanium oxide films obtained with other deposition techniques. In particular, the grain size of stoichiometric TiO_2 prepared by magnetron sputtering is several tens of nanometers [Hou2003] (Fig. 3b) and ranges from 10 to 100 nm for electron-beam deposited Ti films on Si [Kuri2002] (Fig. 4a). Note also that RMS roughness of our 10-nm thick film is 2.9±0.1 nm, i.e. very similar to the roughness of much thinner (~1 nm) films obtained with traditional deposition techniques [Huo2003, Kuri2002].

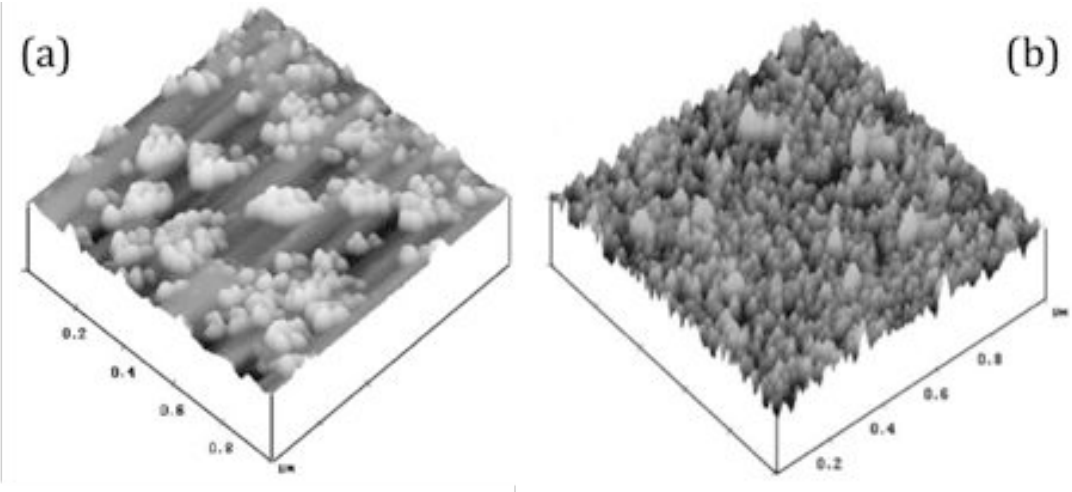

Figure 7 - (a) AFM image of a Ti-covered Si(111) specimen prepared using an electron-beam evaporator. The nominal thickness of the film is 1.8 ML (Scan area= 1x1 μm^2) - **(b)** AFM image of a TiO_2 film deposited with ac magnetron sputtering (Scan area= 1x1 μm^2) [Kuri2002].

These data suggest that the deposition of titania cluster by supersonic beam is much more effective in obtaining a film with lower grain size when compared to standard deposition techniques. This might be explained by a lower diffusion coefficient of the nanoclusters on clean silicon with respect to sublimated titanium adatoms.

3.3.3 Chemical composition

The chemical composition of the nanostructures films deposited at RT has been analyzed *in situ* through AES. The lineshape of the Ti $L_3M_{2,3}V$ transition centered around 415 eV is presented in Fig. 4. The data have been background subtracted following the procedure outlined by Sickafus [Sickafus1979] and then fitted with a least square fitting procedure using three pseudo-Voigt functions. The full width at half maximum (FWHM) of each component has been kept fixed at 4.4 eV, with a Lorentzian contribution of 2.1 eV. Three components can be safely indentified at 416.2, 413.0 and 409.6 eV kinetic energy (KE), respectively.

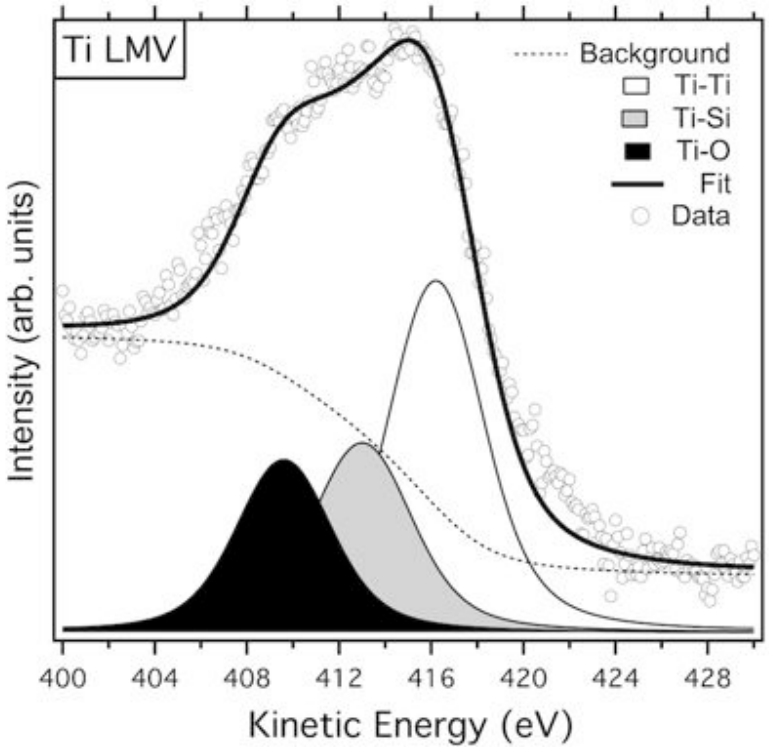

Figure 8 - Ti $L_3M_{2,3}V$ Auger line taken on the as-deposited film. The solid line represents a numerical fit based upon the superposition of three distinct peaks attributed to titanium atoms interacting with oxygen (black peak), silicon (gray) and titanium (white).

The high KE peak is due to Ti primarily involved in Ti-Ti metal-like bonds and the low KE component at 409.6 V to Ti atoms bonded to oxygen [Contarini2002]. At this point the origin of the third component at 413 eV can tentatively be attributed to the presence of Ti atoms interacting with Si at the film/substrate interface. This assumption is corroborated by the XPS presented in Fig. 9, where the Si 2p core level peaks taken before and after the TiO_x cluster deposition are presented (note that the spectra have been normalized to the same intensity for sake of clarity). The main peak is shifted by 0.2 eV towards lower binding energies, compatible with some sort of interaction taking place between the film and the substrate or a band-bending effect [Kittel1996]. Moreover, the Si 2p peak after deposition is centered at 99.2 eV, which is consistent with the formation of TiSi, as discussed by Larciprete et al. for Ti/Si(001) [Larciprete2001]. It is also worth to note that the Si 2p core level spectrum does not present any component around 104 eV, which is typically related with Si-O interaction. This is also confirmed by the AES lines and XPS O 1s spectrum which do not show any features related to silicon oxide nucleation (see also Cap. 3.3.3 – Fig. 8). Thus, we exclude any SiO_2 formation at RT.

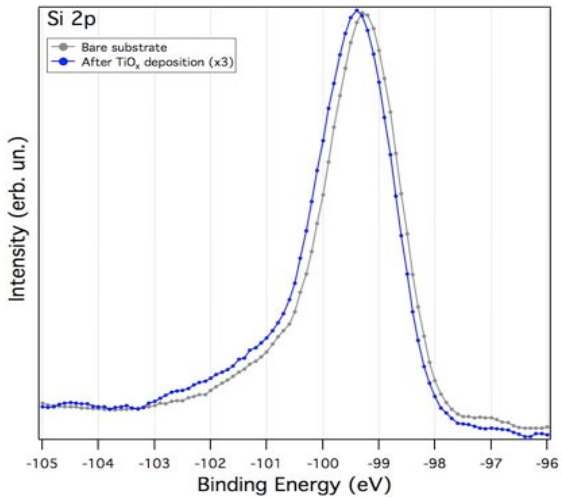

Figure 9 - Si2p XPS spectra taken on the bare substrate (grey) and after the TiOx deposition (blue).

A quantitative analysis of the AES measurements has been carried out in order to estimate the chemical composition of the film. From the integral intensities of the Ti $L_3M_{2,3}V$ spectrum, we estimated that 50% of the titanium is present in metal-like form, 25% is involved in Ti-O bonds and the remaining 25% is due to TiSi. Along with the Ti $L_3M_{2,3}V$ Auger line, the Si $L_{2,3}VV$ at 92 eV KE and the O KLL at 505 eV KE spectra have been collected (not shown). The comparison between the peak areas corrected for elemental sensitivity [Mroczkowski1985] allows us to identify the as-deposited film composition. The stoichiometry can be estimated by considering the electron mean free path (λ) of a particular Auger peak in a uniform film [Shimizu1983]. However, the nanostructured nature and the high porosity of the present system make this point not trivial, because λ is unknown for this kind of film structure. The estimated dimension of a single titania cluster is at least 3 nm [Barborini2003], and the AFM data show that in this 10-nm thick film more than 90% of the substrate is covered by clusters. Therefore, we estimate the expected substrate contribution to the Si Auger intensity not to be greater than 10%. In pure, non-nanostructured Ti, electrons with kinetic energy of 90 eV (i.e. the KE of the Si $L_{2,3}VV$ line) have a λ lower than 0.5 nm and even shorter in pure TiO_2 [Lesiak2006, Fuentes2002]. By weighting the Si Auger line intensity with such considerations, we obtain an upper limit for the Si contribution to the film stoichiometry, which results in a composition of Si (47%) and O (40%), while the amount of Ti is around 13%. We have no evidence of oxygen bonded to silicon; hence, the discrepancy between the oxygen amount bonded to Ti and the total oxygen observed in the film is likely due to the extremely high reactivity of the nanoclusters. This suggests that even in UHV conditions they are acting as an efficient getter of residual water. We also note that some error in the total stoichiometry can be induced by applying a quantitative analysis procedure typically used for well-ordered thin films to a cluster-assembled layer.

Everything considered, the percentage of silicon within the deposited film still results to be remarkably high, indicating a huge diffusion of the Si atoms from the substrate

through the nanostructured film even at RT. We attribute this enhancement of the Si mobility to the high porosity of the cluster-assembled film.

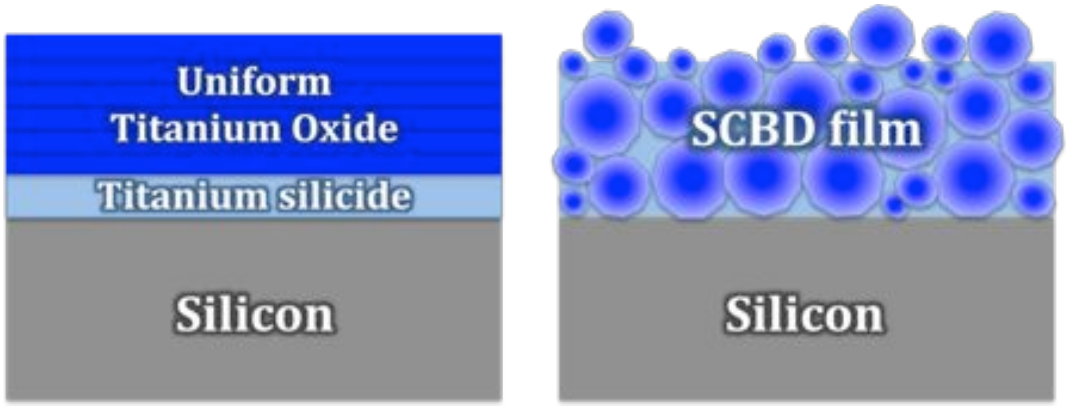

Figure 10 - Schematic view of the typical structure of a uniform film where just the very first layers are affected by any silicide formation (left). While a SCBD film allows a stronger Si diffusion and hence an extensive silicide nucleation (right).

Moreover, the enhanced Si diffusion can also be responsible for the extensive RT TiSi formation suggested by the XPS and AES data discussed before. In fact, a room temperature silicide nucleation has already been observed for several uniform Ti and TiO_2 films deposited on Si substrates [Jeon1992, Wang1991, Butz1984]. However, this process is usually limited to the very Ti-Si interface, since this interfacial silicide layer acts like a self-limiting barrier against the Si diffusion and therefore restraining the silicide thickness to just a few atomic layers [Chambers1987, Arranz2005]. The highly porous structure of our SCBD films avoids the formation of such a silicide barrier, thus allowing a much more extensive TiSi nucleation (Fig. 6).

3.3.4 Effects of thermal treatments

A comprehensive spectroscopic analysis (XPS, UPS, AES) has been carried out to investigate the film stability and chemical composition as a function of the annealing temperature. Fig. 7 shows the evolution of the Auger Ti $L_3M_{2,3}V$ lineshape at selected annealing temperatures, together with the least squares fitting results. The Si and O AES lines are not presented since most of the information on the nanostructured film evolution can be extracted from the analysis of the Ti excitation line.

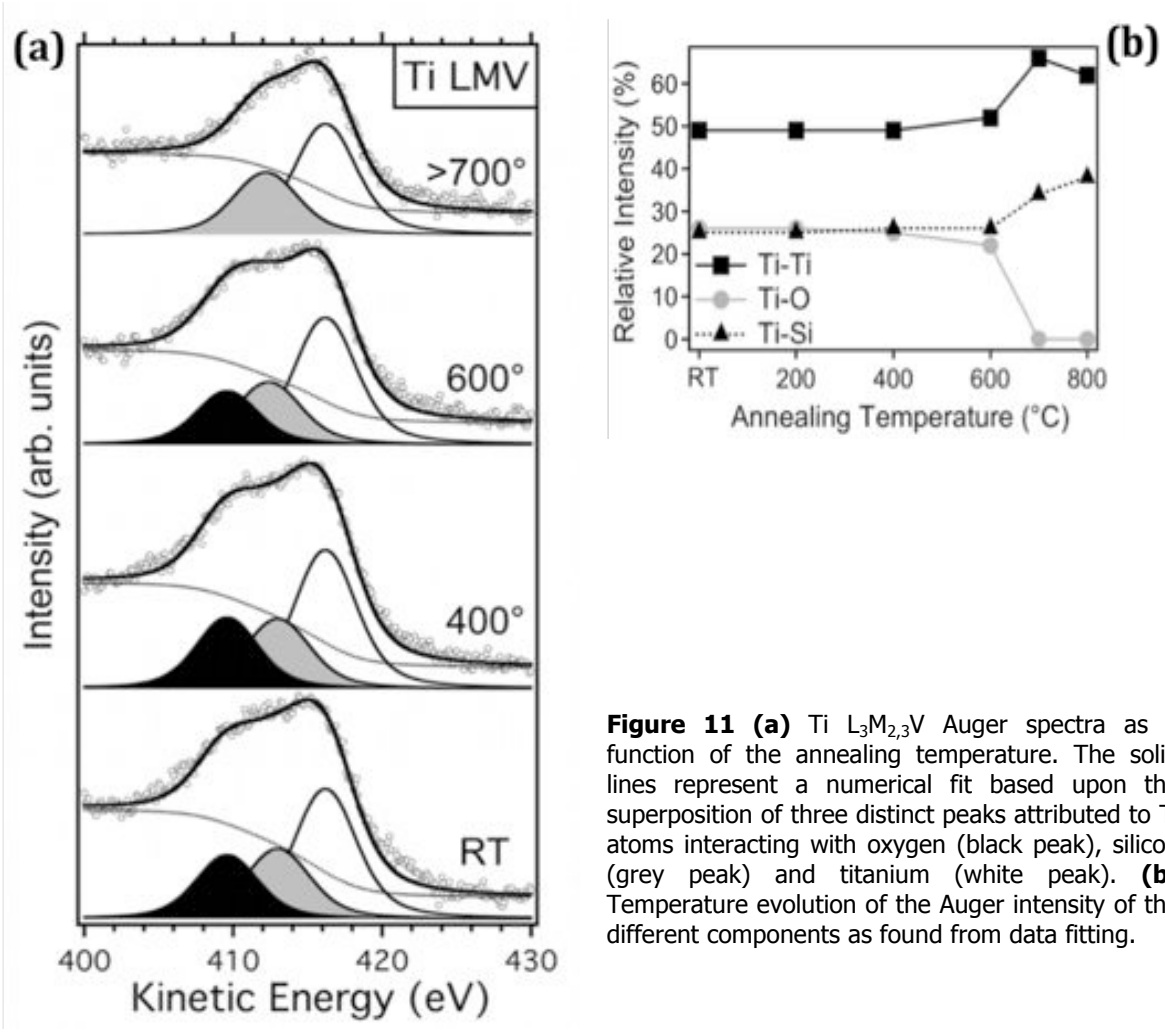

Figure 11 (a) Ti $L_3M_{2,3}V$ Auger spectra as a function of the annealing temperature. The solid lines represent a numerical fit based upon the superposition of three distinct peaks attributed to Ti atoms interacting with oxygen (black peak), silicon (grey peak) and titanium (white peak). **(b)** Temperature evolution of the Auger intensity of the different components as found from data fitting.

The AES lineshape remains essentially unchanged up to 600°C. At this temperature a slight decrease in the Ti-O component intensity (black peak in Fig. 7) is observed, along with an increase of the Ti-Ti peak intensity (see Fig. 7b). Beyond this limit the Auger spectrum suffers major variations, with the oxygen-related peak completely disappearing as the component ascribed to Ti-Si increases in intensity. Moreover, the latter component suffers a 0.5 eV shift towards lower KE. Fig. 7b also confirms that above 600°C the film undergoes some changes in the chemical composition. Both the metallic Ti and the Ti-Si components increase in the relative intensity, suggesting that the Ti atoms bonded to oxygen partly become metal-like Ti and partly bond to silicon.

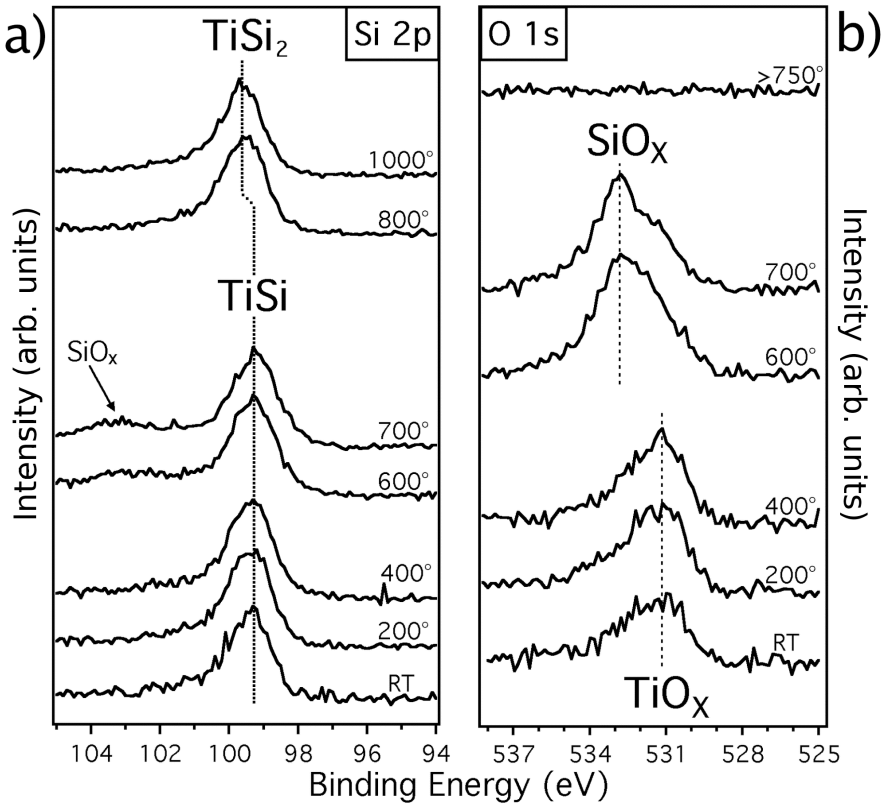

Figure 12 XPS Si 2p **(a)** and O 1s **(b)** core level photoemission spectra for a SCBD TiOx film deposited on a Si(111) substrate as a function of the annealing temperature. The spectra are normalized to the photon flux.

More information can be gained looking at the corresponding Si 2p and O 1s XPS spectra presented in Fig. 8. Both lines remain essentially unchanged in the RT-500°C annealing range. At 600°C, a component appears around 103.5 eV in the Si 2p, indicating the formation of silicon oxide [Seo2006]. This is also confirmed by the presence of a new component at 532.9 eV in the O 1s XPS spectrum [McCurdy2004]. The oxygen evolution from Ti-O towards Si-O bonding has been reported and discussed in details before [Nemanich1985], and a full understanding of this process can be gained by considering the ternary phase diagram. In fact, calculations based on thermodynamic properties of the three phases (Si-Ti-O) indicate that the only stable oxide at 600°C is SiO_2 [Beyers1984]. Also the XPS data confirm that the film chemical composition changes as the temperature exceeds 700°C. The oxygen is completely removed from the system (Fig. 8b) due to the sublimation of the SiO_2 previously formed. At the same time, the Si 2p peak shifts towards higher BE at 99.6 eV. This shift suggests that the TiSi is converted into $TiSi_2$ [Larciprete2001].

The thermal evolution of the Valence Band (VB) photoemission data presented in Fig. 9 is consistent with the contemporary presence of TiO_x, metallic Ti and TiSi at RT. The broad feature around 5.8 eV is due to the O 2p levels of TiO_x [Le Fevre2004], and the states in the 0-2 eV BE range with a sharp cut-off at the Fermi edge are related to both the semi-metallic character of the titanium silicide (around the Fermi level) and to the non-stoichiometric TiO_x (states around 1 eV BE) [Caruso2008]. When the temperature reaches 600°C, a broad peak appears around 7.3 eV, originating from the Si-O interaction [Kim2003]. Finally, at 800 and 1000°C, all the oxygen related features disappear and the VB spectra present a quite sharp component centered at 1 eV, due to the hybridization of Ti 3d and Si 3p states in $TiSi_2$ [Butz1984, Arranz2005].

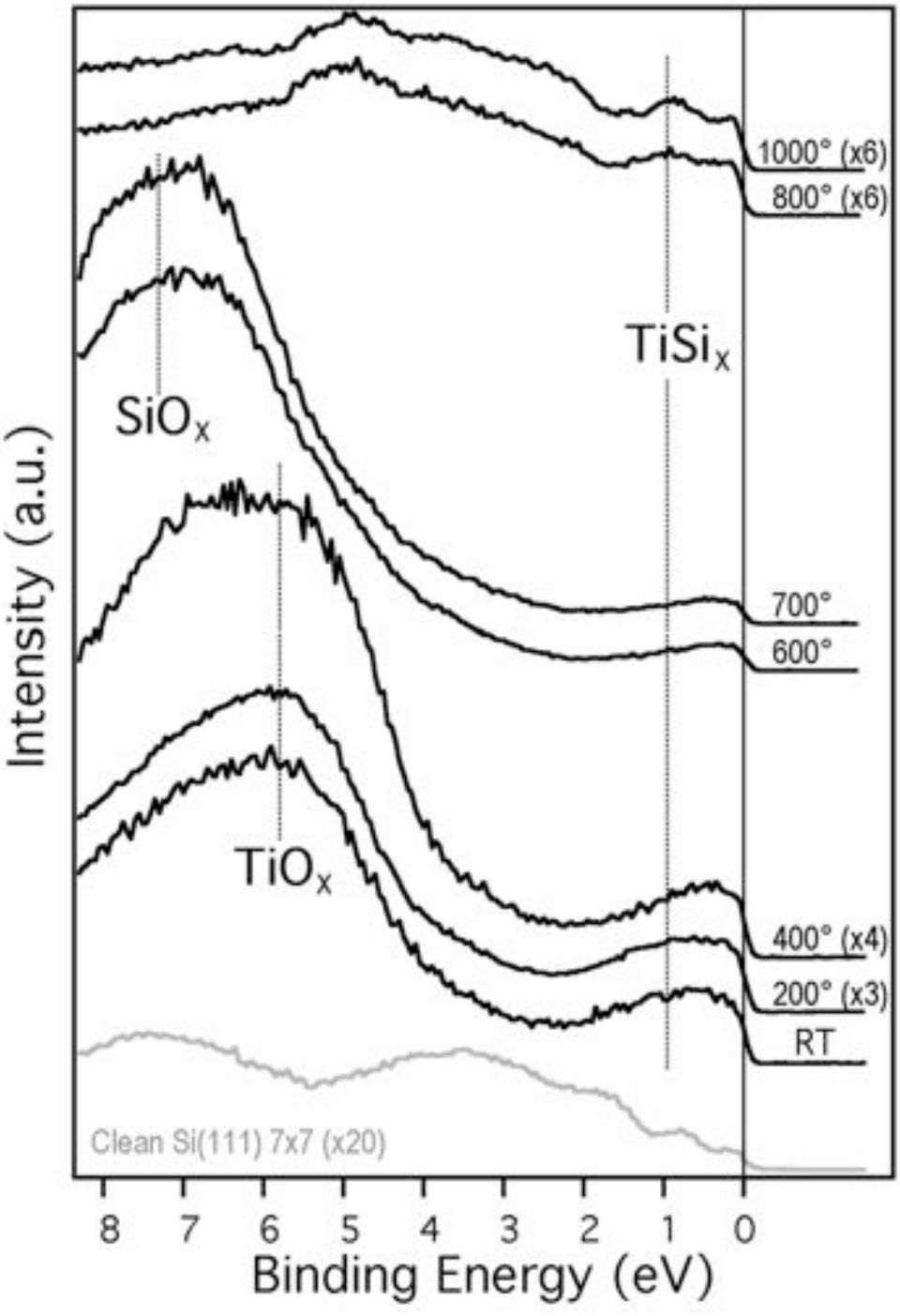

Figure 13 Valence Band photoemission spectra plotted with respect to The Fermi level. Normalization coefficients to the photon flux are reported on the right side along with the annealing temperature.

The AFM image of our SCBD film after the annealing treatment in UHV at 1000°C (Fig. 10) reveals that the surface morphology suffered only marginal variations. The RMS roughness of the film (~4.5 nm) remains in the same order of magnitude as before the annealing, while there is an increase of the average clusters' lateral size up to 22.6 ± 3.2 nm, indicating the coalescence of smaller clusters. This process could also involve a partial dewetting of the film that could explain both the appearance of small regions in which the silicon substrate is left uncovered (black areas in Fig 10) and the increase of the Si 2p/Ti 3d XPS intensity ratio at this temperature (not shown).

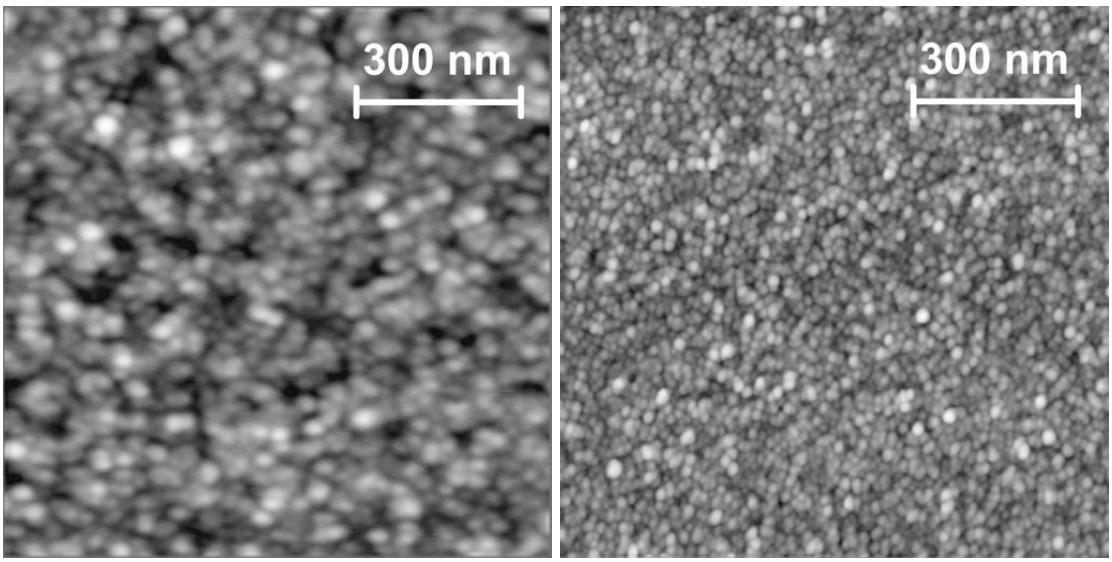

Figure 14 – (left) AFM image taken on the titania films deposited on Si(001) after being annealed in UHV conditions up to 1000°C (Area: 1x1 μm^2). On the right: the AFM image taken on the as-deposited film, before the annealing treatment.

A comparison with the previous works on Ti/Si interfaces suggest that the morphology of our nanostructured film is by far the most stable upon temperature variations. In fact, oxygen-free Ti/Si interfaces heated in UHV beyond 500°C show rough surfaces, with grains whose lateral size reaches hundreds of nanometers [Ohmi1999]. In $TiSi_2$ films obtained by rapid thermal annealing in UHV beyond 800°C the average grain

diameter is ~110 nm, five times larger than our result. For $TiSi_2$ films synthesized with pulse-laser irradiation, the value is ~85 nm [Chen1999]. Moreover in partially oxidized TiO_x/Si interfaces (grown by means of RF sputtering) Ilango el Al [Ilango2005b] found that the RMS roughness suffers a steep increase after a vacuum annealing beyond 500°C, reaching a value of ~50nm at 800°C with an average grain size of ~42 nm [Ilango2005a].

Such a film roughening upon thermal treatment is observed by Hou et al [Hou2003] in stoichiometric TiO_2 films as well. They measure a RMS roughness varying between 18.9 and 43.5 nm at 900 and 1100°C, respectively, with an average grain size ranging from 300 nm up to 1-3 μm. Hence, the previously investigated Ti-Si systems exhibit a strong tendency towards roughening upon temperature variation, irrespectively of the different deposition conditions. On the contrary, our SCBD film is the least affected by this process, and this is likely to be related to the stability of cluster-assembled structure, which prevents an extensive coalescence of the smaller clusters.

3.3.5 Conclusions

In this section we showed that SCBD can be effectively used to deposit nanostructured TiO_x films on silicon. The reactivity of the as-deposited films is extremely high, much higher than what found for titania films grown with standard techniques. This enhanced reactivity, along with the highly porous structure of the film, contributes to an unusually extended silicide formation even at RT. Moreover, the nanostructured film morphology exhibits a high stability against roughening upon temperature variations up to 1000°C.

Both the porous structure and high reactivity of the SCBD TiO_x films make them the perfect candidates for efficiently incorporating dopants atoms in the titania matrix.

3.4 N-doped TiO_2 SCBD films

In chapter 3.3 we investigated in detail the structure and the properties of a TiO_x film, showing how the nanoclusters' high reactivity can trigger chemical reactions that normally do not take place in standard systems and interfaces. Moreover, this is achieved while preserving a remarkable morphological stability of the film structure.
In this chapter we will discuss how this extremely high reactivity can be exploited in order to introduce selected atomic dopants (N atoms) in the TiO_2 film structure, and how the system's properties change as a consequence of the doping process.

3.4.1 Experimental

Nanostructured N-doped TiO_x films were deposited by SCBD using a Pulsed Microplasma Cluster Source (PMCS). N-TiO_x films were grown in UHV conditions at RT on different substrates (Si(001), $LaAlO_3$ and Al_2O_3) depending on the different needs of the various experimental techniques used for the investigation of the grown film. Before deposition, the insulating substrates were cleaned by cycles of sputtering (Ar^+ ions, E_{kin}=1000 eV) and annealing (up to 500°C) in UHV conditions. The silicon wafer was cleaned by flash thermal treatments up to 1000°C in UHV until no impurities were detected by AES and XPS.
The films' chemical composition was then characterized *in situ* right after deposition using XPS. The samples were then left for 10 hours in a separate chamber (base pressure <1x10^{-6} Torr) subsequently filled with high purity (99.999%) O_2 atmosphere (p= 1 bar), in order to completely oxidize the film. The samples were then re-checked with XPS to ensure that a complete oxidation was obtained.
The films were then characterized *ex situ* by means of X-ray Photoemission Spectroscopy (XPS), Resonant X-ray Photoemission Spectroscopy (RESPES) and Near-Edge X-ray Absorption Fine Structure Spectroscopy (NEXAFS) at the Spectro-microscopy lab at the University of Tennessee, Knoxville, TN (USA) and at the APE beamline at the

Elettra synchrotron radiation facility in Trieste (Italy). After the insertion in the experimental chamber through a fast entry-lock, the samples were degassed for ~1h at 100°C. During the experiments the pressure in the chamber was kept below 1 x 10^{-10} mbar. XPS measurements were conducted using an Omicron multiscan system equipped with monochromatized Al K-alfa X-ray source (hv= 1486.7 eV). The spectra were acquired in normal emission using an Omicron multichannel setector.

At the APE beamline, the data were acquired using an Omicron photoelectron analyzer, the photon energies used ranged from 390 eV up to 1486 eV, as set from the beamline monochromator, and were calibrated using an Au plate as a reference.

The NEXAFS spectra were acquired in Total Electron Yield (TEY) in order to maxime the bulk-sensitivity of the measurements. [Apewebsite]

3.4.2 Chemical characterization

An accurate XPS analysis was carried out in order to investigate the chemical composition, to establish the effective amount of nitrogen introduced in the sample, and to verify whether it was substitutionally or interstitially embedded in the cluster-assembled film.

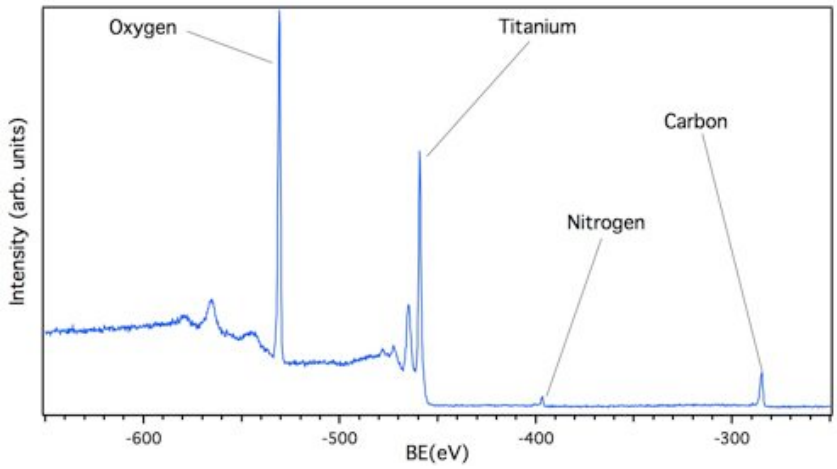

Figure 15 - XPS large scan taken on the N-doped TiO_2 nanoclusters.

The large XPS scan presented in Fig. 11 confirms the presence of the N atoms in the film, along with carbon contamination. The previous XPS data sets acquired *in situ* right after the deposition showed no C presence. Thus, we attribute the C 1s signal measured at APE to the exposure to air during the transportation from the deposition chamber to the beamline. Nonetheless, we can exclude that carbon impurities could somehow alter the following characterizations, since it is well know that C coming from the atmosphere remains inert on the SCBD TiO_2 films up to 800 °C [Barborini2005].

A close inspection of the N 1s core level presented in Fig. 16 allows us to identify two distinct components contributing to the spectrum. A quantitative analysis has been carried out by means of a least squares fitting procedure involving the convolution of two Gaussian components (FWHM= 1.0 and 1.7 eV for components **s** and **i**, respectively) over a polynomial background.

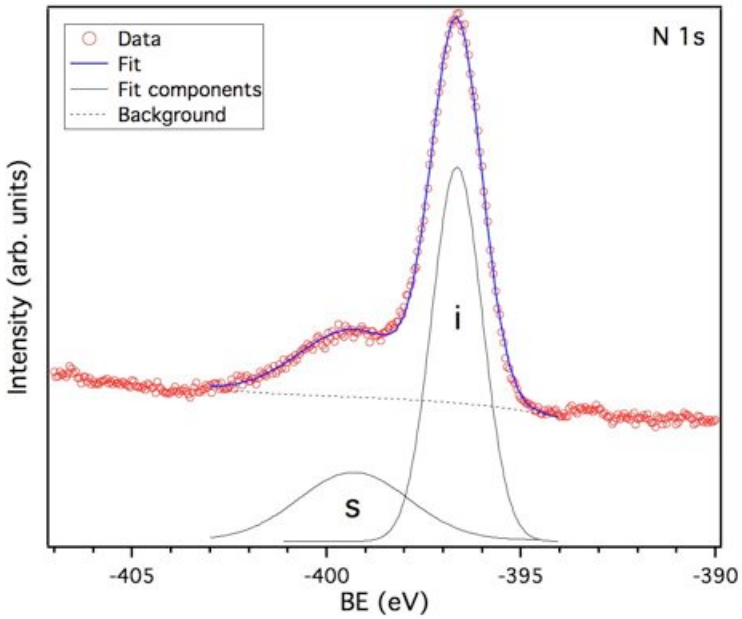

Figure 16 - N 1s core level spectrum (o) on N-TiO_2 nanoclusters along with a numerical fit (—) based on the superposition of two Gaussian components (—) over a polynomial background (- - -)

By comparison to many different works in literature [among the others see Saha1992, Asahi2001, BatzillPRL2006], we attributed the component centered at 399.6 eV (**i** in Fig. 16) to interstitial dopants and molecular N physisorbed on the surface. The second component (**s**) found at 396.8 eV is ascribed to N^{3-} species primarily involved in Ti-N bonds, suggesting that nitrogen is substitutionally embedded in the TiO_2 film. Moreover, the intensity ratio between the two components is estimated to be ~5.5. These results indicate that most of the N atoms are successfully incorporated into the cluster-assembled film in substitutional sites, while only ~18% is present in interstitial sites or physisorbed on the film surface. It should also be noted that the sample has been measured *ex situ*, i.e. some of the N atoms are residuals originating from air exposure during transportation. This is also confirmed by a comparison with the XPS data taken *in situ* right after the deposition (not shown here). Following the quantitative analysis procedure outlined in Chap. 2, we finally estimated the atomic concentration of N effectively incorporated in the film. We found this concentration to be ~4%.

The Ti 2p core level spectrum presented in the top panel of Fig. 17 exhibits the typical multi-peak structure with two main lines due to spin-orbit splitting of the Ti 2p level centered at 459.2 ($2p_{3/2}$) and 465.0 eV BE ($2p_{1/2}$), respectively. The same two structures are also replicated ~13 eV towards higher BE, due to plasmon losses. Moreover, a shoulder is clearly visible at lower BE with respect to the main Ti $2p_{3/2}$ peak. This peak is located at 457.55 eV and its intensity is ~12% of the main Ti^{4+} peak. The presence of this component is a clear indication of Ti^{3+} species [Diebold2003]. The assignment of this peak in N-doped TiO_2 is somewhat complicated since it can be related to both Ti-N-O bonds [Diebold2003] and oxygen vacancies [BatzillPRL2006]. Nonetheless, considering that we estimated the N concentration to be ~4%, most of the contribution to the Ti^{3+} should be ascribed to oxygen vacancies. In order to further elucidate the origin of the latter contribution, a Valence Band (VB) photoemission spectrum has been acquired (Fig. 17 bottom). In fact, oxygen vacancies in TiO_2 also induce a distinct peak in the proximity of the Fermi level (~1 eV BE) due to unhybridized Ti 3d states [CarusoAPL2004].

The valence band spectrum shows the most intense features between 4 and 9 eV BE. This region is populated by the bonding O 2p – Ti 3d hybridized states. Moreover, a less intense but still detectable peak is found around 1 eV BE (see the magnification in Fig. 17 bottom). This indicates that our SCBD film possesses native defects as oxygen vacancies that contribute to the low-energy shoulder found in the Ti 2p core level spectrum (Fig. 17 top). Thus, the Ti^{3+} component should be interpreted as originating from both oxygen vacancies and Ti-O-N bonds related to the film doping.

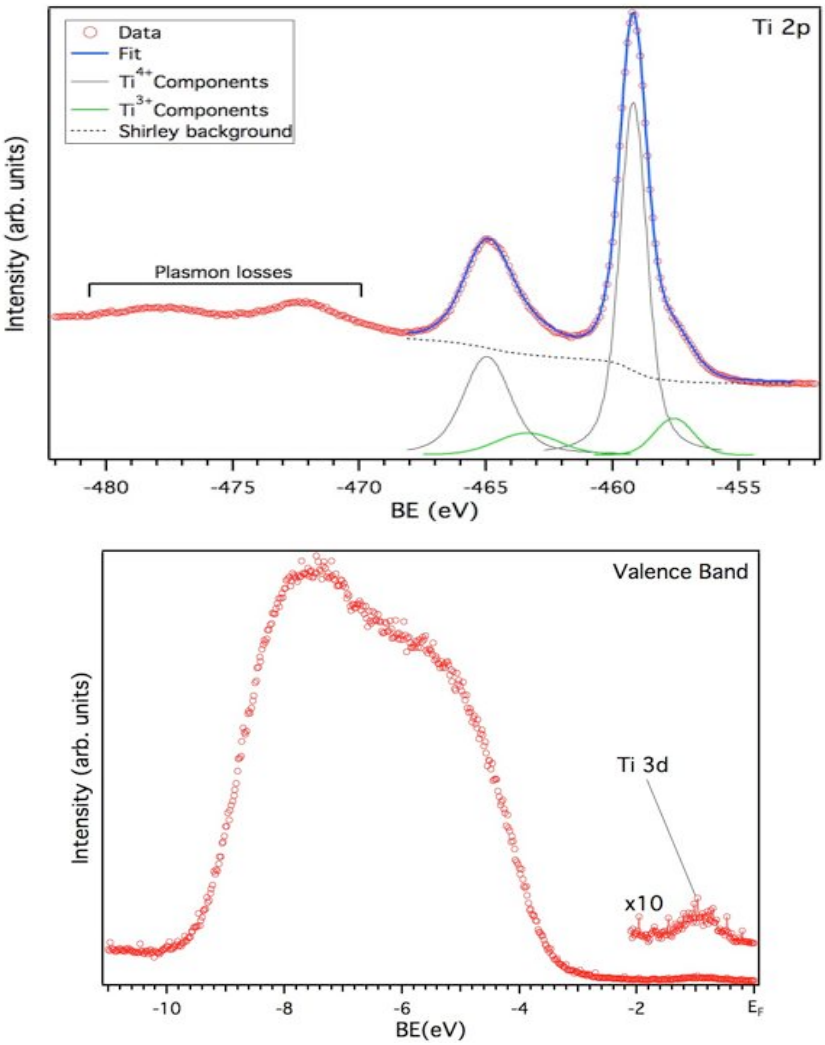

Figure 17 – (top) XPS Ti2p. (bottom) Valence band.

A comparison between the VB spectrum acquired on the N-TiO_2 clusters sample and a reference spectrum taken on a PLD undoped TiO2 sample (with mixed anatase and rutile phases) allows us to discuss the differences introduced in the VB states by both the cluster-assembled structure and the N-doping of the film. In the undoped TiO_2 film, the lineshape of the main structure between 4 and 9 eV BE resembles the one measured for the N-TiO_2 clusters. The main peak is found at ~8 eV BE, with a second, less intense peak around 5.8 eV. These features appear to be smeared out in the SCBD spectrum: the major peak is still visible around 7.8 eV BE while the second is present only as a broad shoulder around 5.6 eV BE. This kind of broadening of the VB structures is not surprising, considering the structure of our SCBD film. In fact, its cluster-assembled nature is expected to induce much more disorder in the film with respect to the standard TiO_2, smearing out the VB states.

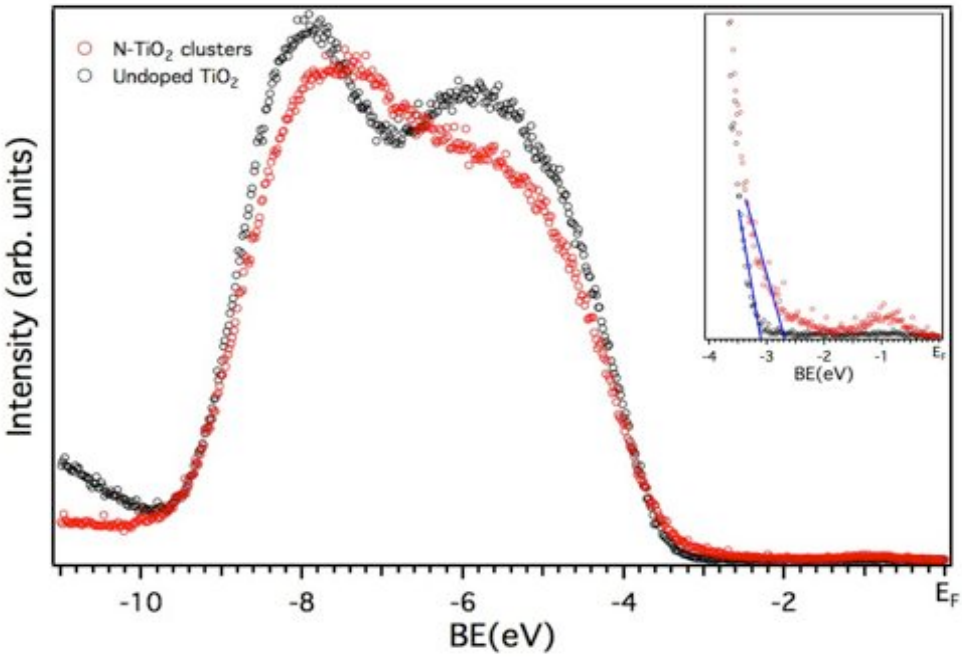

Figure 18 - XPS valence band spectra taken on SCBD N-TiO2 film (o) along with the same spectrum taken on an undoped TiO_2 film (o). In the inset a magnification of the top

of the VB is presented. A shift of the top of the VB is evident in the N-TiO_2 system (the two solid lines are a guide to the eye).

A more accurate inspection of the two spectra reveals that another difference is present at the very top of the VB. Looking at the inset of Fig. 14, it is evident that the N-doped clusters film exhibits a shift of the top of the valence band of ~0.4 eV. Interestingly, impurity states located in the same BE region were found in several N-TiO_2 systems [BatzillPRL2006, Asahi2001, Nambu2006]. Those states have been assigned to N 2p originating from N^{3-} species substituting lattice O^{2-} [BatzillPRL2006]. Moreover, in a previous VB spectroscopy study of an analogous undoped SCBD titania film, no significant shifts of the VB cut-off were found [Caruso2007]. Thus, we can safely exclude that this impurity band could be related to the cluster-assembled structure. On the contrary, we conclude that the N-doping is responsible for the states at the top of the VB. It remains unclear, at this level, whether these states could contribute to the shrinkage of the band gap since we do not know the shape and the energy position of the empty states in the Conduction Band (CB) with respect to Fermi level. Thus, we also carried out X-ray Absorption Spectroscopy (XAS) measurements presented in the next paragraph.

3.4.3 Conduction band analysis: NEXAFS data

The local symmetry and the chemical environment surrounding Ti, O, and N atoms have been investigated by x-ray absorption spectroscopy. Three different sets of NEXAFS spectra were acquired on the SCBD N-TiO_2 film using unpolarized photons whose energies were close to the O K-edge, Ti L-edge and N K-edge threshold, respectively. The results are presented in Figs. 19, 20, and 21 along with reference spectra taken on a PLD undoped TiO_2 sample (only for the Ti and O absorption edges).

The O K-edge spectra exhibit two main structures centered at ~531 and ~?534 eV, along with additional structures at higher energies. As shown by de Groot [deGroot1993], O K-edge NEXAFS spectra can be well explained with single-electron approximation models. These spectra essentially map the O 2p-projected density of empty states in TiO_2. Correlation effects appear to have a negligible influence on the O K-edge spectra since O 2p states are hybridized and relatively delocalized, resulting in a weak interaction with the O 1s core hole.

In a Molecular Orbital (MO) picture of undoped TiO_2 [Brydson1987, deGroot1993], the bonding between Ti 4s and the O 2p orbitals forms a mostly O 2p-derived valence band, as discussed before in Chap. 3.4.2. On the other hand, the conduction band is formed by antibonding Ti 3d, 4s, 4p and O 2p orbitals. In addition, the crystal field of the O atoms splits the Ti 3d band into t_{2g} (formed by d_{xy}, d_{xz} and d_{yz} orbitals) and e_g ($d_{x^2-y^2}$ and d_{z^2} orbitals). Since the Ti e_g orbitals point directly toward the 2p orbitals of the surrounding O atoms, the e_g band is very sensitive to the local environment. Moreover, the e_g peaks are expected to be broader than the t_{2g} ones due to a larger degree of hybridization of the Ti e_g orbitals with O ligands and associated broadening effects. Therefore, we attribute the two main structures in Fig. 19 to excitation from O 1s core level to t_{2g} and e_g bands. The peaks at higher energies are assigned to transitions into antibonding O 2p and Ti 4sp bands [Brydson1987, deGroot1993, Braun2010]. The dispersion of these bands is larger due to the larger size of the Ti 4s and 4p orbitals and correspondingly larger overlap. This region is much more sensitive to long-range order [SorianoSurfSci290] with respect to the lower energy part.

The NEXAFS spectra taken on the N-TiO_2 clusters and on the undoped TiO_2 film share a common trend in their lineshape. Nonetheless, the N-TiO_2 spectrum presents a clear broadening of all the features. This point provides an indication of a much more disordered structure for the cluster-assembled film [SorianoSurfSci290]. This is also confirmed by the higher energy part of the spectrum, where the features related to the O 2p – Ti 4sp bands are much broader with respect to that found for the PLD sample. Moreover, the main bump exhibits a shift of ~1.5 eV toward lower energies that could

be related to some changes in the ligand coordination [SorianoSurfSci290]. It is not clear, at this point, whether these changes can be directly ascribed to N-doping effects of the SCBD film.

In the low energy portion of the spectrum another difference can be appreciated looking at our least squares fitting results showed in Fig. 19. In fact, for the N-TiO_2 clusters, another component is found around 533 eV (black peak in Fig. 19) that is not present in the undoped TiO_2 film. This is consistent with a recent NEXAFS investigation of N-doped TiO_2 powder [Braun2010], in which the authors suggest that N-doping induces an extra peak in the same energy region which they tentatively ascribe to an $e_g^{\downarrow}$ state. This result would give a further confirmation that the N atoms are substitutionally embedded in the TiO_2 structure.

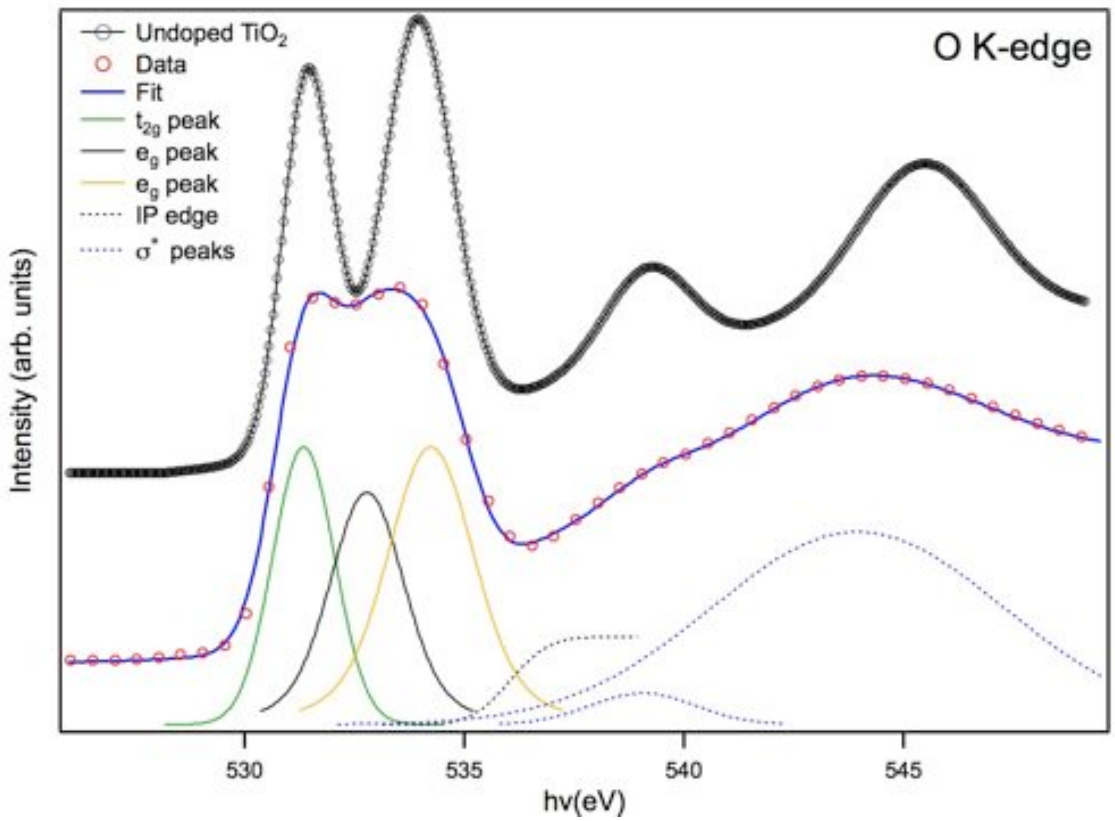

Figure 19 – O K-edge NEXAFS taken on N-doped TiO_2 nanoclusters (red circles) along with a reference spectrum taken on an undoped TiO_2 film.

With respect to what was found in the O K-edge absorption spectrum, the Ti L-edge spectra (Fig. 20) show a considerably more complex behavior. Such complexity arises, as pointed out by de Groot, from the strong Coulomb interactions between poorly screened Ti 3d electrons and the Ti 2p core holes [deGroot1990].

The Ti $L_{2,3}$ near-edge absorption spectra exhibit two main edges (labeled L_3 and L_2 in Fig. 20) separated by ~5.4 eV. These structures are due to transitions from the spin-orbit split Ti $2p_{3/2}$ and $2p_{1/2}$ core levels to the Ti $3d^*$ empty levels. For both the L_3 and L_2 edges, the crystal field splits the 3d bands into t_{2g} and e_g sub-bands [Braun2010, Mastelaro2006, Brydson1989]. The e_g states are further split into two sub-peaks (labeled D and E in Fig. 20) for both the L_3 and L_2 edges. Although, in the latter it is not well resolved due to lifetime-related broadening [Kucheyev2004]. This splitting of the e_g band into d_{z^2} and the $d_{x^2-y^2}$ orbitals, which are directed towards the ligand anions and therefore more sensitive to deviations from octahedral symmetry [Brydson1989], indicates the degree of distortion from the octahedral symmetry [deGrootPRB1990, Finkelstein2002].

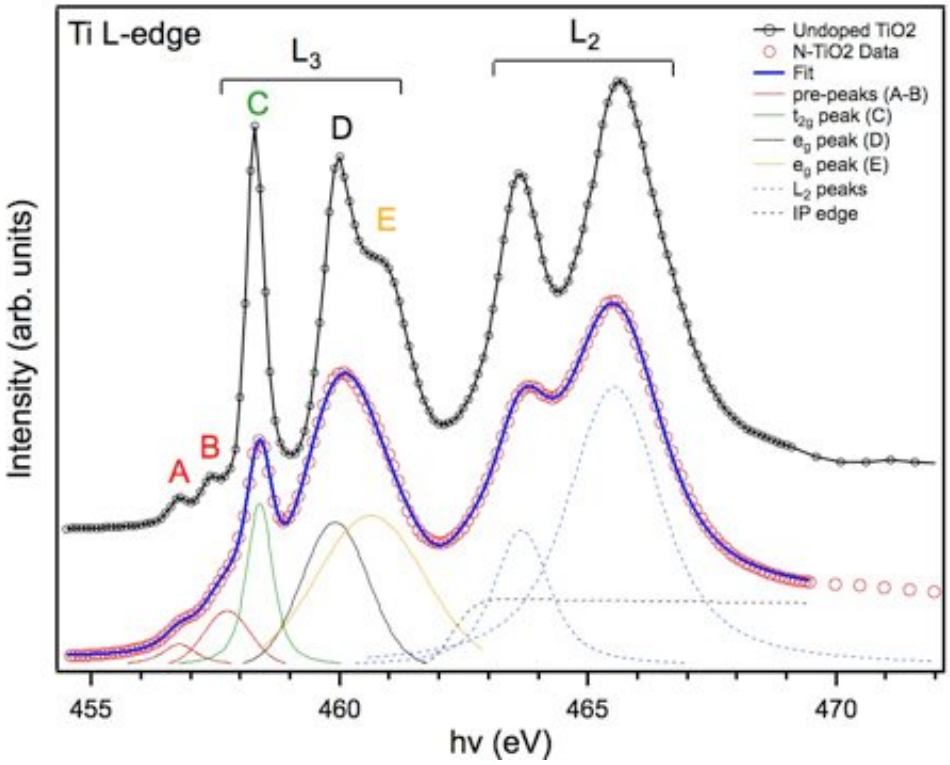

Figure 20 – Ti L-edge NEXAFS spectra taken on the same samples of Fig.19

Two other peaks, less intense but still well resolved, are present in the lowest energy region of the spectra (labeled A and B). The origin of these two contributions is still somewhat unclear: according to atomic multiplet calculations of de Groot et al. [de Groot1990], they are a result of the strong interaction between poorly screened 3d electrons and the Ti 2p core hole. However, more recent band structure calculations by Finkelstein at al. [Finkelstein2002] indicate that these peaks can also be attributed to sharp features in the one electron Ti 3d partial DOS, while the width and the intensity of these peaks are modified by correlation effects.

As found also for the O K-edge spectrum, the N-doped SCBD and the undoped PLD spectra share the same overall lineshape. Once again, the nanoclusters also exhibit the typical broadening due to the much more disordered structure, as discussed before. Besides that, the sharpest component's intensity is strongly reduced in the N-TiO_2

sample, and the e_g features D and E are not well resolved. These results are consistent with what was found by Caruso et al. for a similar undoped SCBD film [Caruso2008] and by Kucheyev for natively amorphous TiO_2 and titania aerogels [Kucheyev]. This suggests that the lack of long-range order in the cluster-assembled film is responsible for the major variations found in the NEXAFS spectra. Nonetheless, the intensity ratio between components C and (D-E) in our system is somewhat in between the undoped crystalline value and the results found in literature for amorphous systems. This may suggest that our SCBD film is not completely amorphous, but rather composed by nanometric-size crystals embedded in an amorphous matrix.

So far, only the O K-edge exhibited a possible feature (black e_g peak in Fig.19) related with the N doping. The Ti L-edge NEXAFS results suggest that the N atoms do not induce any major variation in the crystal structure. A better understanding of the N incorporation in the SCBD film can be gained by looking at the N K-edge absorption spectrum shown in Fig. 21.

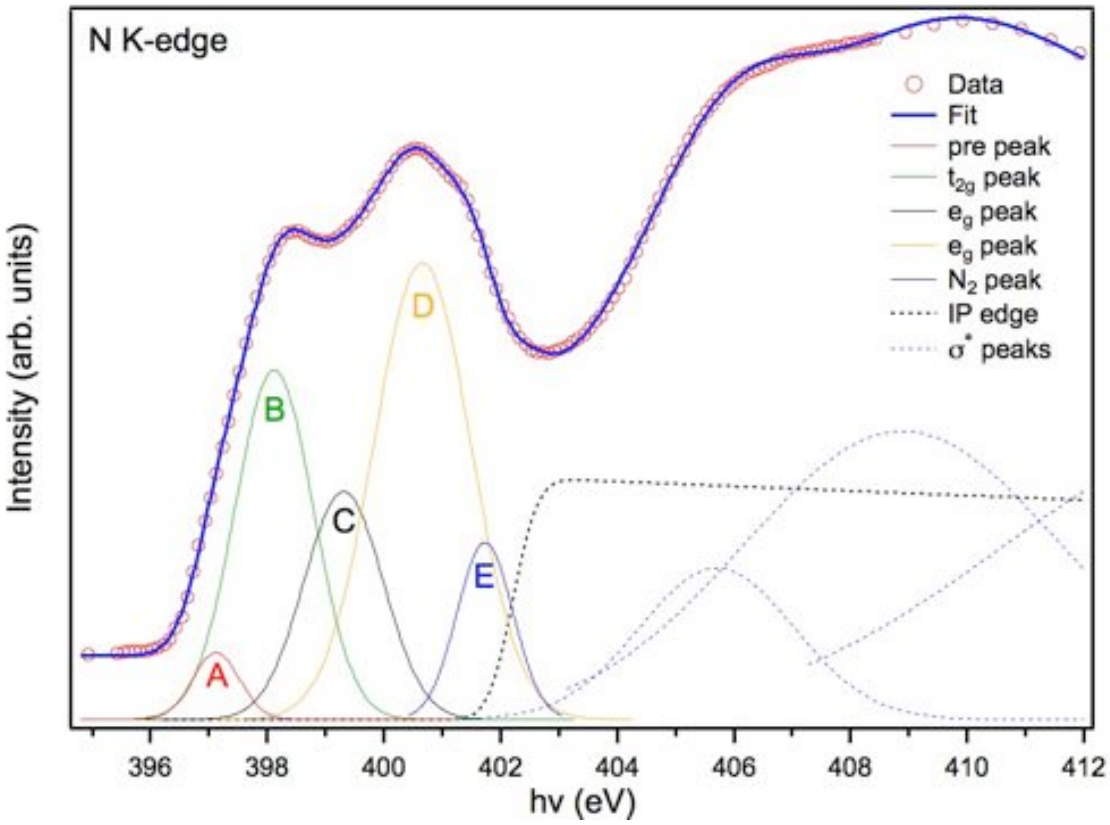

Figure 21 - N K-edge NEXAFS spectra for the N-doped TiO_2 nanoclusters

The spectrum exhibits two sharper peaks in the low-energy region, along with a much broader structure in the 405 - 412 eV range. The first two structures, centered around 398.5 and 400.5 eV, are attributed to transitions from the N 1s core level to N 2p – Ti 3d hybridized states [Kapoor1995, Esaka1999]. The Ti 3d sub-bands are also split into two separate peaks by the ligand field (as discussed before for O K-edge spectrum), giving rise to t_{2g} and e_g components (peaks labeled B and D in Fig. 20). The higher-energy peaks are attributed to transitions to N 2p – Ti 4sp sub-bands [SorianoSurfSc281, Chen2007]. The spectrum exhibits a line shape similar to that found for TiN samples [Chen2007, Esaka1999], and this suggests that the N atoms inside our SCBD film are essentially in a TiN-like environment (see Fig 22). Nonetheless, several differences can be pointed out comparing the two spectra. To better characterize these

differences a least squares fitting procedure was carried out, and the results are presented in Fig. 21. The main two peaks related to t_{2g} and e_g (labeled B and D) are found at 398.1 and 400.6 eV (Δ= 2.5 eV), and their intensity ratio appears to be reversed with respect to the TiN case. Considering the high sensitivity to the local environment of this portion of the spectrum, this difference can be related to the different crystal structure in TiO_2 (tetragonal) and TiN (cubic). This result appears to confirm that substitutional N atoms are diluted in the titania matrix.

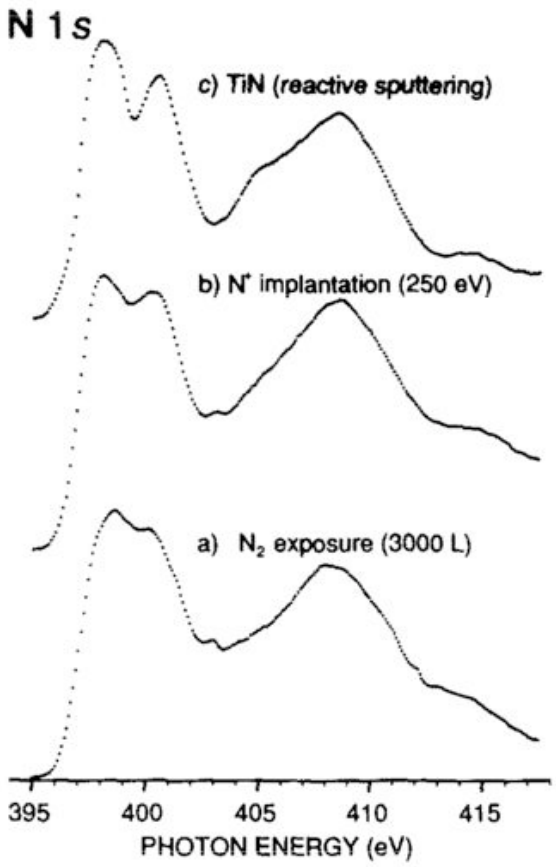

Figure 22 - NEXAFS spectra taken on N-exposed Ti (a), N-implanted Ti (b) and TiN sample (ref. SorianoSurfSci281)

Several additional peaks are found in this region: a pre-peak (labeled A) at 397.1 eV, a second peak (C) at 399.3 eV and a third (E) at 401.7 eV. The first two peaks have

never been reported in literature before for N-TiO2 or TiN. On the other hand, component E can be related to molecular N adsorbed on the surface or even trapped inside the porous structure of our SCBD film, in agreement with the literature [Esake1997, Esaka1999]. Notably, the presence of molecular N is also compatible with our previous N 1s core level spectrum (see Fig. 16), which exhibited a second component attributed to interstitial N. The origin of the pre-peak A is hard to explain only on the basis of these NEXAFS data. Still, it is worth mentioning that a recent hybrid DFT calculation of N-doped TiO_2 anatase crystals predicted the opening of N-related empty states at the bottom of the conduction band [TheoryData]. Likewise, the origin of component C is unclear. However, a comparison with the O K-edge discussed before (Fig. 19) could be helpful in evaluating the origin of this peak. In fact, it is evident that the two spectra share a very similar overall lineshape, possibly originating from a common hybridization with Ti 3d orbitals. During the previous discussion on the O K-edge spectrum, we also found an extra component between the main t_{2g} and e_g peaks that we attributed to the effect of N-doping, according to recent results found in literature [Braun2010]. Keeping in mind that e_g states are directed toward the anions, we tentatively ascribe this component in the N K-edge spectrum to another e_g state originating from Ti-N-O interactions. Clearly, more experimental and theoretical work is needed to fully characterize the origin of this additional component.

3.4.4 Conclusions

In this section we showed that SCBD can be adapted to grow nanostructured N-doped TiO_2 films. The dopants are efficiently injected inside the titania matrix in substitutional sites as confirmed by both the XPS and the NEXAFS results. The presence of nitrogen atoms appreciably modifies the states at the top of the VB, where a shift of the occupied states is observed.

References

[HandbookNanoscience2007] *Handbook of Nanoscience, Engineering and Technology*, 2nd ed.; Goddard III W.A., Brenner D.W., Lyshevski S.E. and Iafrate G.J. (editors), CRC press (2007).

[Nanofabrication2008] Cui Z., *Nanofabrication: principles, capabilities and limits,* Springer (2008).

[Wegner2006] Wegner K., Piseri P., Vahedi Tafreshi H. and Milani P., *J. Phys. D: Appl. Phys.* **39**, R439 (2006).

[Milani1999] Milani P. and Iannotta S., *Cluster Beam Synthesis of Nanostructured Materials*, Springer (1999).

[Barborini2008] Barborini E. et al., *J. Micromech. Microeng.* **18**, 055015 (2008).

[Barborini2005] Barborini E., Conti A.M., Kholmanov I., *Adv. Mat.* **17** 1842 (2005)

[Cassina2009] Cassina V. et al., *Phys. Rev. B* **79**, 115422 (2009).

[Barborini1999] Barborini et al., *Chem. Phys. Lett.* **300**, 633 (1999).

[Yamada1998] Yamada I. and Matsuo J., *Mater. Sci. Semicond. Proc.* **1**, 27 (1998)

[Henkes1995] *J. Vac. Sci. Technol. A* **13**, 2133 (1995).

[Apewebsite] http://www.elettra.trieste.it/experiments/beamlines/ape/index.html.

[Chambers1987] Chambers S.A., Hill D.M., Xu F. and Weaver J.H., *Phys. Rev. B*, **35** 634 (1987).

[Hou2003] Y.Q. Hou, D. -M. Zhuang, G. Zhang, M. Zhao and M.S. Wu, *App. Surf. Sci.* **218**, 97 (2003)

[Lesiak2006] B. Lesiak, J. Zemek and P. Jiricek, *App. Surf. Sci*. **252** 2741 (2006).

[Del Giudice1987] M. del Giudice, J.J. Joyce, M.W. Ruckman and J.H. Weaver, *Phys. Rev. B* **35** 6213 (1987)

[Larciprete2001] R. Larciprete, M. Danilov, A. Barinov, L. Casalis, L. Gregoratti, A. Goldoni and M. Kiskinova, *Surf. Sci.* **482,** 141 (2001)

[Arranz2005] A. Arranz and C. Palacio, *Surf. Sci*. **588**, 92 (2005).

[Butz1984] R. Butz, G.W. Rubloff, T.Y. Tan and P.S. Ho, *Phys. Rev B*, 30 5421 (1984).

[Caruso2008] Caruso T. et al., *J. Chem Phys* **128**, 094704 (2008).
[Kuri2002] Kuri et al., *J. Vac. Sci. Technol. A* **20**, 1997 (2002).
[Saha1992] Saha N. C., Tompkins H. G., *J. Appl. Phys*. **72**, 3072 (1992).
[Asahi] Asahi et al., *Science* **293**, 269 (2001).
[BatzillPRL2006] Batzill M., Morales E.H. and Diebold U.; *Phys. Rev. Lett.* **96**, 026103 (2006).
[Diebold2003] Diebold U., *Surf. Sci. Rep.* **48**, 53 (2003).
[CarusoAPL2004] Caruso T. et al., *Appl. Phys. Lett*. **84,** 3412 (2004).
[Barborini2003] Barborini E. et al., *Eur. Phys. J. D* **24**, 277 (2003).
[Nambu2006] Nambu A et al., *J. Chem Phys.* **125**, 094706 (2006).
[Caruso2007] Caruso T. et al., *Surf. Sci.* **601** 2688 (2007).
[SorianoSurfSci290] Soriano L. et al., *Surf. Sci.* **290**, 427 (1993).
[SorianoSurfSci281] Soriano et al., *Surf. Sci.* **281**, 120 (1993).
[Braun2010] Braun A. et al., *J. Phys. Chem. C* **114** 516 (2010).
[Brydson1989] Brydson R. et al., *J. Phys.: Condens. Matter* **1**, 797 (1989).
[Mastelaro2006] Mastelaro V.R. et al., *J. App. Phys.* **99** 044104 (2006).
[deGroot1990] de Groot F.M.F., Fuggle J.C., Thole B.T. and Sawatzky G.A., *Phys. Rev. B* **41** 928 (1990).
[Kucheyev2004] Kucheyev S.O. et al., *Physical Review B* **69** 245102 (2004).
[Chen2007] Chen H. et al., *J. Phys. Chem. C* **111**, 1366 (2007).
[Kapoor1995] Kapoor R. et al., *Catal. Lett.* **34**, 179 (1995).
[Esaka1999] Esaka F. et al., *Surf. Interface Anal.* **27**, 1098 (1999).
[theorydata] Zhu Z., private communication.

Introduction

As we discussed in the first chapter, the TiO_2 use as a photocatalyst is severely limited by its intrinsic band gap (>3 eV). In fact, TiO_2 can only harvest a small portion of the solar spectrum, namely the ultra-violet region. Since the first work of Fujishima and Honda [Fujishima1972], numerous attempts have been made to optimize the band gap of TiO_2 introducing different doping atoms. Regardless an overwhelming body of literature regarding the doping of TiO_2, the fundamental limitation is generally related to the extremely poor thermodynamic solubility of most of the dopant species, especially for p-type doping [DieboldReview, ChambersReview]. So far, most of the doping approaches used result in impurity atoms residing at undesirable interstitial sites, rather then substitutionally embedded in the TiO_2 matrix. As a result, the effectiveness of the band gap narrowing is often compromised. Moreover, interstitial dopants also provide numerous recombination centers that are responsible for the loss of photogenerated electron-hole pairs [Serpone2006, Nakano2007].

In a recent work, Zhu et al. proposed a noncompensated n-p co-doping approach in order to overcome these fundamental limitations [ZhuPRL2009]. First, they claimed that the Coulomb interaction between the n- and the p-type dopants with opposite charge states substantially enhances the solubility of the dopant pairs in substitutional sites. Second, the noncompensated nature of the dopants ensures the creation of impurity bands within the band gap region, effectively narrowing the band gap.

In their calculations they considered a bulk anatase TiO_2 codoped with n-p pairs: Cr-N, V-C, Cr-C an V-N. The first two couples give rise to net n-type and p-type doping, respectively; the latter two give compensated doping. The n-type dopants are substitutionally incorporated substituting a Ti atom, while the p-type ones substitute the neighboring O atoms. For each case, the n-type and p-type dopants are predicted to have a strong tendency to form a pair occupying neighboring lattice sites. The introduction of the different n-p couples induces major variations in the density of

states (Fig. 1). New electronic states are found in the intrinsic band gap, narrowing the gap's width to 1.6 eV and 0.9 in Cr-N and V-C codoped TiO_2, respectively.

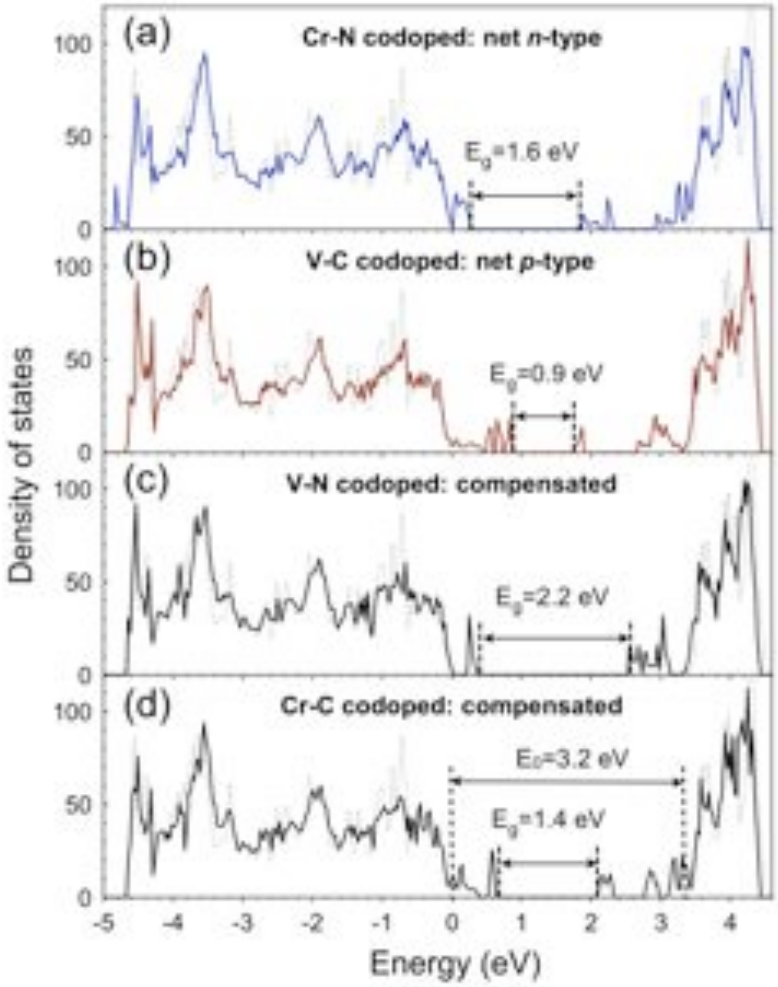

Figure 1 - Density of states (DOS) of anatase TiO_2 for different n-p doping pairs: (a) Cr-N resulting in net n-type doping: (b) V-C resulting in net p-type doping: (c) and (d) V-N and Cr-C resulting in compensated doping. The dashed lines indicate pure anatase TiO_2 DOS [ZhuPRL2009].

In search for optimal growth conditions, Zhu et al. also addressed the formation energies of codoped systems with different dopants' configurations (interstitial and substitutional). Their results predict that is energetically favorable to dope both Cr and

N in substitutional sites at O-rich conditions, while this is unfavorable for the V-C pair (Fig. 2a and b). A third aspect the authors examined is the kinetic solubility of the two dopants. Notably, an interstitial Cr or N atom alone has to overcome an energy barrier of 2.0 and 2.3 eV respectively to become a substitutional dopant. Moreover, nitrogen atoms already in substitutional sites only need to overcome a barrier of ~0.5 eV to go back to interstitial sites, indicating that N strongly prefers the latter configuration.

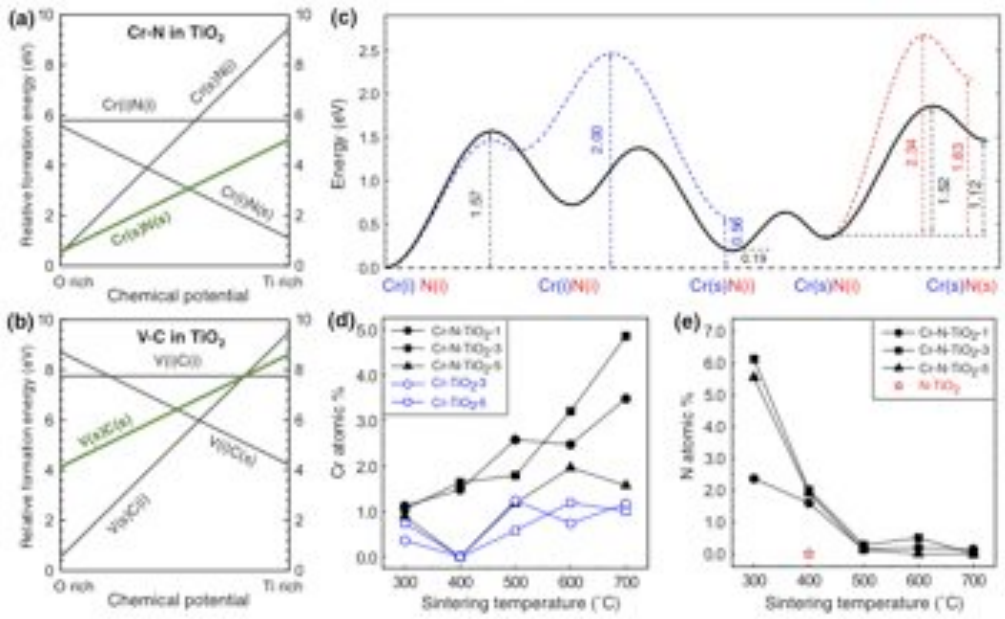

Figure 2 – (a) and (b): calculated relative formation energy for all the possible combinations of interstitial and substitutional configurations of Cr-N and V-C in anatase TiO_2 as a function of the chemical potential of Ti and O. (c): calculated kinetic barriers for a single Cr (blue), a single N (red) and a Cr-N pair (black solid line) going from interstitial to substitutional sites in anatase TiO_2. (d) and (e) XPS measurements of the Cr and N concentrations in anatase TiO_2 nanocrystals as a function of the annealing temperature (the numbers in the legend designate the nominal at.% of the Cr precursor) [ZhuPRL2009].

These results seem also to explain why it has been exceptionally difficult to dope high concentration of substitutional N into TiO_2 [DiValentin2007]. In contrast, for the Cr-N pair, the interstitial Cr and N atoms can reach simultaneous substitutional sites overcoming a significantly lower overall energy barrier with respect to the single doping

case (Fig. 3). Finally, they also calculated the variation in the final state energy for Cr-N pair, and they found that is 0.71 eV lower than that of N dopant alone. Thus, they concluded that both the kinetic and thermodynamic solubilities of the dopants are substantially enhanced by noncompensated codoping.

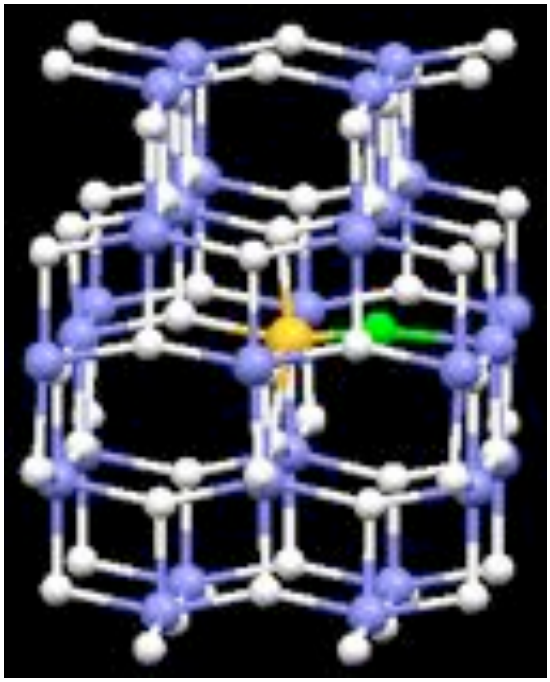

Figure 3 – Ball-and-stick model of the Cr-N-TiO_2 structure as proposed by Zhu et al [ZhuPRL2009]. The substitutional Cr and N atoms are present at the yellow and green sites, respectively. The Ti and the O atoms in the TiO_2 matrix are present at the blue and white sites.

Along with theoretical calculations, also some experimental data is presented supporting the predictions for Cr-N codoped TiO_2. The authors used a wet chemical technique to prepare pure, doped and codoped TiO_2 nanocrystals. The amount of Cr and N found in the particles was estimated by XPS (see Fig. 2d and e). The results confirm that the codoping approach is more effective in retaining N (still present up to 400°C), while in the single doped case is lost at a lower temperature (<300 °C). Nonetheless, beyond the 400 °C limit, no nitrogen is found in the film (or just a small amount at 600 °C, as evident in Fig. 2e). Moreover, is not clear whether the authors took into account just the XPS signal coming from the desirable substitutional N or both the substitutional and the interstitial one (see Chap. 3.4). This aspect could have lead to a possible

overestimation the N concentration in all the samples. In addition, the wet chemical technique used to deposit the Cr-N-TiO_2 nanocrystals does not allow for a precise control of the doping concentrations, making it difficult to verify whether the N and the Cr are embedded in pairs (i.e. 1:1 ratio) as predicted.

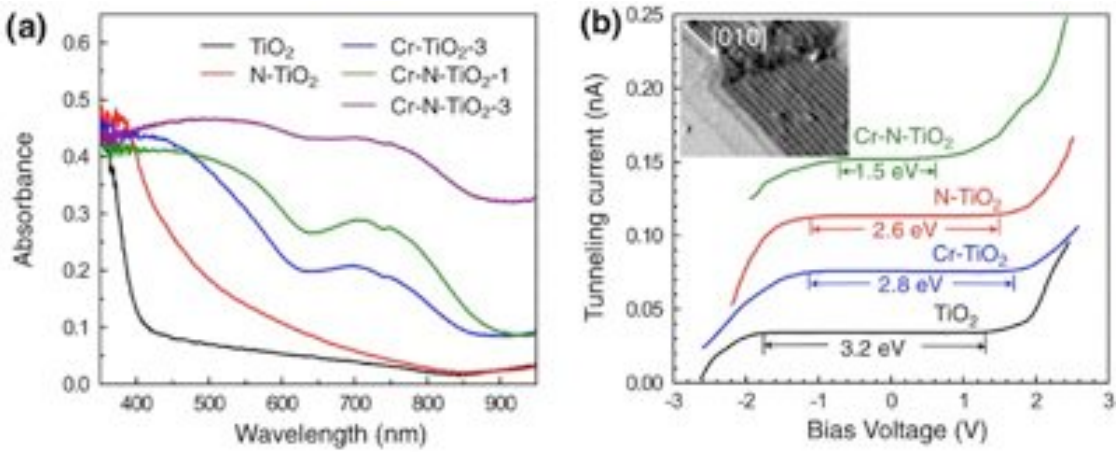

Figure 4 - Absorbance and STS measurements conducted on undoped, N- and Cr- single doped and Cr-N codoped TiO_2 samples

The optical absorbance and the Scanning Tunneling Spectroscopy (STS) results both confirm a consistent band gap narrowing in the codoped sample, with respect to the single doped ones (Fig. 3). Still, it remains unclear whether this effect is due to a overall shift of the VB and/or CB, or whether it is due to the existence of impurity bands similar to those predicted by the calculations. Finally, there is no solid evidence that both N and Cr are present in substitutional lattice sites.

As a final remark, it is clear that the work presented by Zhu et al. could have a very broad impact on the photovoltaic applications of TiO_2. Nonetheless, more work is still needed to prove the validity of their results.

In the following chapter, we will investigate the possibility to use SCBD to grow Cr-N doped TiO_2 films in UHV conditions. We already discussed the extremely high reactivity of the cluster-assembled films in Chap. 3, also proving that dopants can be easily

introduced inside the TiO_2 matrix. Hence, SCBD appears to be potentially very effective in growing films with a higher concentration of dopants in a much more controlled system (UHV) compared to standard wet chemical techniques.
The as-deposited samples will be characterized both in-situ and ex-situ by means of microscopy (AFM, XRD) and spectroscopy techniques (XPS, XAS, RESPES), discussing both their morphology and their electronic structure compared to the undoped and the N-doped case.

4.1 Deposition of Cr-N-TiO_2 nanoclusters

4.1.1 Experimental

Nanostructured Cr-N-doped TiO_2 films were deposited using the same supersonic cluster beam deposition apparatus described in details in Chap. 3.2. Instead of the standard titanium rod, we used a new, high purity (+99.99%) Ti-Cr rod. The Cr-Ti atomic ratio in the rod was 5:95, as estimated by the supplier. As expected, no operational parameter variations were needed to operate the source with the new rod. This is consistent with many works in literature [ThetisWebsite, Cassina2009], confirming that the PMCS can efficiently deposit almost any transition metal [ThetisWebsite]. Nitrogen dopants were introduced in the source's chamber as both air residual traces and impurities diluted into the He flow, following the same procedure successfully used to deposit N-TiO_2 nanoclusters (see Chap. 3).
Cr-N-TiO_x films were grown in UHV conditions at RT on different substrates both Si(001) and $LaAlO_3$ single crystals, in order to match the different requirements of the various techniques used for the characterization. Before the deposition, both the substrates were cleaned by means of standard procedures described in details in Chap. 3.4.1. The films' chemical composition was then investigated *in situ* right after the deposition using XPS. The samples were then left in oxidizing atmosphere, as done for

TiO_2 and N-TiO_2 samples (see Chap. 3.4.1). Again, the complete oxidation was checked using XPS. The resulting films were found to be composed of doped TiO_x with x ~2, indicating that the oxidation was successfully completed.

The films were then analyzed *ex situ* using X-ray Photoemission Spectroscopy (XPS), Resonant X-ray Photoemission Spectroscopy (RESPES) and Near-Edge X-ray Absorption Fine Structure spectroscopy (NEXAFS) at the Spectro-microscopy lab at the University of Tennessee, Knoxville TN (USA) and at the APE beamline at the elettra synchrotron radiation facility in Trieste (Italy). After the insertion in the experimental chamber through a fast entry-lock, the samples were degassed for ~1h at 100 °C. During the experiments the pressure in the chamber was kept below 1 x 10^{-10} mbar. XPS measurements were conducted using an Omicron multiscan system equipped with monochromatized Al K-alfa X-ray source (hv= 1486.7 eV). The spectra were acquired in normal emission using an Omicron multichannel setector.

At the APE beamline, the data were acquired using an Omicron photoelectron analyzer, the photon energies used ranged from 390 eV up to 1486 eV, as set from the beamline monochromator, and were calibrated using an Au plate as a reference.

The NEXAFS spectra were acquired in Total Electron Yield (TEY) in order to maxime the bulk-sensitivity of the measurements. [Apewebsite]

4.1.2 Chemical analysis: photoemission results

The XPS analysis of the deposited films confirms that SCBD is a powerful tool to grow also Cr-N codoped samples. Strong evidences of the presence of both nitrogen and chromium are found, as indicated in Fig. 4. As discussed in Chap. 3.4.2, also some carbon contaminations are found on the sample due to the exposition to air.

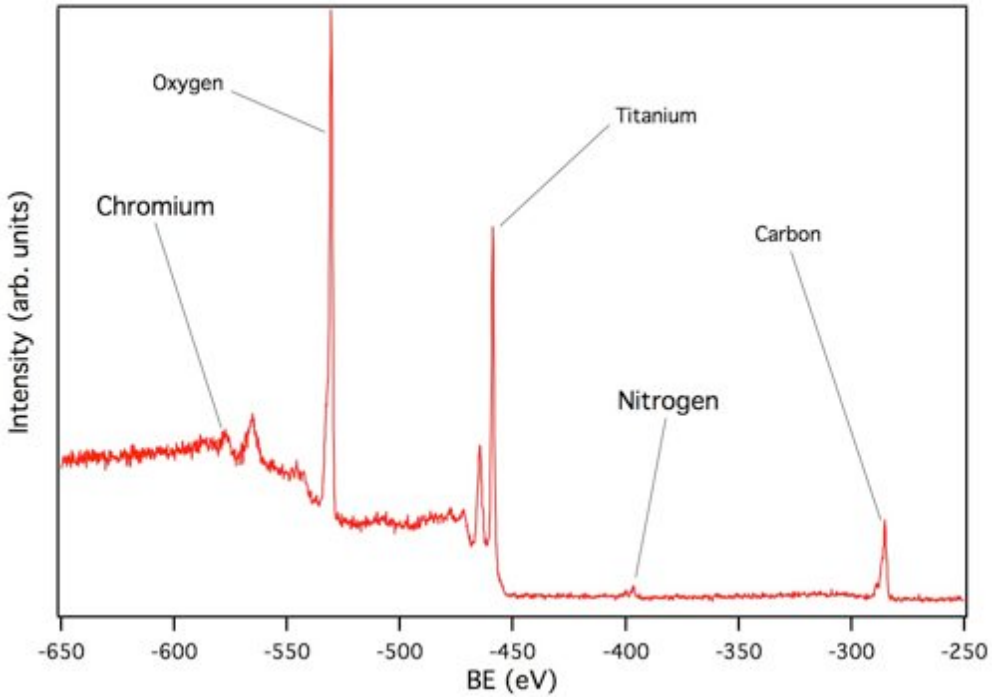

Figure 5 - XPS broad scan taken on the Cr-N-doped TiO2 nanoclusters

The N 1s spectrum shown in Fig. 5 resembles the one measured on the N-TiO_2 film, presenting two distinct components ascribed to interstitial and substitutional N incorporated in the nanostructured film. The **i** component at 399.8 eV (FWHM= 1.7 eV) exhibits a more pronounced intensity compared to the N-TiO_2 sample, indicating that more interstitial nitrogen is present in the film. This can be related to both the presence of Cr in the film and to a slight variation in the Cr-N-doped film structure affecting its porosity and reactivity. On the other hand, the most desirable **s** component found at 396.4 eV BE (FWHM= 1.0 eV) does not show any appreciable intensity variation with respect to what measured for N-only doped SCBD film.

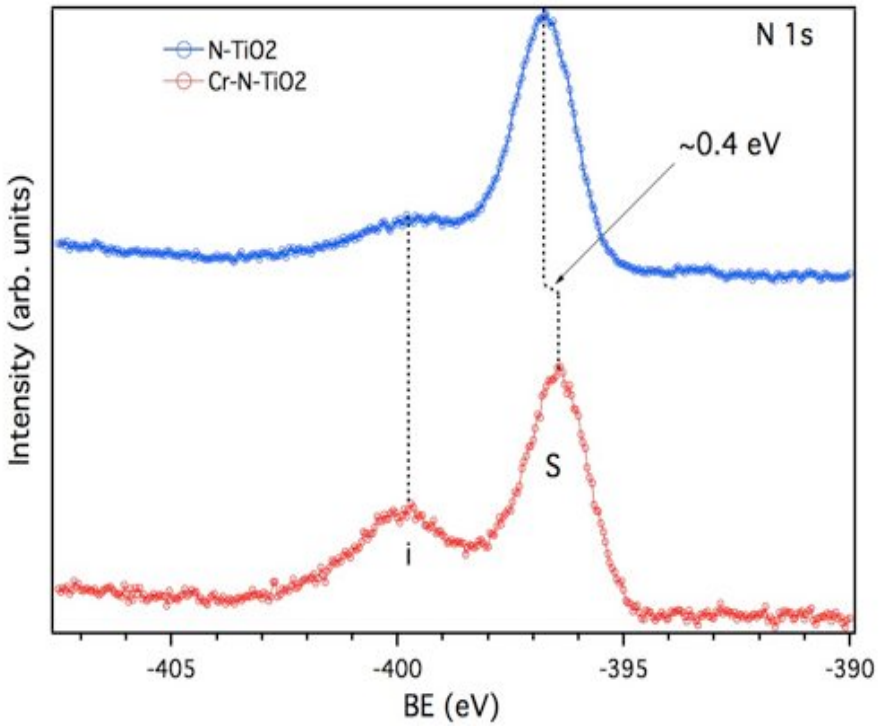

Figure 6 - N 1s core level spectra taken on the N-TiO2 (O) and on the Cr-N-TiO2 (O) samples.

Notably, this component exhibits a shift toward lower BE of ~ 0.4 eV. This can be explained in terms of a larger charge transfer to the N dopants in a Cr-Ti environment, with respect to what found in a Ti-only one [Bertoti2002]. As suggested by Bertoti et al., the energy position of this component can also give a hint of what is the N/Cr ratio in the sample. In fact, for chromium nitrides, the N 1s peak is found to shift towards higher BE in Cr-rich compounds (up to 397.5 eV BE), while it is centered at ~396.5 eV for N-rich compounds. Thus, our results suggest that the N atoms are present in a CrN_x-like environment with $x \geq 1$. This result does not help to definitely establish whether the theoretical picture given by Zhu et al. is a good description of the Cr-N doping mechanism. In fact, they predicted the formation of Cr-N pairs (thus a Cr:N ratio of 1) reaching substitutional sites simultaneously, overcoming a significantly lower energy barrier compared to the single doping case (see Introduction and Fig. 3).

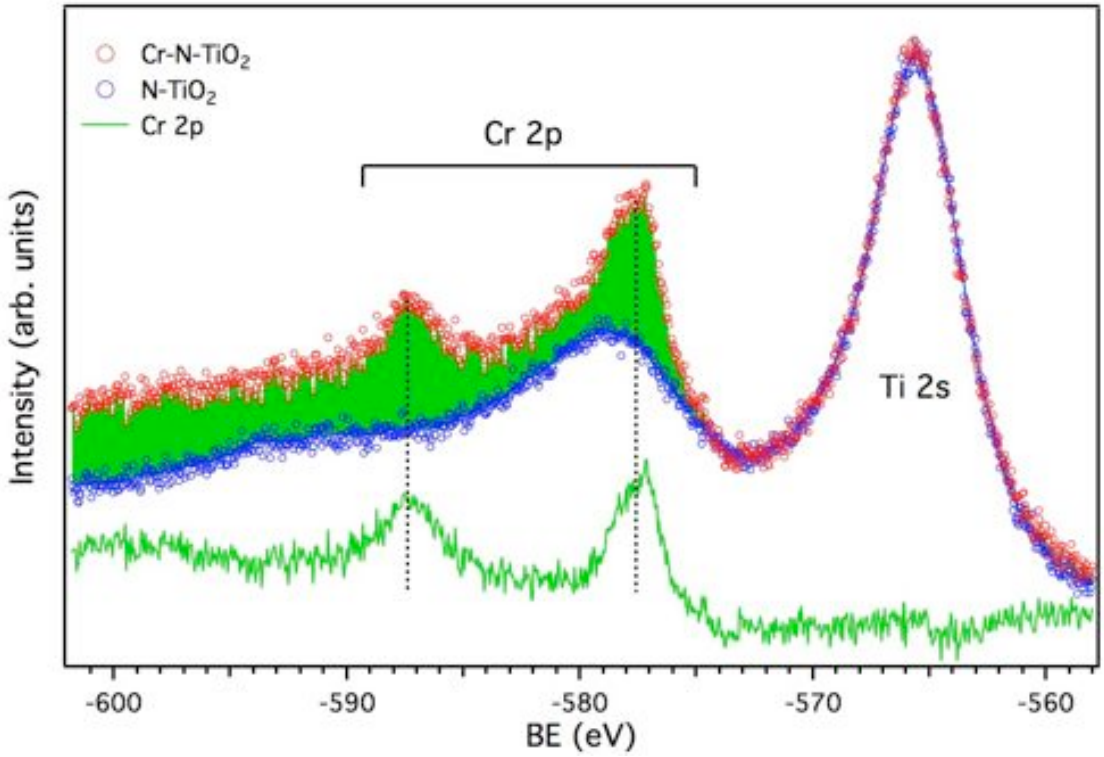

Figure 7 - Cr 2p and Ti 2s XPS results for Cr-N-TiO_2 nanoclusters (red markers) and N-TiO_2 nanoclusters (blue)

In order to the study the SCBD efficacy in depositing co-doped titania films, we collected the Cr 2p core level spectrum. The results are plotted in Fig. 7 along with the same region measured on the N-TiO_2 sample. The spectrum is complicated by the contemporary presence of the Ti 2s peak and its related plasmon loss (~566 eV and ~579 eV BE). Nonetheless, the codoped sample clearly exhibits two additional features around 577 eV and 587 eV BE attributed to photoelectrons originating from Cr $2p_{3/2}$ and $2p_{1/2}$ levels, respectively [Unveren2004, Slebarski2001]. Using the spectrum obtained on the N-doped sample, we subtracted the contribution originating from both the Ti 2s and its plasmon loss from the Cr-N doped spectrum. This leaves us with only the components originating from the Cr 2p photoemission (green spectrum in Fig. 7). The BEs measured for the $2p_{3/2}$ and $2p_{1/2}$ peaks (577.3 and 587.3 eV, respectively) are close

to the values found in literature for CrO_x (577.1 eV) [Mischie1988], rather than what found for Cr-N bonds (574.5 eV BE) [Bertoti2002]. This result suggests that the Cr is primarily involved in Cr-O bonds, but a Cr-N-O interaction cannot be ruled out, because of the limited resolution of our XPS measurements along with the low concentration of the dopants.

These first results confirm that the chromium is successfully introduced in the film, but it does not help to clarify whether the dopants are present in substitutional or interstitial sites. In fact, the low concentration of Cr dopants and the underlying Ti-related peaks, hamper an accurate evaluation of the Cr peak lineshape.

In order to possibly circumvent this issue, the Cr 3s core level peak was also acquired (Fig. 8). This particular peak possesses a very low cross-section, especially when investigated using a photon energy of 1486.7 eV [Yeh1985]. Nonetheless, it is particularly interesting due to possible splits due to final-state effects [Pollini2001, McFeely1972, Shirley1975].

It is well known that in any atomic system with unpaired valence electrons, the exchange interaction affects core electron with spin up and spin down differently. According to atomic theory [VanVleck1934], this causes a splitting in the core levels that is proportional to the total spin *S* of the 3d valence shell. The intensity ratio between the split peaks should also be given by *S/(S+1)* [Fadley1969]. Nonetheless, the description of the experimental results on different transition metals (TM) is sometimes controversial. Late TM compounds are generally well described in this picture. In contrast, early TM compounds do not show a clear correlation of the exchange splitting with the actual d occupation or the magnetic moment [ZimmermannJphyscondmatt1998, VaAcker1988]. On the other hand, the splitting does show a tendency to increase with the formal d occupation [Zimmermann1998]. Accordingly, for instance, no exchange splitting is observed in d^0 compounds like TiO_2 [Zimmermann1998].

In our case, the presence of Cr impurities diluted in a TiO_2 matrix, should give rise to a splitting of the Cr 3s core level peak that reflects the valence configuration of the atoms

inside the material. This can give us an important insight on the Cr dopants electronic configuration, allowing an estimation of its oxidation state.

Cr-doped TiO_2 has been extensively characterized in literature, both theoretically and experimentally [ZhuPRL2009, Osterwalder2005, Nolan2009, Kaspar2005, Gracia2004]. When chromium impurities are successfully incorporated in substitutional sites of the TiO_2 lattice, their oxidation state is expected to be 3+ (d^3 configuration) [Gracia2004, ZhuPRL2009]. Hence, the corresponding exchange interaction splitting is expected to be ~ 4.2 eV, as commonly found in several Cr^{3+} compounds [Tsurkan2000].

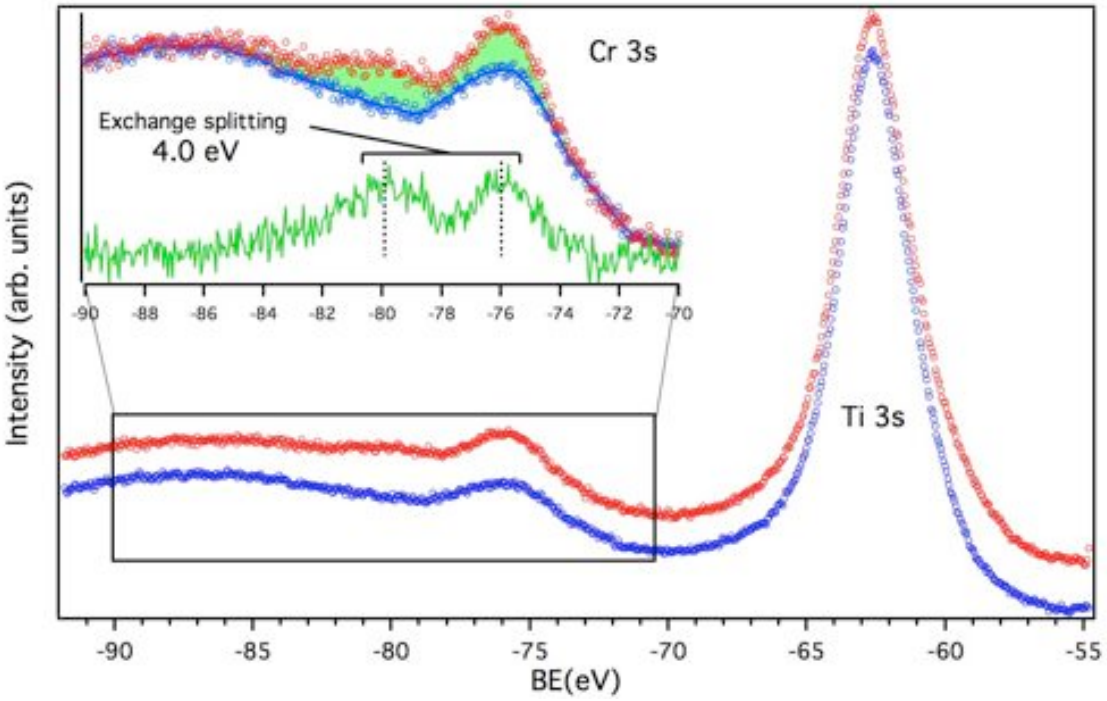

Figure 8 - Cr 3s XPS results for Cr-N-TiO_2 nanoclusters (red markers) and N-TiO_2 nanoclusters (blue)

Our results are illustrated in Fig. 8, where both the spectra taken on N-TiO_2 and Cr-N-TiO_2 are presented (blue and red spectra, respectively). These spectra are dominated by a strong component attributed to Ti 3s core level emission centered at 62.5 eV BE. Unfortunately, the Ti plasmon loss ~ 13 eV away from the main peak is in the same BE

region where the Cr 3s core level peak is expected (see the bump around 76 eV BE). This spurious contribution to the Cr emission has been accounted for subtracting the N-TiO_2 spectrum (slightly smoothed) from the Cr-N-TiO_2 data after normalizing the spectra to the Ti 3s peak. The result of this procedure is displayed in the inset of Fig. 8 (green spectrum). After the background subtraction, two distinct Cr 3s components are found at 76 and 80 eV BE (Δ= 4.0 eV). The separation between the two indicates the presence of Cr^{3+} ions diluted in the titania film, confirming that the Cr atoms are replacing Ti ones in the TiO_2 lattice.

Finally, we estimated the atomic concentration of Cr and N impurities present in the film to be 2.15% and 4.0%, respectively. This result finally proves that the doping process follows two separate channels for the two dopants, leading to different concentrations in the film. The Cr-N pairs formation cannot be completely ruled out, but the significantly higher N concentration indicates that the single incorporation of N can take place in SCBD films even without the contemporary presence of a Cr atom to form a Cr-N doping pair.

The Ti 2p spectrum (Fig. 9) is similar but not identical to the one taken on the N-only doped sample. The main peak (Ti $2p_{3/2}$) is now located at 459 eV, ~0.2 eV away from the same peak measured on the N-TiO_2 film. Moreover, in the latter case we also found an evident shoulder on the lower-BE side (457.55 eV BE) of the peak, attributed to Ti^{3+} related with both O-vacancies and N-Ti-O bonds. In the Cr-N-doped sample, a weak and very broad component centered around 457.2 eV BE is found instead. Several different aspect of the film can give rise to this feature, such as oxygen vacancies, TiN-like bonds and Ti-Cr interactions inside the clusters. Nonetheless, the overall Ti 2p spectrum lineshape and the very weak intensity of the low-BE component are consistent with a cluster-assembled film possessing a near-stoichiometric composition.

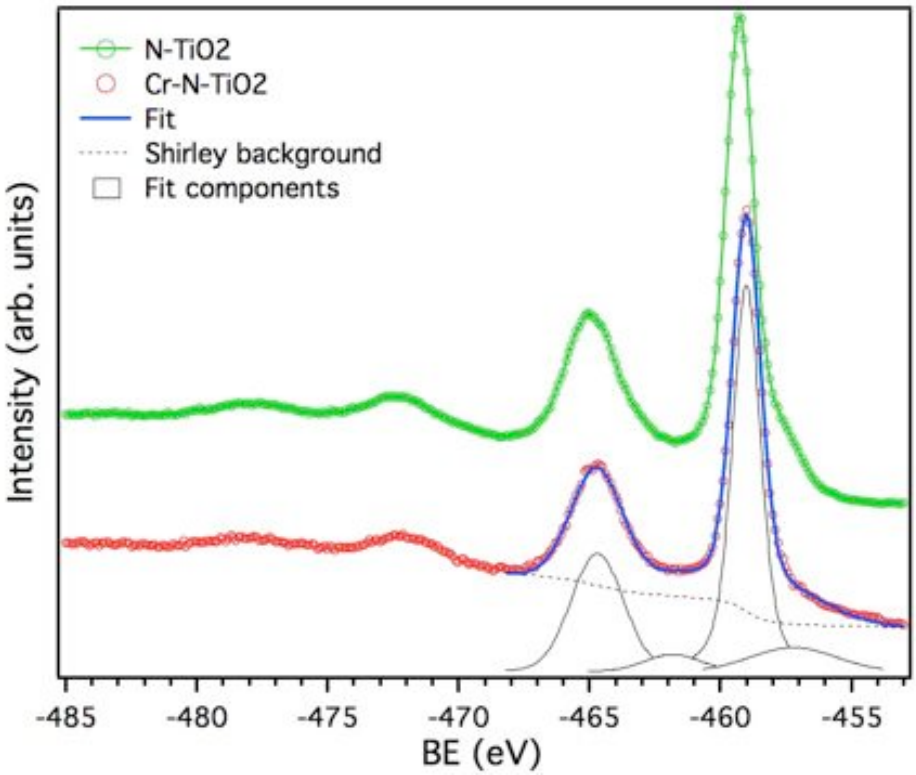

Figure 9 - Ti 2p core level spectra taken on Cr-N- and N-doped SCBD films (red and green markers, respectively), along with the results of a least squares fitting procedure (blue solid line). Also the fit components are reported (black lines).

4.1.3 Empty states in the CB: X-ray Absorption Spectroscopy

The same characterization presented in Chap. 3.4.3 for the SCBD N-doped TiO_2 sample, was carried out for the Cr-N codoped nanoclusters sample to investigate any possible change in chemical composition and/or orbital local symmetry.

The Ti L-edge and O K-edge absorption spectra measured on the cluster-assembled Cr-N-TiO_2 film resemble what measured on the analogous N-only doped film, as evident from Fig. 10 and 11, where the two data sets are compared. Both Ti and O edges are virtually unchanged, presenting the same spectral features with no noticeable variations in the peak positions or in the spectral intensities.

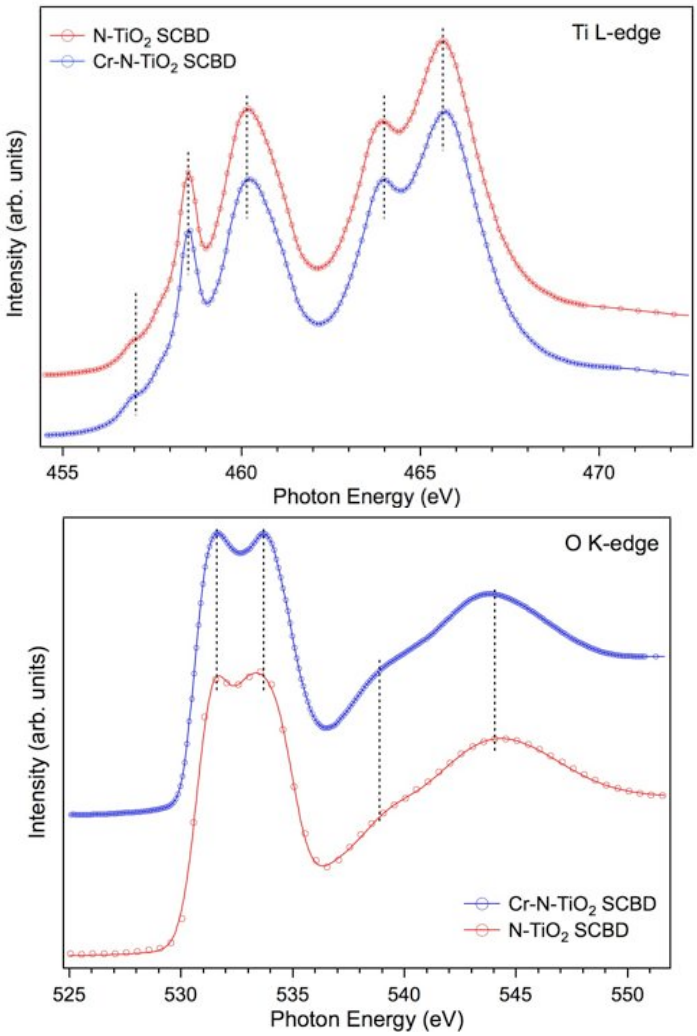

Figure 10 – Ti L-edge and O K-edge absorption spectra acquired on Cr-N- and N-only doped SCBD samples (blue and red spectra, respectively).

As we discussed in details in Chap. 3, NEXAFS is extremely sensitive to the local symmetry and to the chemical environment surrounding the atom considered. Therefore, a constant lineshape implies that the overall structure of the titania nanoclusters is not affected by the type (and the number) of the dopants introduced in the system, further confirming the results obtained for the SCBD TiO_2 on silicon described in Chap. 3.2.

Considering the low concentration of N and Cr present in our samples, N K-edge and Cr L-edge absorption spectra should give more information about the coordination inside the system and the chemical environment surrounding these ions. The NEXAFS data taken at these two absorption edges are presented in Fig. 11 and 12.

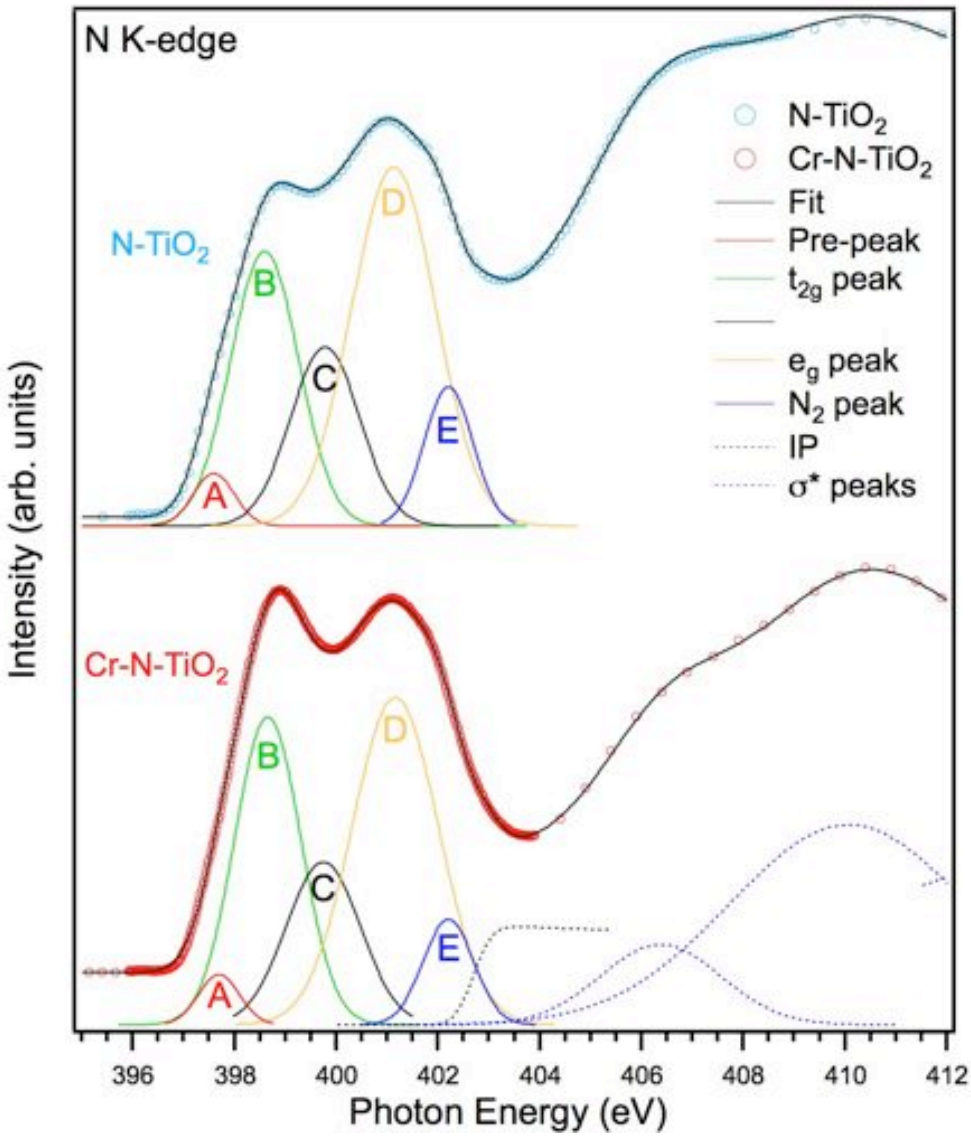

Figure 11 – N K-edge XAS spectra taken on Cr-N-TiO_2 SCBD sample (red spectrum) along with the same spectrum taken on the N-only doped TiO_2 SCBD film.

The N K-edge of the Cr-N doped sample presents two sharp structures in the low-energy region (398-402 eV) with a much broader structure in the 405-412 eV range. The first two peaks, centered around 398.5 and 401 eV, are due to N 2p – Ti 3d states. These states are split into two separate contributions by the ligand field, originating the t_{2g} and e_g components (peaks B and D in Fig.11), as discussed in details in Chap. 3.3.3. The spectrum exhibits a lineshape that follows the trend set by the N-only doped SCBD film (light blue spectrum in Fig. 11), with the same broadening related with the nanostructured character of the SCBD samples. In Fig. 11 are also presented the results of a least squares fitting procedure carried out on the NEXAFS spectrum. Our results show that the same components used to fit the N-TiO_2 data can successfully fit also the Cr-N codoped data, possibly suggesting that the N atoms are not affected by the presence of the Cr dopants. Nonetheless, an important difference between the two spectra is evident: the e_g - t_{2g} intensity ratio (peaks B and D in Fig. 11) is now much more balanced, while in the N-TiO_2 film the e_g peak is clearly more intense. This variation has an interesting effect on the overall lineshape of the N K-edge absorption spectrum that can be appreciated looking at Fig. 12. Here the N K-edge and the O K-edge XAS results obtained for the same SCBD Cr-N codoped sample are compared. The O-edge spectrum has been shifted in order to align the first peak of the spectra at 399 eV.

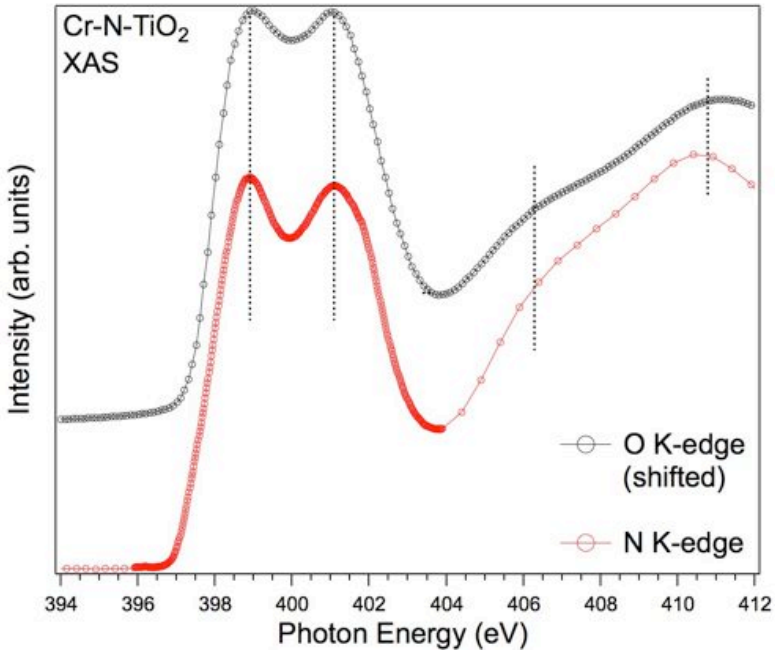

Figure 12-XAS spectra taken on the Cr-N-TiO_2 sample at the N and O absorption edge. The O-edge spectrum has been aligned to the first peak of the N-edge spectrum (399 eV).

The N and O spectra appear almost identical, presenting the same ligand-field splitting of 2.3 eV between the e_g and t_{2g} features. Also the σ^* part (i.e. beyond 404 eV) appears to be very similar, with two main structures centered around 406.5 and 411.5 eV. The common lineshape shared by these two spectra suggests that O and N species are sharing essentially the same coordination to the cations present in the film (Ti and Cr atoms). This is also confirmed by the similarity between the N K-edge NEXAFS data presented here and what found in literature for TiN samples (see Fig.22 in Chap. 3) [SorianoSurfSci281]. These results are a strong confirmation that N is efficiently injected in substitutional sites inside the SCBD film and suggest that N and O states are significantly hybridized.

On the other hand, no clear signs of a Cr-N interaction can be found in the N K-edge NEXAFS data. This might indicate that no extended Cr-N pairs formation is taking place in our SCBD codoped films, but it can also be due to the low concentration of N and Cr inside the film. Therefore, our efforts to understand the mechanism driving the Cr-N

incorporation inside the SCBD titania film involved a NEXAFS characterization of the Cr L-edge, presented in Fig. 13.

Cr L-edge absorption spectroscopy provides valuable information on the electronic structure of the metal ion, being very sensitive to the different species of Cr [Kendelewicz1999]. However, for transition metal compounds with unfilled d states, a simple one-electron-like description of the absorption process is not adequate in understanding the experimental results [Theil1999]. In particular, the metal L-edges that correspond to excitation of a 2p electron to empty 3d states are best described by atomic-like multiplet transitions for the appropriate site symmetry determined by the ligands, as explained in details by deGroot et al. [deGroot1989]. Those results demonstrate the extreme sensitivity of such NEXAFS spectra to oxidation state of the cation and to the geometry of the nearest-neighbor coordination shell. The atomic nature of these transitions allows an easy interpretation of the data taken on complex systems by a direct comparison with suitable standards of known charge state [Kendelewicz1999, Dedkov2005].

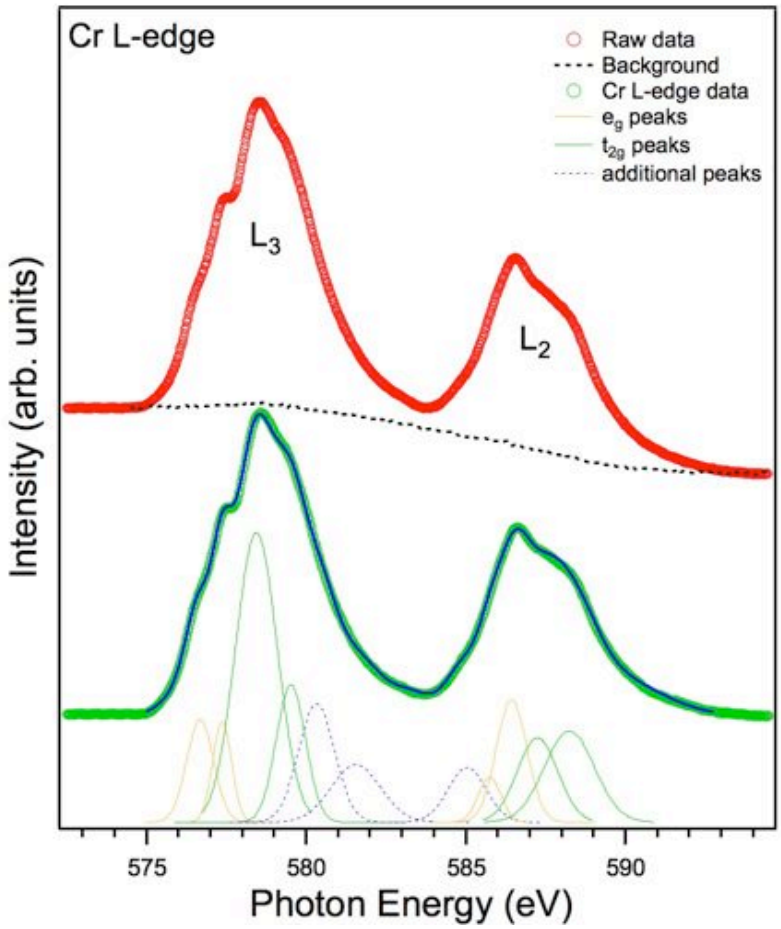

Figure 13– Cr L-edge X-ray absorption spectrum before (red spectrum) and after (green) background subtraction

The Cr L-edge absorption spectrum presents two distinct structures centered around 578.5 eV and 587.5 eV originating from the spin-orbit split initial states ($2p_{3/2}$ and $2p_{1/2}$, respectively). The separation between the L_3 and L_2 edges is comparable to the width found in the corresponding core level photoemission spectrum (see Fig. 7). Each structure presents a fine structure originating from the multiplet effects related with the extra electron added to the Cr 3d empty states [Arnold2009]. Our analysis involves a least squares fitting procedure based on the superposition of several Gaussian components over a background (dotted line in fig.13) obtained measuring the same

spectral region on the SCBD N-only doped TiO_2 sample discussed in Chap. 3. At least four strong components can be isolated in both L_3 and L_2 absorption edges, these are ascribed to e_g and t_{2g} states [Theil1999, deGroot1990]. Additional peaks are also found in the 580-585 eV region, possessing lower intensity and a broader width. These contributions are ascribed to other not resolved multiplet features, as frequently found in literature (see Fig. 14) [Theil1999, Dedkov2005, Kendelewicz1999, Bhobe2010].

As explained before, a direct comparison with some results obtained on different compounds is very useful in understanding the oxidation state of Cr inside our SCBD film. In fact, various Cr^{3+} compounds exhibit the same lineshape found in our analysis, as evident comparing Fig. 13 and Fig. 14, where some Cr L-edge absorption spectra taken on different chromium compounds are presented [Theil1999, Dedkov2005, Kendelewicz1999]. As discussed in details by Theil et al., the local Cr^{3+} site symmetry is slightly distorted octahedral. The ground state does not change with a small distortion of the ligand field symmetry but remains t_{2g} [ChenPhysScripta1990]. Thus, the absorption spectrum is only slightly dependent on distortion [Theil1999]. This is a fundamental issue in our case, since implies that the Cr L-edge NEXAFS lineshape, in a first approximation, can be taken as representative of the Cr oxidation state, without a strong influence of the SCBD porous and distorted structure.

This is another strong confirmation that chromium atoms are successfully injected in substitutional sites inside the TiO_2 nanoclusters.

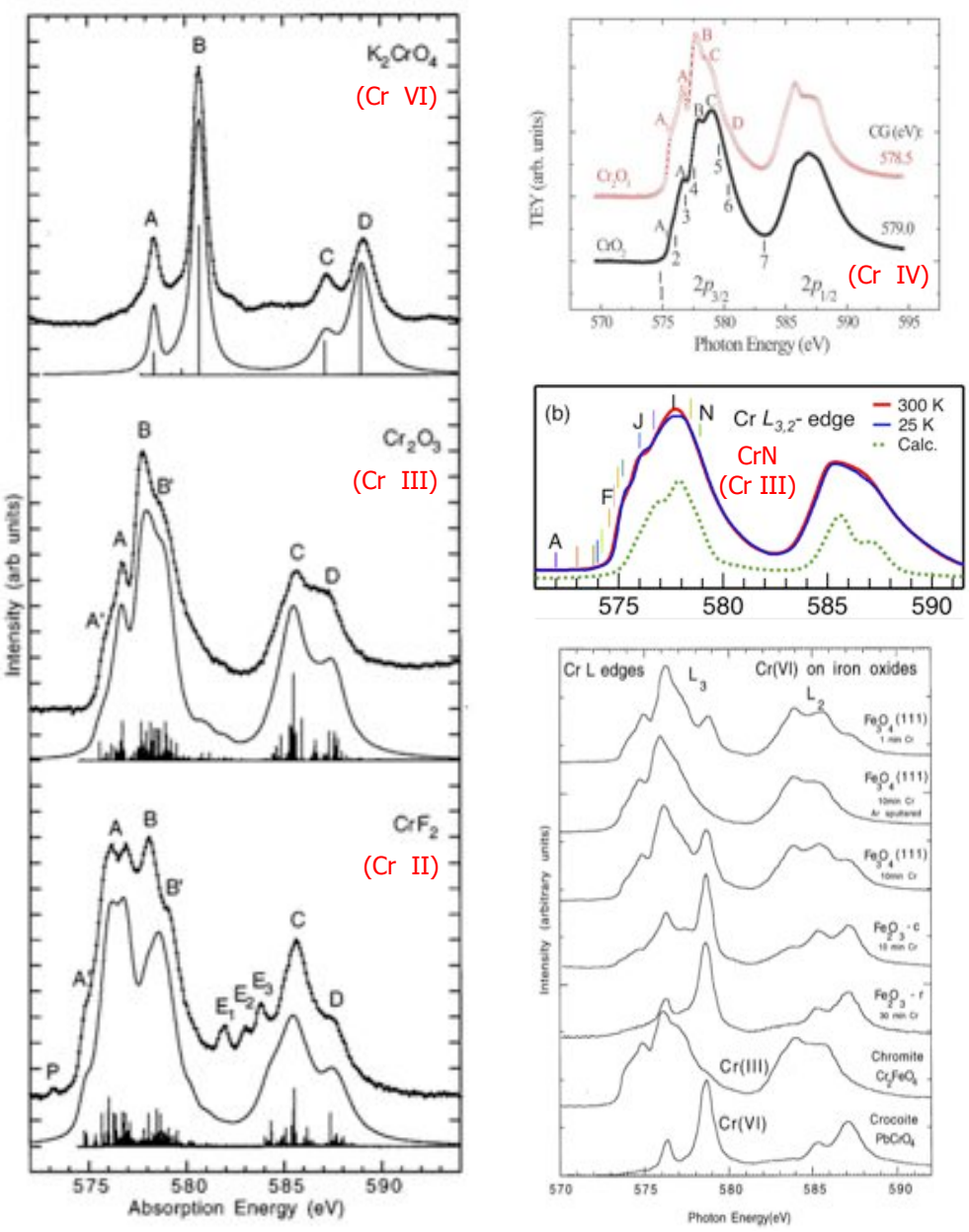

Figure 14 – Cr L-edge absorption spectra taken on several chromium compounds possessing different oxidation states (II, III, IV and VI).

4.2 Band gap tuning

4.2.1 Band gap narrowing: VB photoemission

The most important aim of the co-doping approach is the ability to induce an effective band gap shrinking. As we discussed in the introduction, the intrinsic 3.2 eV band gap of the undoped TiO_2 hampers the possibility to harvest the greatest part of the sun-light spectrum. Thus, the ability to tune the gap is of fundamental importance for any possible technological application. Hence, our spectroscopic analysis involved a thorough characterization of both the top of the VB and the bottom of the CB. First, we probed the filled states present at the top of the VB by means of XPS.

The photoemission spectrum measured on the Cr-N-TiO_2 sample is presented in Fig. 15 along with the same region acquired on an undoped TiO_2 sample and on the SCBD N-TiO_2 one (see Chap. 3.4.2). The codoped SCBD sample exhibits a lineshape very similar to the N-doped sample. However, a rigid shift of ~0.3 eV towards lower binding energies of the whole O 2p – Ti 3d band is evident. On the contrary, the N-doped film does not present any kind of rigid shift of the entire VB, as also reported by Batzill et al. for a TiO_2 single crystal after N ion implantation [BatzillPRL2006]. Moreover, this rigid shift is not found in Cr-only doped samples, as confirmed by VB spectra recently shown by Osterwalder et al. and Nolan et al. for Cr-only doped TiO_2 samples [Osterwalder2005, Nolan2009]. This suggests that the rigid shift is a direct consequence of the simultaneous Cr-N codoping.

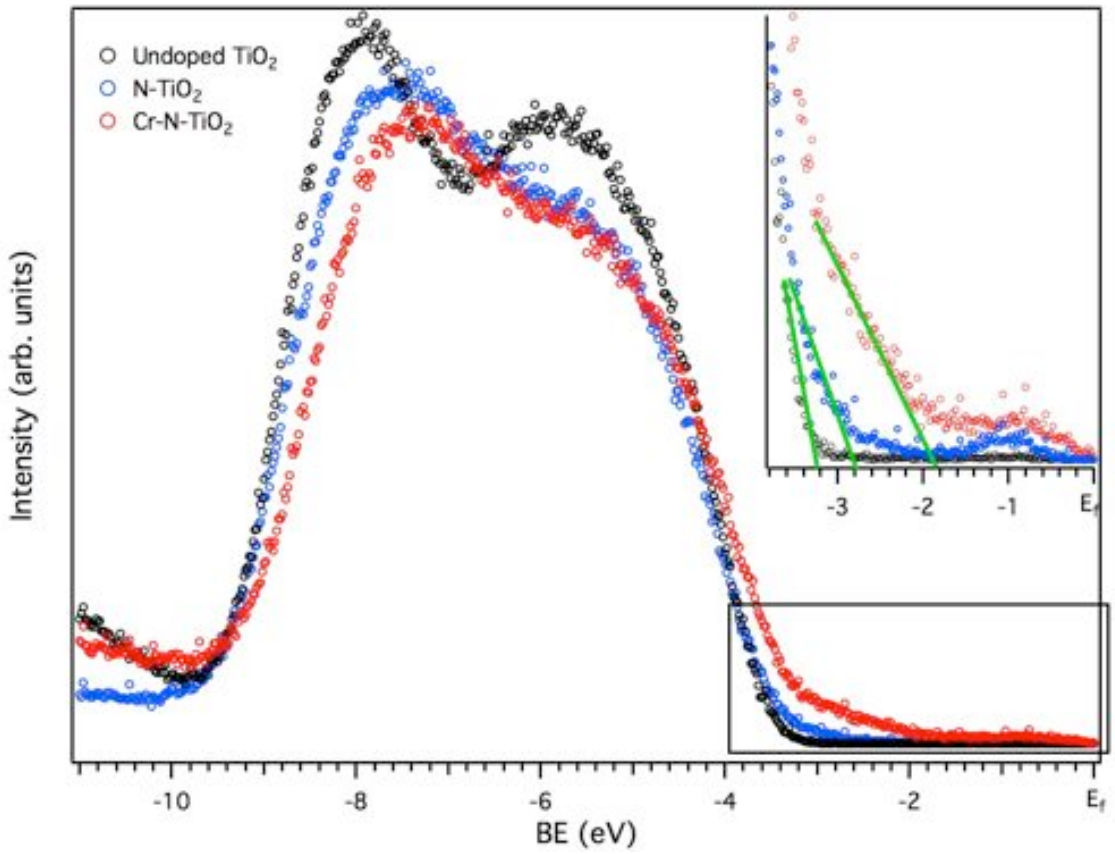

Figure 15 - VB photoemission spectra taken on Cr-N- and N-doped SCBD films (red and blue markers, respectively) along with a reference spectrum acquired on undoped TiO_2 (black markers).

The Cr-N-TiO_2 sample presents the same peak centered around 1 eV BE, as already seen for the N-only doped specimen. We attributed this component to Ti 3d states related to oxygen vacancies (see Chap. 3). Upon doping with Cr atoms, above the top of the valence band a new broad state appears around 2.6 eV. The low cross section of the VB photoemission probed with Al K-alfa photons (hv= 1486.7 eV) makes a precise estimation difficult, but we can safely attribute this component to Cr 3d states, as also found for Cr-doped TiO_2. Nonetheless, a comparison with the N-TiO_2 data suggests that also N 2p states probably contribute to this broad feature.

Since the peak centered at 1 eV BE is known to be suppressed as the sample faces air [BattzillPRL2006], the Cr-related component should be the one closing the gap on the filled states side. Hence, if the CB does not exhibit any appreciable variation, the band gap should be reduced to ~1.8 eV in the Cr-N codoped SCBD film. This value is close to the value estimated by Zhu et al. on codoped TiO_2 nanoparticles with STS (band gap = 1.5 eV) [ZhuPRL2009], confirming the effectiveness of the co-doping approach in reducing the titania intrinsic band gap.

To better characterize the valence band structure and the chemical decomposition of the filled states, we conducted a Resonant Photoemission (RESPES) analysis. As described in Chap. 2, the chemical sensitivity of this experimental technique allows to identify which element is responsible for a specific spectral feature in the VB. Moreover, additional information regarding the electron's hopping probability and the orbital delocalization can be argued from the resonance behavior as a function of the incident photon energy [Bruhwiler2002]. Since our main interest was to clarify the variations induced by the n-type and p-type dopants in the band gap, we gathered VB spectra using photons whose energy was close to the N 1s and the Cr 2p BEs (~400 eV and ~575 eV, respectively).

The Cr-edge resonant behavior is presented in the left panel of Fig. 11, along with the XAS spectrum measured on the same sample (right panel). The VB photoemission matches what presented in Fig.10, with a broad O 2p – Ti 3d feature between 3 and 10 eV BE [ref]. The photoemission spectra are complicated by the contemporary presence of two core level emissions around 23 eV and 38 eV BE. These features are ascribed to Ti 3p and O 2p photoelectrons [Thomas2003]. All these features present a similar intensity decrease as the incident photon energy is increased. This effect is related to the decreasing photoionization cross-sections for the Ti 3p, the O 2s and the VB emissions in the 570-600 eV range [Yeh1993].

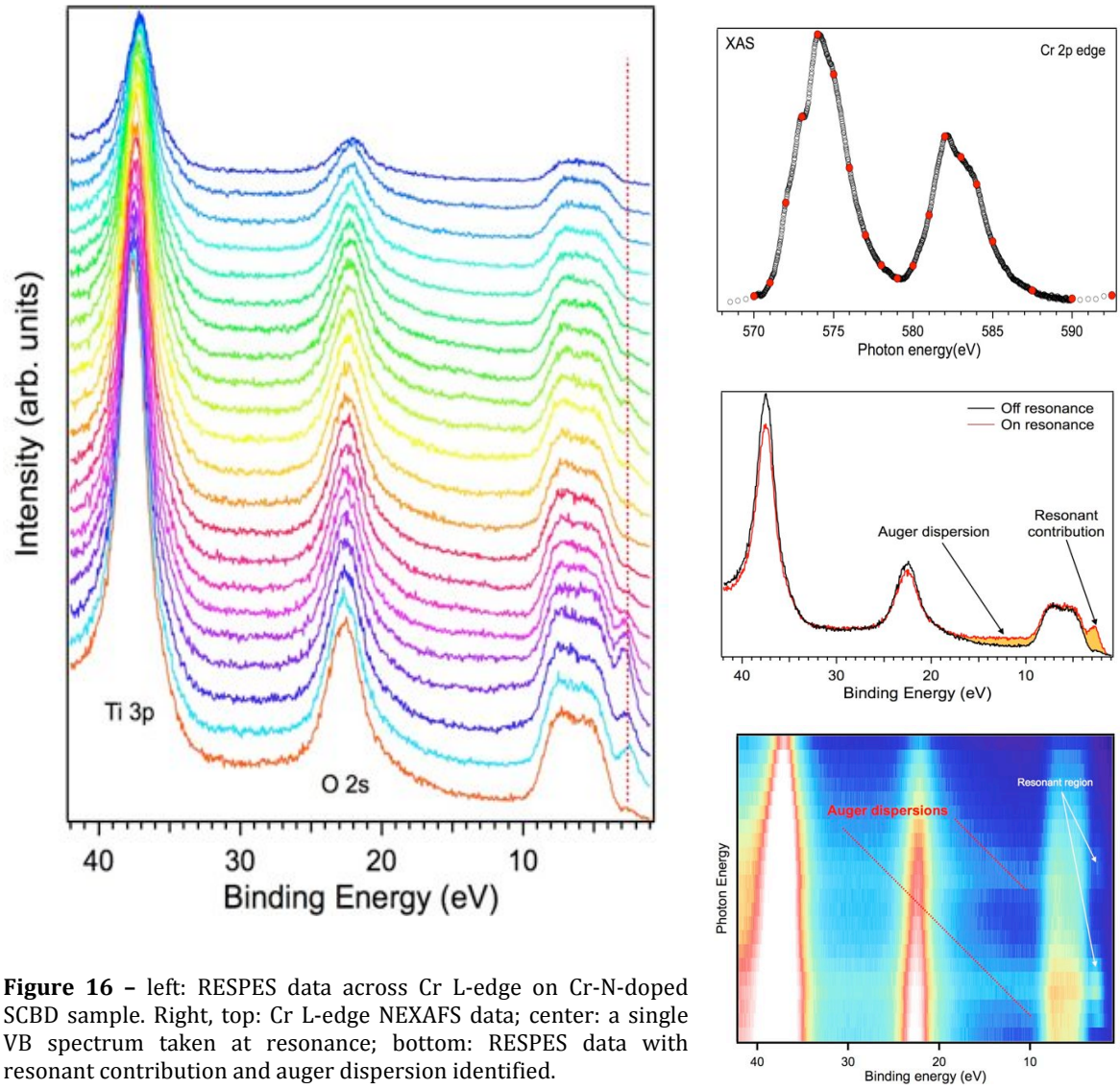

Figure 16 – left: RESPES data across Cr L-edge on Cr-N-doped SCBD sample. Right, top: Cr L-edge NEXAFS data; center: a single VB spectrum taken at resonance; bottom: RESPES data with resonant contribution and auger dispersion identified.

A strong modulation occurs at the top of the VB portion of the spectra (~3 eV BE) as the incident photon energy reaches the resonance values (see Fig.12). This strong resonant behavior confirms that those states are mainly Cr-related, as argued from the photoemission data discussed in the previous section. Moreover, the presence of such strongly resonating feature clearly indicates that the electrons excited in the LUMO states are localized [ChenAPL2006].

It is interesting to note that, as expected, the resonant peak integral intensity varies resembling the corresponding XAS lineshape (compare Fig. 17 and Fig. 13). Moreover, even if a detailed quantitative analysis is hampered by the very low signal coming from the dopants (Cr and N concentration ranges from ~5% to ~10%), a weak but noticeable Auger peak is found as the ionization edge is crossed (see bottom right part of Fig. 15). With such low signal-to-noise ratio, discriminating the origin of this Auger peak (pure Auger or Raman-Auger peak, see Chap. 2) is not possible. Still, one can argue that the contemporary presence of the resonant features along with the Auger component is compatible with a core-hole state lifetime longer than the charge-transfer time [Vijayalakshmi2007].

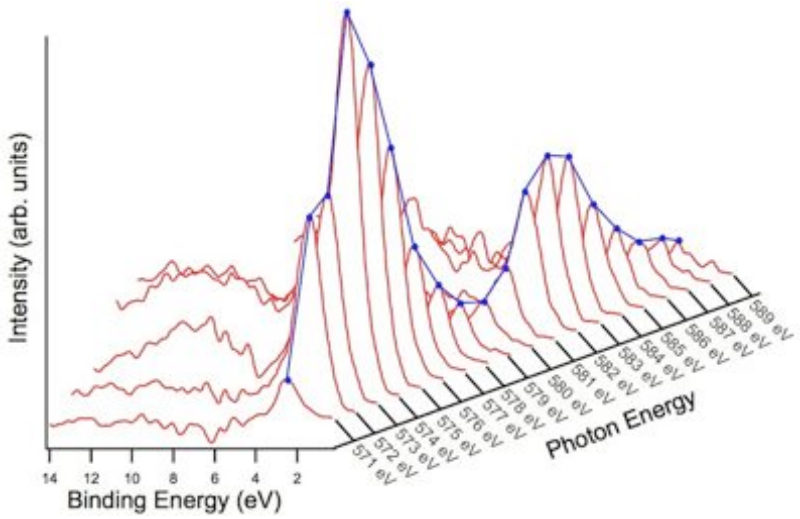

Figure 17 – Pure resonant contribution for Cr-edge RESPES, Blue line is a guide to the eye showing the that the dependence of the resonant peak resembles the corresponding XAS line profile.

Resonant photoemission spectra were also collected with photon energy varying across the *N 1s* $\rightarrow \pi^*$ absorption threshold and the results are presented in Fig. 18. The Cr-edge RESPES spectra previously discussed, clearly showed a strongly resonantly enhanced peak in the 2-4 eV BE region along with low-intensity Auger peaks. In contrast, in the N-edge data, the resonant enhancement is not detected. On the other hand, a low-intensity component is found when the incident photon energy reaches the

absorption edge (i.e. hv > 393 eV). This component appears to be shifted towards higher BEs as the incident photon energy increases (see black dotted line in Fig. 12). The quantitative analysis of these RESPES spectra is complicated by the contemporary presence of the Ti- and O-related core level peaks as well as by the low intensity originating form the low concentration of the dopants (see Fig. 18).

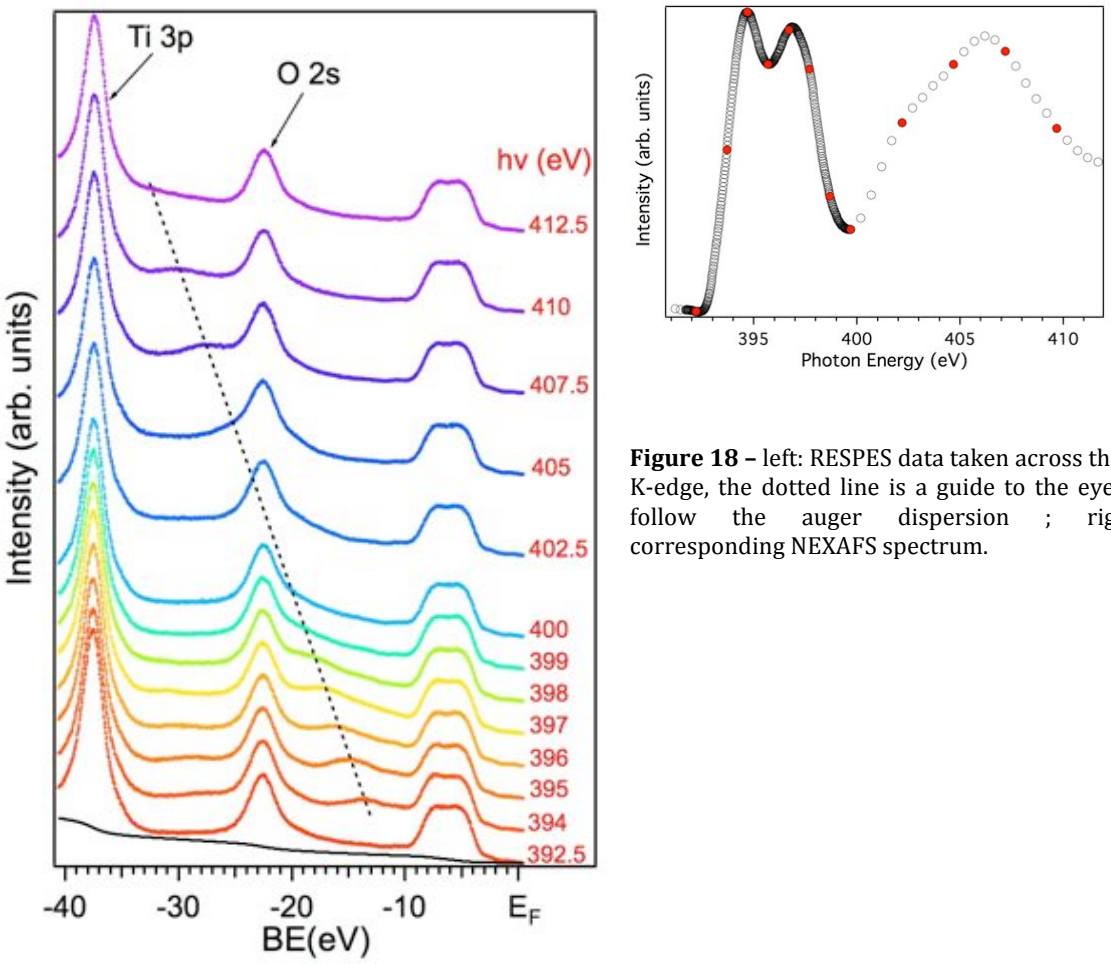

Figure 18 – left: RESPES data taken across the N K-edge, the dotted line is a guide to the eye to follow the auger dispersion ; right: corresponding NEXAFS spectrum.

Hence, our analysis involved the removal of the Ti 3p and the O 2s peaks from the experimental data, along with a Shirley background subtraction. The results of this

procedure (Fig. 19) univocally identify the component found in the N-edge spectra as an Auger peak.

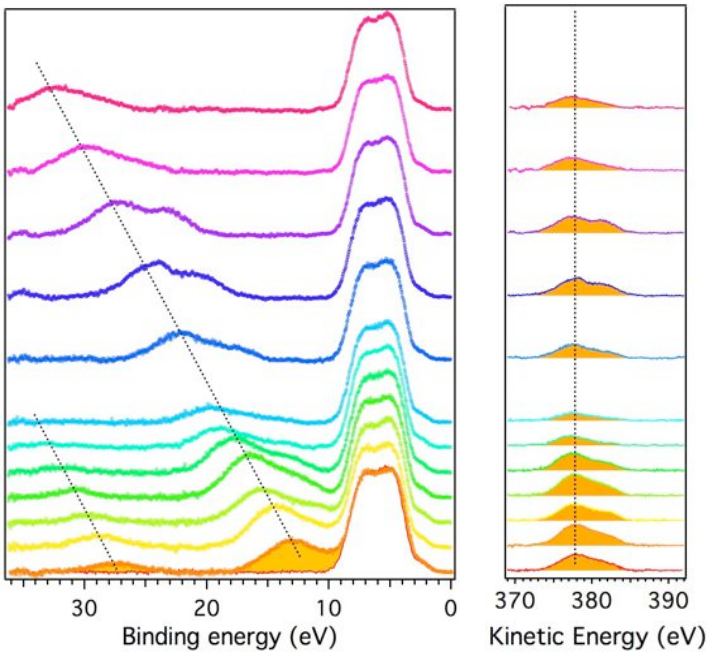

Figure 19 – Same RESPES data presented in Fig.18 after a Shirley background subtraction and the removal of the Ti 3p and the O 2s contributions. The same data are presented as a function of the Binding Energy (left) and of the Kinetic Energy (right)

In fact, it is clear that the kinetic energy of this peak is constant and independent from the incident photon energy (see the right panel in Fig. 19). This indicates that the core hole decays via a normal Auger process during the N 1s core-hole lifetime (~6 fs) [Westermark2002]. As discussed in Chap. 2, the presence of the Auger contribution and the contemporary absence of any resonantly enhanced peak suggests that the excited electrons are quickly (i.e. $t_{CT} << t_C$) delocalized, following a process similar to the one presented in the right panel of Fig. 20 [Bruhwiler2002]. This results in the suppression of any resonant contribution leaving the Auger channel as the only core-hole decay available. Still, the picture provided in Fig. 19 could be misleading: the process described is strictly true only for a thin film strongly coupled to a metal substrate (i.e.

the excited electrons are delocalized in the conduction band of the substrate). In our case, we are dealing with a cluster-assembled film, in which there is no coupling with the substrate. Therefore, the delocalization of the XAS electrons over the entire film in band-like states is only one of the possible interpretations of our RESPES data. On the other hand, another possible explanation could be that these electrons are quickly delocalized on energy levels that are still confined inside a single cluster's volume. This "confined" delocalization can still explain the quenching of the resonant contributions in the RESPES spectra, but would also imply that the N-related impurity states would be unable to effectively transport the photoexcited charge carriers throughout the entire film. Thus, the charge carriers would only be partially able to reach a possible contact region, reducing the benefits induced by any band gap reduction.

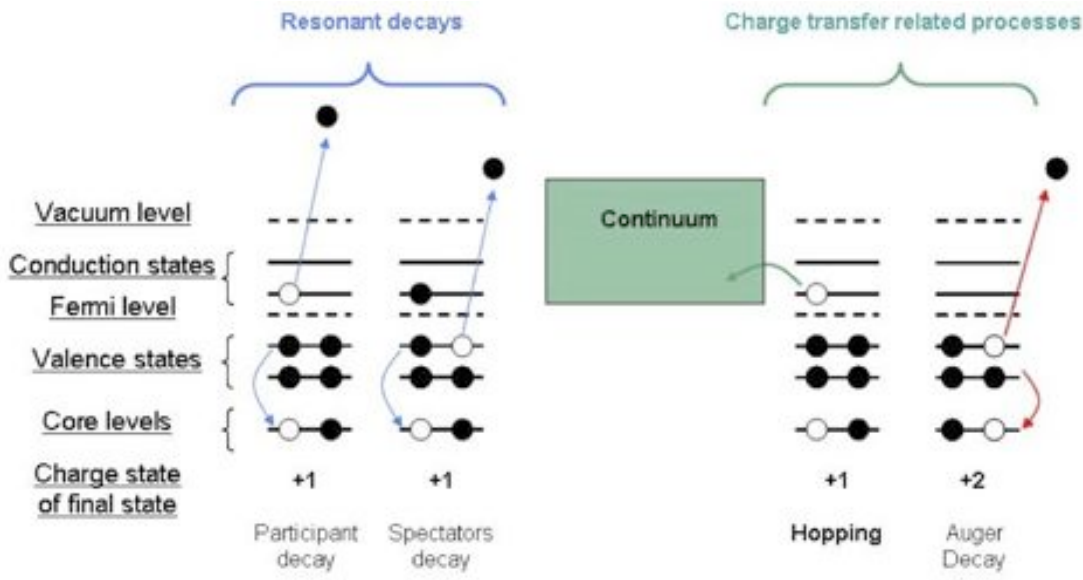

Figure 20 – Schematic view of the two main pathways for deexcitation of a system that is coupled to a (substrate) continuum. After excitation, autoionization may occur as usual (left), where we include only the participant channel to emphasize the role of the excited electron. Alter- natively, the excited electron may tunnel into the continuum (right side), opening an Auger channel.

Our results confirm that the features found at the top of the VB are N- and Cr- related states. Moreover, the RESPES data suggest that, while the Cr- derived orbitals in the Valence Band are essentially localized, the N- derived ones are much more delocalized.

4.2.2 Optical Absorption

Valence Band photoemission and RESPES data suggest that our SCBD Cr-N codoped films possess impurity states inside the TiO_2 band gap. Since the existence of such states is fundamental for photovoltaic applications, we investigated the cluster-assembled film using optical absorption spectroscopy. Since this technique does not involve any core-hole excitation, no inner potential (i.e. core-hole screening) affects the electronic structure of the system. Thus, a direct estimation of the optical band-gap is possible.

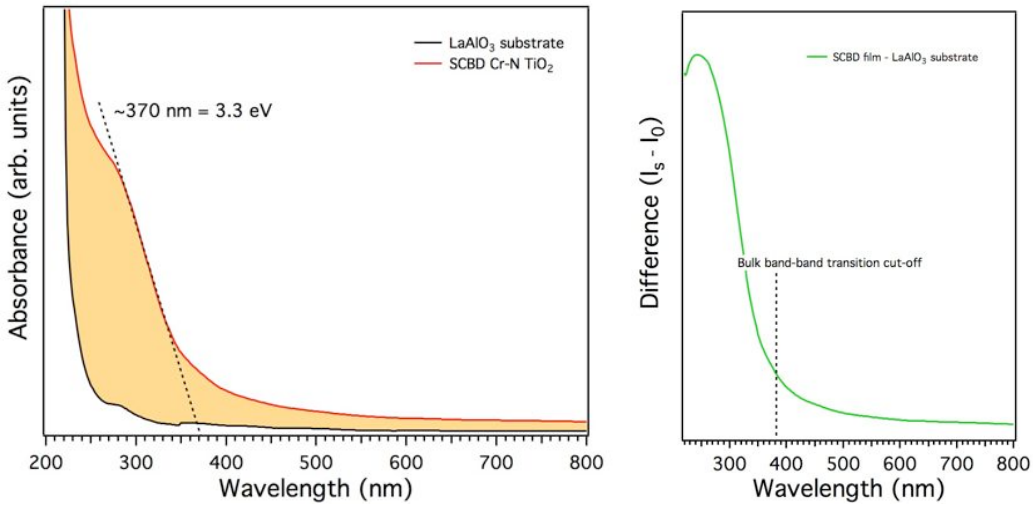

Figure 21 – (*Top*) Optical absorption spectra taken on the SCBD Cr-N codoped TiO_2 film along with a reference spectrum taken on the bare substrate ($LaAlO_3$, Band gap ~5.0 eV [Wang2007]). The dotted line indicates the band-to-band transition of bulk TiO_2 (~3.75 nm – 3.3 eV). (*bottom*) Difference between the two spectra plotted in the top panel (I_s= sample, I_0= substrate) [Eres2009].

In order to isolate the contributions coming from the Cr-N TiO_2 film only, we conducted the same analysis also on the bare substrate. In order to minimize any spurious contribution to the film's absorption spectra, an insulating substrate with a large band gap is preferred. Therefore, in this case, we used $LaAlO_3$ (band gap ~5.0 eV [Wang2007]).

The SCBD Cr-N TiO_2 absorption spectrum exhibits a broad feature whose cut-off at λ= 370 nm (left panel in Fig. 16) is compatible with the main band-to-band transition in undoped TiO_2 nanoclusters (~3.3 eV) [Barborini2005]. Beyond that threshold, the signal drops, indicating that most of the visible light is not absorbed by the system. Still, looking at the pure signal coming from the Cr-N-TiO_2 film (right part of Fig. 16) a quite long absorption tail is still clearly measured. This low-intensity signal is hard to evaluate, since it can be associated with the Cr-N states found at the top of the VB (see Chap. 4.1.4) or with a simple smearing of the main absorption cut-off due to impurities, to the porous structure of the film or to spectrometer limitations. Nonetheless, even if the VB impurity states might play a role in slightly extending the absorption edge into the visible region, this effect seams to be weak, hampering the chance to significantly enhance the number of photo-excited charge carriers inside the film.

4.2.3 Conclusions

In this chapter, we demonstrated that SCBD Cr-N codoped TiO_2 films can be grown using the PMCS set-up described in Chap.3. Both the Cr and the N dopants are injected into substitutional sites inside the titania clusters. The introduction of the Cr together with the N atoms strongly modifies the occupied states at the top of the VB. The band gap is reduced due to localized Cr- and delocalized N-related occupied states, as suggested by the RESPES measurements. Although, the cluster-assembled structure of the SCBD film probably hampers a significant shift in the optical absorption. These peculiar properties of the Cr-N doped nanoclusters, make them a very promising candidate for photocatalytic applications rather than for photovoltaic cells.

References

[ZhuPRL2009] Zhu W. et al., *Phys. Rev. Lett.* **103**, 226401 (2009).

[Fujishima1972] Fujishima A. and Honda K., *Nature* **238**, 37 (1972).

[Dieboldreview] Diebold U., *Surf. Sci. Rep.* **48**, 53 (2003).

[Chambersreview] Chambers S.A., *Surf. Sci. Rep.* **39**, 105 (2000).

[Serpone2006] Serpone N., *J. Phys. Chem. B* **110**, 24287 (2006).

[Nakano2007] Nakano Y. et al., *Chem. Phys.* **339**, 20 (2007).

[ThetisWebsite] http://www.tethis-lab.com/products-coatings-scbd_pmcs.html

[Cassina2009] Cassina V. et al., *Phys. Rev. B* **79**, 115422 (2009).

[Apewebsite] http://www.elettra.trieste.it/experiments/beamlines/ape/index.html.

[Unveren2004] Unveren E. et al., *Surf. Interface. Anal.* **36**, 92 (2004).

[Slebarski2001] Slebarski A., Neumann M. and Schneider B., *J. Phys.: Condens. Matter* **13**, 5515 (2001).

[Fadley1969] Fadley C.S. et al., *Phys. Rev. Lett.* **23**, 1397 (1969).

[Pollini2001] Pollini I., Mosser A. and Parlebas J.C., *Phys. Rep.* **355**, 1 (2001).

[ZimmermannJPhysCondmat1998] Zimmermann R. et al., *J. Phys.: Condens. Matter* **10**, 5697.

[Bertoti2002] Bertoti I., *Surf. Coat. Tech.* **151**, 194 (2002).

[Mcfeely1972] McFeely F.R. et al., *Phys. Lett. A* **49**, 301 (1972).

[Shirley1975] Shirley D.A., *Phys. Scr.* **11**, 117 (1975).

[VanVleck1934] Van Vleck J.W., *Phys. Rev.* **45**, 405 (1934).

[VanAcker1988] Van Acker J.F. et al., *Phys. Rev. B* **37**, 6827 (1988).

[Zimmermann1998] Zimmermann R. et al., *J. Electron Spectrosc. Relat. Phenom.* **96**, 179 (1998).

[Tsurkan2000] Tsurkan V. et al., *Solid State Comm.* **114**, 149 (2000).

[SorianoSurfSci281] Soriano et al., *Surf. Sci.* **281**, 120 (1993).

[Kendelewicz1999] Kendelewicz T. et al., *Surf. Sci.* **424**, 219 (1999).

[Theil1999] Theil C., van Elp J. and FolkMann F., *Phys. Rev. B* **59**, 7932 (1999).

[deGroot1989] de Groot F.M.F. et al., *Phys. Rev. B* **40**, 5715 (1989).

[deGroot1990] de Groot F.M.F. et al., *Phys. Rev. B* **41**, 928 (1990)

[Dedkov2005] Dedkov Y.S. et al., *Phys. Rev. B* **72**, 060401 (2005).

[Bhobe2010] Bhobe P.A. et al., unpublished data (2010).

[Garcia2004] Gracia F. et al., *J. Phys. Chem. B* **108**, 17466 (2004).

[BatzillPRL2006] Batzill M., Morales E.H. and Diebold U.; *Phys. Rev. Lett.* **96**, 026103 (2006)

[Osterwalder2005] Osterwalder J. et al., *Thin Solid Films* **484**, 289 (2005).

[Nolan2009] Nolan M., Mulley J.S. and Bennett A., *Phys. Chem. Chem. Phys.* **11** 2156 (2009).

[Kaspar2005] Kaspar T.C. et al., *Phys. Rev. Lett.* **95** 217203 (2005).

[Mischie1988] Mischie S., Mathieu H.J. and Landolt D., *Surf. Interface Anal.* **11**, 182 (1988).

[Bruhwiler2002] Bruhwiler P.A., Karis O. and Mårtensson N., *Rev. Mod. Phys.* **74** 703 (2002).

[Thomas2003] Thomas A.G. et al., *Phys. Rev. B* **67**, 035110 (2003).

[Yeh1985] Yeh J.J. and Lindau I., *Atomic Data and Nuclear Data Tables* **32**, 1 (1985).

[Yeh1993] Yeh J.J., *Atomic Calculation of Photoionization Cross-Sections and Asymmetry Parameters,* Gordon and Breach Science Publishers (1993)

[ChenAPL2006] Chen W. et al., *App. Phys. Lett.* **88**, 184102 (2006).

[Vijayalakshmi2007] Vijayalakshmi S., *Phd thesis, Physics dept., University of Hamburg,* Germany (2007).

[Westermark2002] Westermark K. et al., *Chem. Phys.* **285**, 167 (2002).

[Wang2007] Wang X. et al., *Physica B: Cond. Matt.* **392**, 104 (2007).

[Barborini2005] Barborini E. et al., *Adv. Mat.* **17**, 1842 (2005).

[Eres2009] Eres G. et al, *to be published*.

Introduction

As discussed in the previous chapter, the band gap width is a fundamental issue limiting the use of TiO_2 in photocatalytic and photovoltaic applications. In chap. 4, we presented a new approach to this problem, using Cr-N codoped nanoclusters films. Even though our results using cluster-assembled films appear to be very promising, a fundamental issue has to be taken into account when dealing with highly porous and defective systems like nanostructured films. In fact, on one hand their extremely high reactivity can provide a much easier route to substitutionally embed dopants (Cr and N atoms, in this case) inside the film, possibly generating a stronger and more effective band gap reduction. On the other hand, the size of the single clusters can also be counterproductive for pursuing such goal, since the clusters' nanometric dimension (<10 nm in our SCBD films) is close to the electron's associated wavelength (~2 nm for a kinetic energy of 1 eV). In this case, quantum-size effects can play a major role in the electrons' dynamics. Moreover, it is know that such effects tend to spread the energy levels accessible to electrons in solids possessing low dimensionality [Messiah]. Hence, in our case, the energy gap between VB and CB could be even enhanced due to the nanoclusters' size.

Also another important aspect should be carefully taken into account in the choice of a proper film structure: the transport properties of the deposited layer. In fact, an effective reduction of the band gap allows harvesting a greater portion of the incoming light creating a larger number of electron-hole pairs (often referred as "excitons"). Nonetheless, to fully take advantage of this enhancement, the charge carriers should be capable of traveling through the active film reaching the contacts region where they would be actually collected. In this process, scattering due to structural defects (such as nanoclusters' boundaries) can significantly lower the number of excitons reaching the contacts [ref], thus hampering the possibility to take full advantage of the band gap reduction.

In the following chapter, we will investigate these aspects analyzing crystalline TiO_2, N-only and Cr-only doped TiO_2 and Cr-N codoped TiO_2 films grown in UHV conditions by means of Pulsed Laser Deposition (PLD). Then we will put in comparison the

results obtained on the crystalline samples with those collected on the SCBD ones. This will allow to evaluate the role played by the film structure in the band gap tuning mechanism outlined in Chap. 4.

5.1 PLD deposition of epitaxial TiO_2 films

Crystalline interfaces and superlattices are a widely studied class of materials in condensed matter physics. In fact, the synthesis of such completely artificial crystalline structures has been exploited for decades allowing the growth of new compounds presenting distinct properties and new functionalities. Among the others, Transition Metal Oxides (TMO) have received much attention, as they possess a great number of interesting properties [Rao1998]. Obviously, the precise growth of such layers requires appropriate techniques allowing a high degree of precision and atomic-scale control of the constituents. For decades, Molecular Beam Epitaxy (MBE) has been considered the only technique available for such high-precision tasks [Warusawithana2003]. More recently, Pulsed-laser deposition (PLD) has been applied to the growth of interfaces with results comparable to the MBE ones, in terms of control and sharpness [WIllmott2004, Lee2005]. The technique of PLD is conceptually simple, as illustrated in Fig. 1.

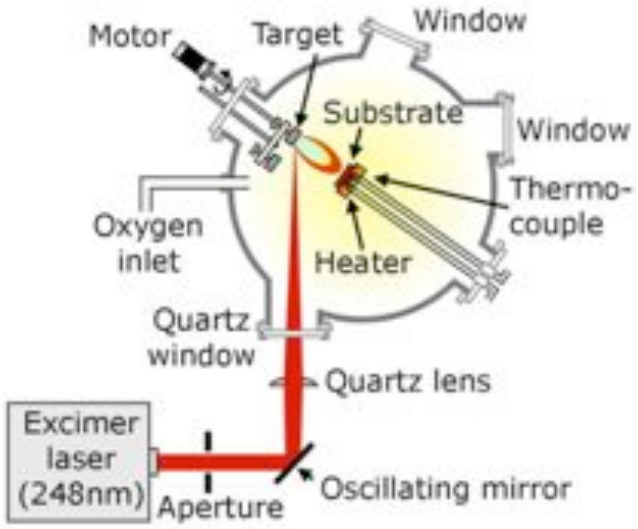

Figure 1 – Schematic representation of a standard PLD apparatus. Arrows in the figures represent axes of motion that can be controlled and synchronized. The laser beam (coming from the lower left) hits the target, forming a plasma plume. This plume expands towards the substrate (shown behind the moving slits)

A pulsed-laser beam hits a target containing the atoms to be deposited, leading to a rapid removal of material from the target and the formation of an energetic plasma plume, which then condensate onto a suitable substrate. Once the ablated material lands on a preheated substrate, it immediately crystallizes [Eres2002]. In the case of metal oxides growth, oxygen has to be supplied externally (i.e. oxygen atmosphere filling the deposition chamber) [christen2008]. PLD is extremely sensitive to many different parameters such as laser energy density on the target (often referred as "fluence"), growth pressure, background gases, substrate temperature, target-substrate distance and even oxygen flow's direction and position with respect to the target [Ohnishi2005]. Nonetheless, it is now a well established technique to deposit crystalline films up to several hundreds of nanometers thick [Shen2004].

5.1.1 Experimental

The TiO_2 films were grown using Pulsed Laser Deposition (PLD) with a KrF excimer laser (248 nm) in 13 mTorr of oxygen using a sintered TiO_2 target. A target with a mixture of CrO and TiO_2 was used to deposit Cr-doped TiO_2 film. For the growth of Cr-N codoped TiO_2, the target is a mixture of CrN and TiO_2 with different weight ratio. The oxygen was replaced by N_2/O_2 (3:1), N_2(5 %NO)/O_2 (3:1), or N_2O for the N-doped and Cr-N codoped TiO2 films to improve the N-doping concentration. The nominal doping concentration was 5% for both N and Cr species. $LaAlO_3$ and $SrTiO_3$ were chosen as substrates due to their good lattice match with bulk TiO_2. Possible effects related with the deposition temperature were investigated growing a series of samples on a holder with a temperature gradient from 800 to 350^o C. An overview of the deposited and measured samples is presented in Table 1.

The as-grown thin films were characterized for the phase formation and crystallinity by X-ray diffraction (Scintag X-1 Advanced X-ray diffractometer (XRD) 2.0°/min, Cu Kα radiation). The UV-vis absorption spectra in the range of 350–1000 nm were recorded with a Photonics 400 Series UV/Vis Spectrophotometer in transmission mode. XPS spectra were obtained by using a K-Alpha Omicron XPS system (Al Kα 1486.6 eV).

The spectroscopic characterization were carried out with same equipment described in details in Chap.4.

Deposited samples		Low-T°	Medium-T°	High-T°
Pure Anatase		250°	550°	800°
Anatase+rutile mixed phase		350°	550°	800°

Table A – A list of PLD samples along with the deposition temperatures.

5.1.2 Film structure and crystallinity: XRD results

X-Ray Diffraction (XRD) is a powerful and simple technique to characterize films' crystalline lattice and structural quality. As in any other diffraction technique, XRD results should be considered, in first approximation, as reflecting averaged properties of the bulk of the system under consideration. Thus, in our case, they are taken as mere indication of the overall crystal structure. Therefore, no quantitative analysis of the diffraction pattern is needed here.

A typical set of XRD results obtained on PLD undoped TiO_2 is presented in Fig.2.

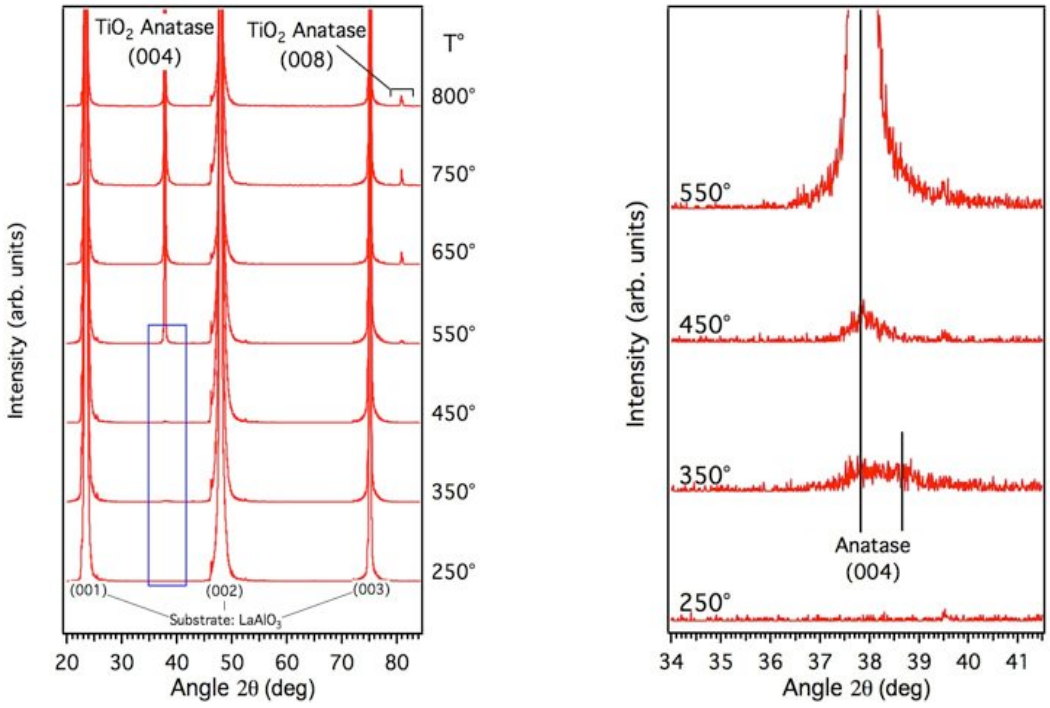

Figure 2 – *(left)* XRD pattern for PLD TiO2 film deposited on LAO. *(right)* magnification of the region enclosed in the blue square in the left panel, showing the small amount of crystalline TiO_2 nucleation at low temperature (350°-450°) [Eres2009]

The diffraction patterns are displayed as a function of the growth temperature (i.e. the substrate temperature during the deposition) ranging from 250°C up to 800°

(left panel). Three strong components are well resolved at ~ 23°, 48° and 76°, these are attributed to diffracted photons coming from the $LaAlO_3$ substrate [Toro2010]. No other components are found when the film is grown at 250°, suggesting that the TiO_2 is amorphous at this point. When the deposition temperature reaches 550° new peaks clearly emerge at ~38° and 81°. These new components are attributed to TiO_2 possessing an anatase crystal structure [Ohsawa2009]. Even if the latter XRD peaks are evident at 550° and beyond, it is important to mention that a small peak in the same angle region is found also at 350° and 450° (see right panel in Fig.2). This suggest that the nucleation of small TiO_2 crystallites dispersed throughout an amorphous titania matrix is possible even at lower temperatures, but in limited amounts.

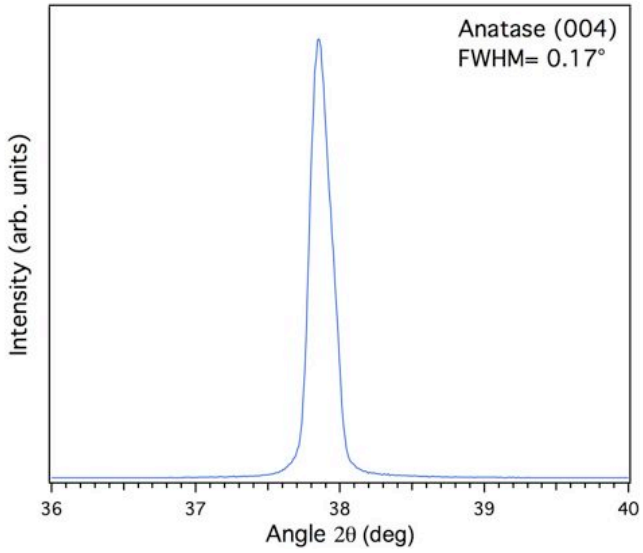

Figure 3 – XRD rocking curve taken on the PLD sample grown at 750° [Eres2009].

It is commonly agreed that from the width of an XRD peak one can extrapolate some information about the degree of crystallization [Chen2007, Kholmanov2003]. More precisely, the FWHM of the so-called rocking curve (shown in Fig. 3) is directly related to the quality and the extent of the crystalline structure of the deposited film (anatase, in our case) [Gall2002]. Our estimation gives a value 0.17° for the FWHM (considering the sample grown at 750°C), which suggests that our PLD film

possesses a very good degree of crystallinity, comparable to what obtained using MBE growth [Fisher2006].

The same diffraction analysis was carried out on the doped TiO_2 samples (N-only, Cr- only doped and Cr-N codoped films). A representative set of XRD patterns are shown in the left panel of Fig.4 for a set of Cr-N codoped films grown at different temperatures.

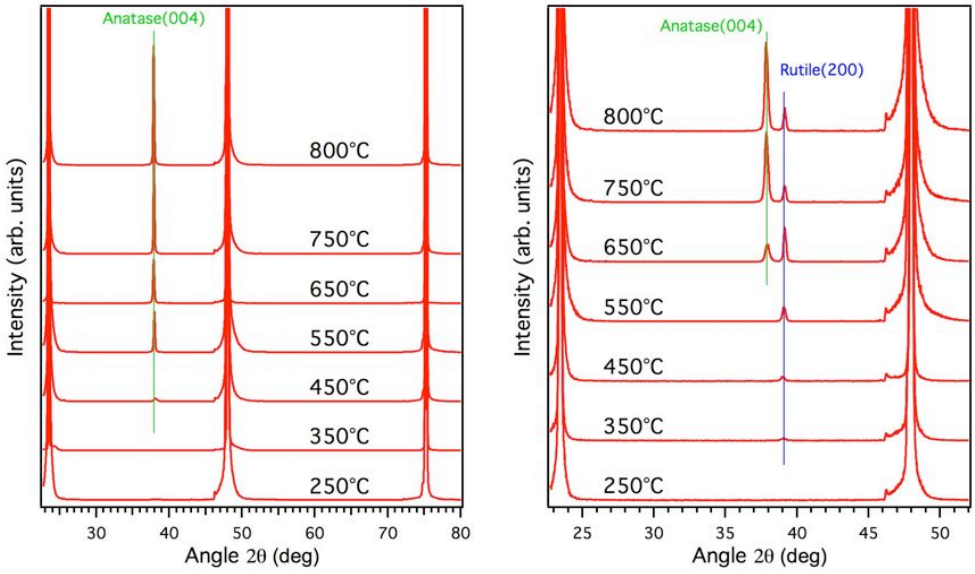

Figure 4 – XRD patterns for Cr-N codoped TiO2 films [Eres2009]

The XRD data resemble what found for pure TiO_2, with the anatase phase starting to grow beyond 350°C, confirming that PLD can be successfully used to deposit epitaxial Cr-N doped TiO_2 films.

PLD is also a versatile technique, allowing the growth of different crystalline phases, provided a fine control on the deposition conditions. This is shown in the right panel of Fig.4, where a second set of XRD spectra is plotted. In fact, by slightly varying the partial pressures of O_2 and N_2 inside the chamber during the film growth, one can obtain also a rutile* nucleation (blue line in Fig. 4). Surprisingly, the rutile phase

*NOTE: Hereafter, the two sets of samples discussed in Fig.4 will be referred as "pure anatase" samples (left side) and "anatase-rutile" mixed phase samples (right side). This is done for sake of simplicity, even if some of them are not rigorously mixed phase samples (i.e. films grown below 600°C present only rutile structure, see Fig.4)

appears to be nucleating at low temperatures, with anatase becoming the dominant phase at high temperatures. This growth behavior is reversed with respect to what is normally observed for TiO_2, with anatase being the low-T° phase and rutile the high-T° one [Dachille1968]. Still, as recently suggested by Sa Li [SaLi2009], an anatase-to-rutile conversion can take place upon transition metal doping.

The results obtained for the Cr-only and N-only doped samples are similar to what observed for the codoped ones, as briefly shown in Fig. 5 where the diffraction pattern obtained for the single doped specimens are compared to the codoped one (all of the samples compared here were grown at the same temperature of 800°C).

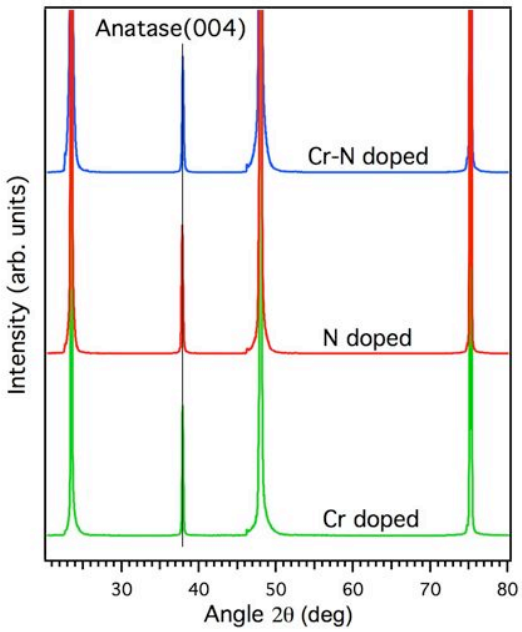

Figure 5 – XRD results for Cr-only, N-only and Cr-N doped samples. No phases other than anatase are observed [Eres2009].

Therefore, we can safely conclude that PLD allows a high-quality epitaxial growth of undoped, Cr-doped, N-doped and also Cr-N codoped TiO_2.

5.1.3 Chemical composition: XPS results

The structural analysis discussed in the previous part clearly demonstrates that high-quality, crystalline TiO_2 films can be grown by means of Pulsed Laser Deposition. Still, to gather precise information about the Cr and N atoms diluted inside the titania matrix, (such as atomic concentration, lattice sites and electronic configuration) XPS analysis is of fundamental importance. In the last decade, epitaxial N- and Cr-doped TiO_2 films have been widely studied both theoretically and experimentally [Braun2010, Diwald2004, Livraghi2006, Kaspar2005, Nolan2009] Thus, our present investigation is primarily focused on the Cr-N codoped films, since they promise to be more effective than the single doped ones, as discussed in the previous chapter.

The XPS spectra confirm that N and Cr atoms are successfully introduced in most of the samples (Fig.6).

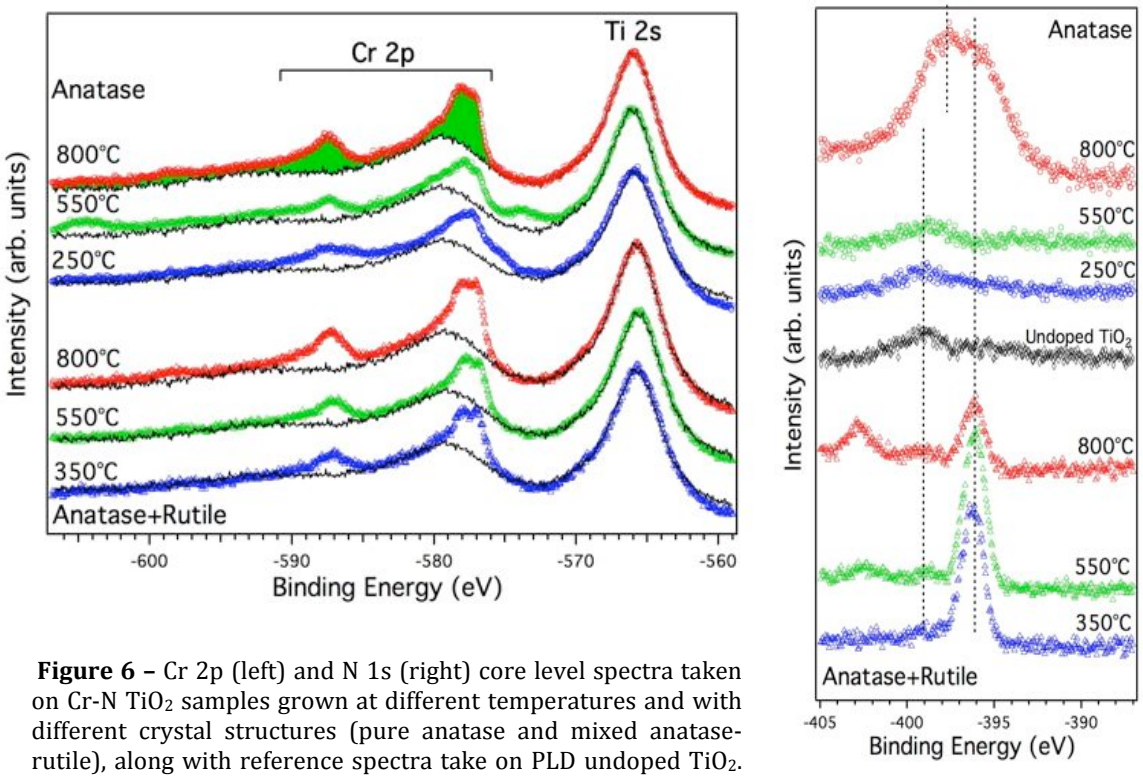

Figure 6 – Cr 2p (left) and N 1s (right) core level spectra taken on Cr-N TiO_2 samples grown at different temperatures and with different crystal structures (pure anatase and mixed anatase-rutile), along with reference spectra take on PLD undoped TiO_2. All the samples were measured *ex situ* in UHV conditions after an annealing procedure up to 500°C.

Cr 2p core level spectra taken on the six different samples are presented in Fig. 6a, along with a reference spectrum taken on a PLD undoped TiO_2 film. The latter was

used to isolate the contribution originating from the Cr atoms only (green area), following the procedure described in details in Chap.4. The results of this analysis are shown in Fig.7 for the anatase-rutile specimens, along with the results of a least-squares fitting procedure conducted on the sample grown at 800°C.

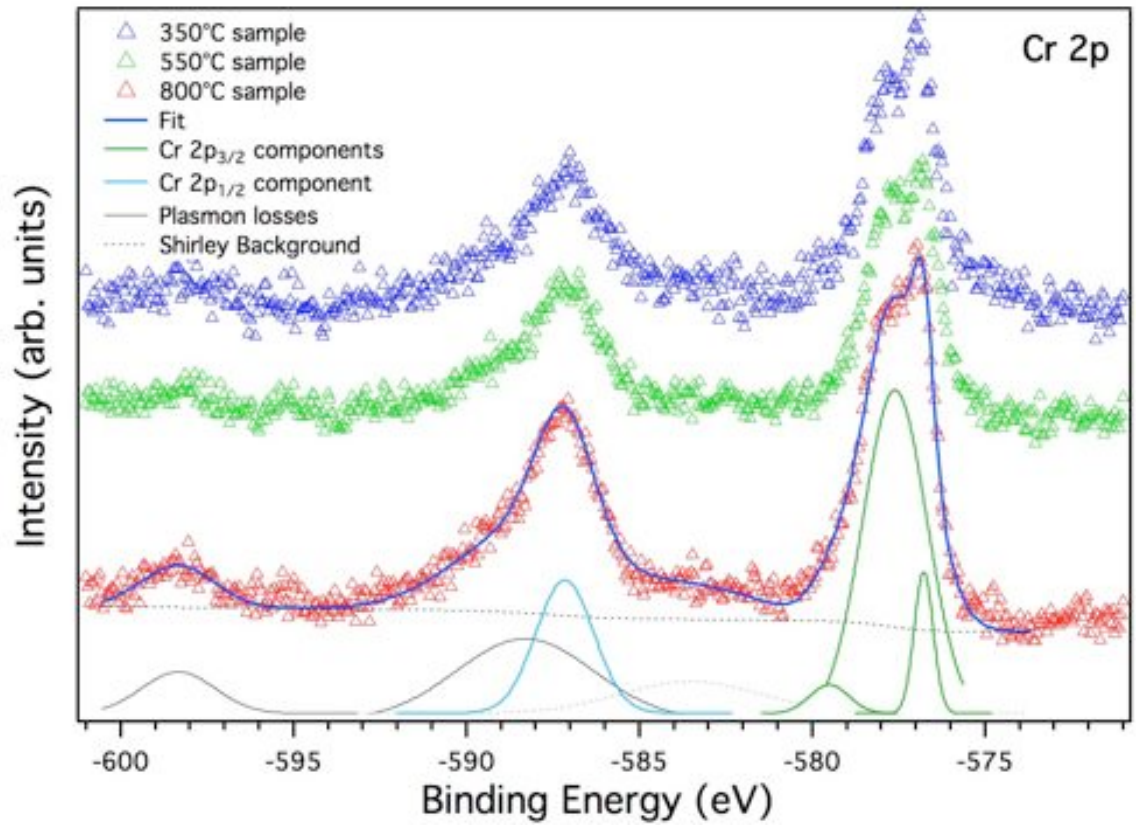

Figure 7 – Cr 2p for mixed rutile-anatase TiO2 samples and fit

The three anatase-rutile samples present very similar spectra, with essentially unchanged lineshapes upon deposition temperature variations. Thus, the result of the fitting procedure carried out on the 800°C sample can be considered as representative of all the three spectra.

It is evident, especially considering the $2p_{3/2}$ emission, that the lineshape is quite complicated, with several components clearly present. It is fundamental to bear in mind that these spectral structures are not to be directly ascribed to different phases present inside the sample, but they must be thought as originating from multiplet splitting and satellite emissions [Chambers2001, Unveren2004]. In fact, as outlined

by Gupta and Sen [Gupta1975], more than 60 multiplets for the 2p orbital of the Cr^{3+} free ion have been calculated. However, all these individual multiplet components cannot be resolved experimentally and, at the highest resolution, only "bundles" of closely spaced multiplet features can be resolved. Consequently, in our fitting procedure we used several peaks in order to take into account such multiplet structure. Our situation is even more complicated due to the small amount of chromium dopants inside our films, resulting in low-intensity Cr-related photoemission peaks. Moreover, the contemporary presence of three different atomic species (Ti, O, N) possibly interacting with Cr can give rise to additional features, complicating the XPS data analysis.

The Cr $2p_{3/2}$ and $2p_{1/2}$ are found around 577.5 eV and 587 eV respectively, along with the two corresponding plasmon losses found 10.2 eV away from the main peak (black peaks in Fig.7). Moreover, an additional component is barely noticeable around 583 eV BE (dotted peak), roughly 5 eV away from the main $2p_{3/2}$ peak, as also predicted by Ilton et al. [Ilton2003].

The $2p_{3/2}$ feature is composed by at least three different peaks at 576.8, 577.6 and 579.5 eV BE, typically found in chromium oxides such as Cr_2O_3 and also $Cr_{2-x}Ti_xO_3$ (see Fig.8) [Unveren2004, Niemeyer2002], in good agreement with *ab initio* calculations for free Cr^{3+} ion [Ilton2003]. It is interesting to note that the height ratio between the two low-BE components (576.8 and 577.6 eV) is reversed with respect to what measured for pure Cr_2O_3 and for lightly Ti-doped $Cr_{2-x}O_3$ samples [Chambers2001, Niemeyer2002]. This appears to be related with the presence of Ti atoms, as also noticeable in the work of Niemeyer et al. for the $Cr_{2-x}Ti_xO_3$ samples with the highest Ti concentration.

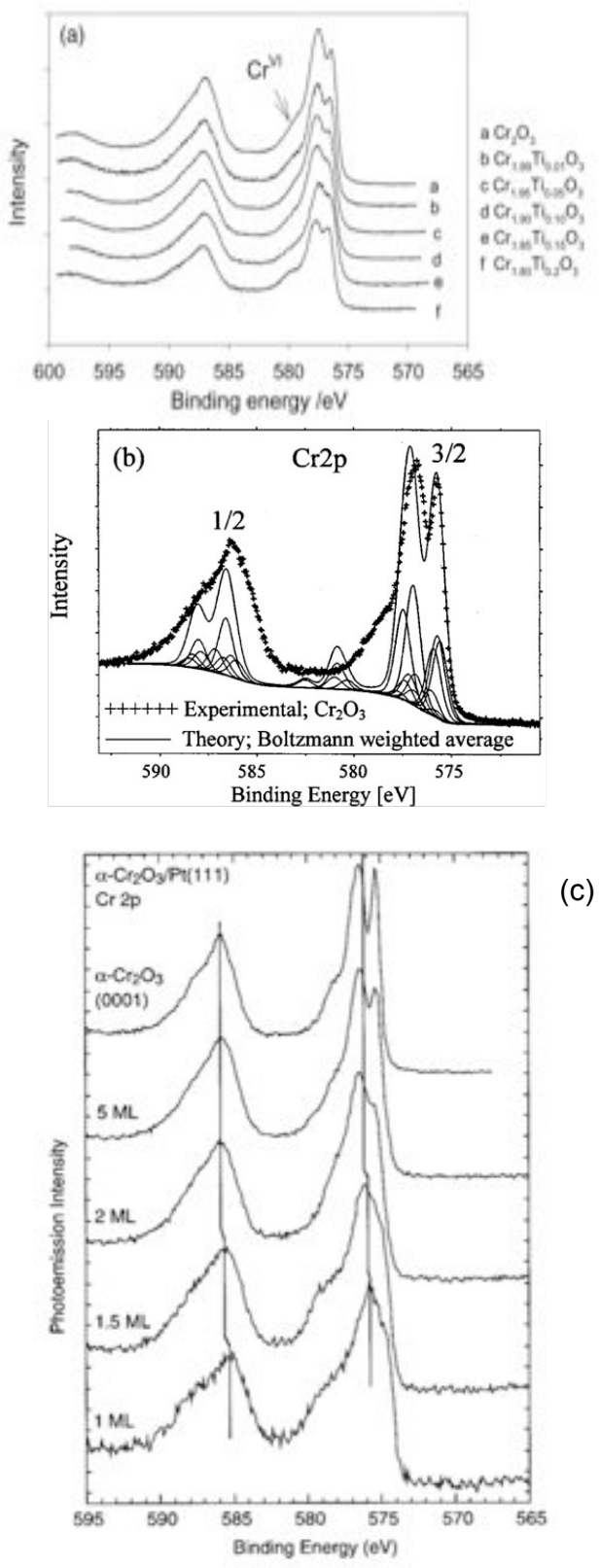

Figure 8 – Cr 2p XPS spectra taken on (a) $Ti_xCr_{2-x}O_3$ (0<x<0.2) [Niemeyer2002], (b) Cr_2O_3 along with theoretical calculations for free Cr^{3+} ion [Ilton2003] and (c) Cr_2O_3 thin films with different thickness [Chambers2001]

This result suggests that the Cr atoms are efficiently injected inside these systems and they appear to be also thermodynamically very stable upon a wide growth-temperature range, as confirmed by the almost identical lineshape found in the 350°C, 550° and 800°C samples.

On the contrary, the results obtained for pure anatase specimens are more variegated, with only the 800°C film presenting a lineshape similar to what observed for SCBD (see Chap.4) and mixed-phase samples (Fig.7).

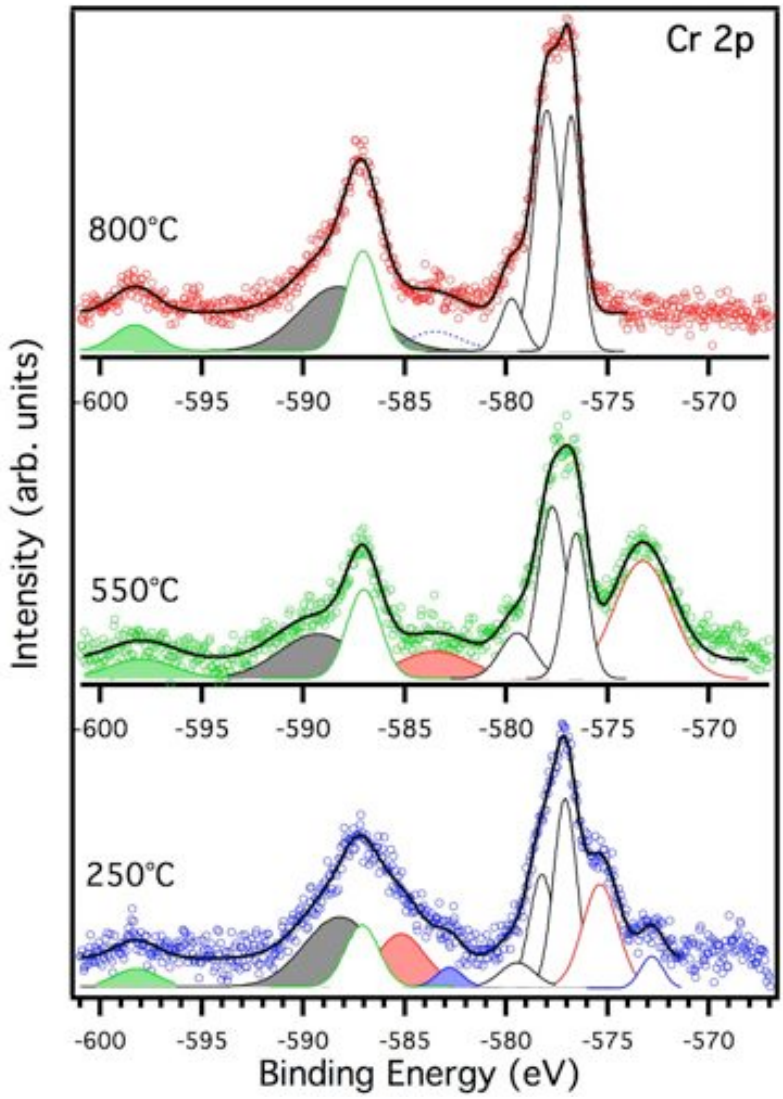

Figure 9 – Cr 2p XPS spectra taken on pure anatase Cr-N-TiO_2 grown at 250°, 550° and 800°C along with fit results. See text for more details.

Both the 550°C and the 350°C films exhibit a much broader Cr $2p_{3/2}$ component centered around 577.5 eV BE. The first also presents a separate peak at 573.5 eV, while the second has also a quite intense shoulder around 575 eV, none of which is observed in the other samples (Fig.7). Among all the features present in these two spectra, the low-BE peaks may give some hints about the chemical composition of the samples. In fact, the BE of the 573.5 eV peak in the 550°C sample is compatible with the presence of metallic Cr inside the film [Shuttleworth1980], probably in the form of small cluster dispersed inside the TiO_2 matrix. The lineshape and the energy position of the remaining peaks indicate that the Cr atoms are also partially bonded to Ti and O species, forming the expected Cr^{3+} ions. Nonetheless, it appears that the deposition temperature does not allow a complete dilution of the Cr dopants inside the film. A similar result is found in the 250°C sample too, where the overall lineshape of the $2p_{3/2}$ peak does not present the strong multiplet splitting typical of Cr oxides. This peak appears only slightly asymmetric, with a significant shoulder on the lower BE side. The complex structure of this particular spectrum suggests that several compounds can nucleate when the growth temperature is this low (i.e. metallic Cr, Cr-O, Cr-Ti or even Cr-N complexes).

Following the procedure outlined in Chap. 4, we also analyze the Cr 3s spectra in order to gain information about the valence configuration of the Cr ions. Our data are consistent with the Cr 2p results. In fact, the presence of chromium is evident in the six samples considered (see Fig. 10). After subtracting the contribution coming from the Ti 3s peak, we can isolate the pure Cr 3s signal and evaluate the exchange splitting due to unpaired electrons in the Cr valence band, as described in details in Chap. 4.

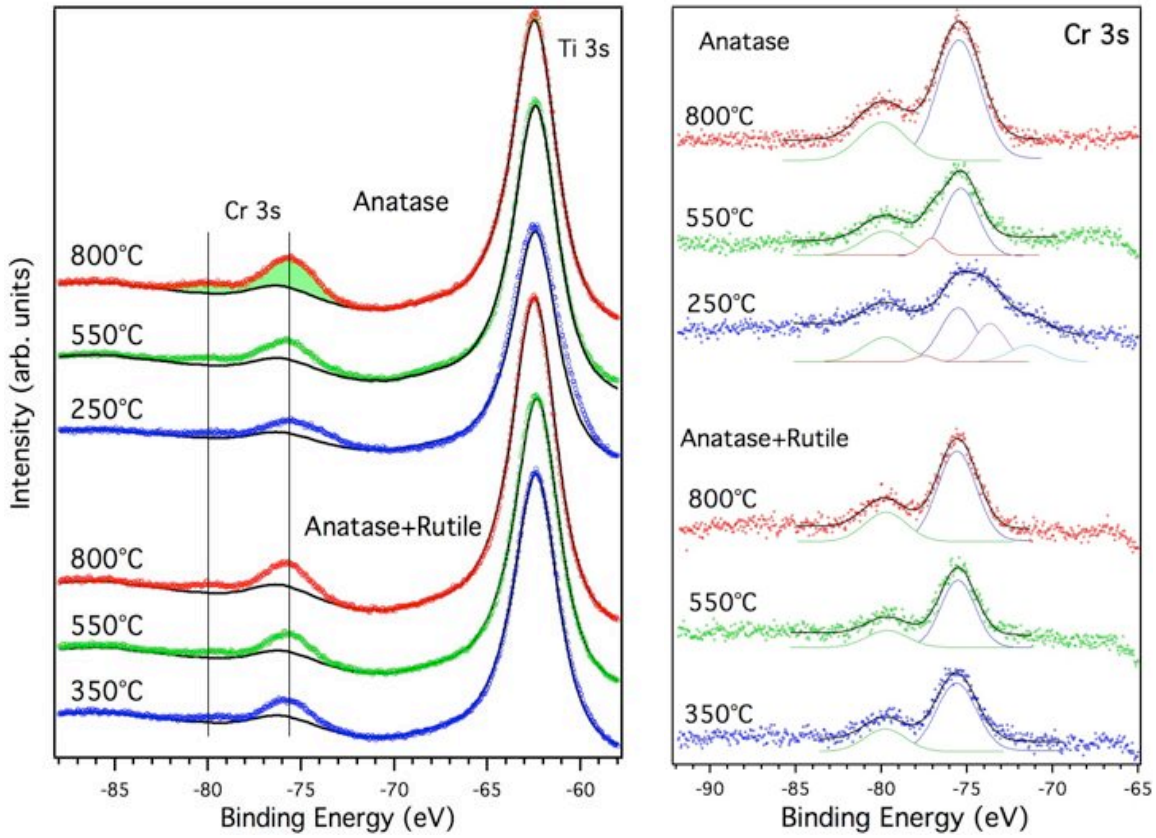

Figure 10 – Cr 3s photoemission spectra taken on Cr-N TiO_2 samples grown at different temperatures and having different crystal structures (anatase and mixed anatase-rutile) along with a reference spectrum taken on a similar undoped TiO_2 sample.

The anatase-rutile samples possess an almost identical lineshape (right side of Fig.10), with two separated peaks attributed to the spin up and spin down 3s photoelectrons differently affected by the interaction with the total spin S of the valence 3d electrons during the photoemission process. The two components are found at 75.5 eV and 79.8 eV BE, separated by 4.3 eV. This separation indicates that the Cr ions are in a 3+ configuration [Zimmermann1998], confirming that these atoms are substitutionally embedded in the TiO_2 structure. On the other hand, No major variations are observed as a function of the growth temperature, as also noted for the Cr 2p photoemission spectra of these three samples.

On the other hand, the pure anatase films exhibit a strong evolution as a function of the growth temperature. The 800°C film is the only one possessing a lineshape similar to what observed for the mixed phase films, with two distinct components

centered at 75.3 eV and 79.6 eV BE (separation ~4.3 eV). The 550°C sample shows an additional component at 77.1 eV BE (separation ~1.8 eV) that indicates the nucleation of a different chromium phase. It is important to remember that also the Cr 2p spectrum taken on the same film shows an additional peak that we tentatively ascribed to metallic Cr (see Fig. 9). In the same way, this additional component at 77.1 eV is compatible with metal-like Cr droplets not diluted in the TiO_2 lattice. In fact, elemental chromium has unpaired electrons in the VB as well, originating multiplet splitting in the 3s photoemission spectra [VancAmpen1991]. Moreover, the energy difference between the two components in metallic Cr is reported to be around 2 eV [Klebanoff1986], less than what observed for any Cr^{3+} compound (~4.2 eV [Zimmermann1998]). Our estimation for the "metal-like" component's splitting is 1.8 eV so in good agreement with the value found for solid Cr samples.

The most complex spectrum is found for the 250°C film (blue spectrum in the upper part of Fig. 10), confirming what found in Cr 2p XPS spectrum. Our best fit involves five different components, clearly indicating that the growth temperature is too low to allow an efficient Cr dilution inside the TiO_2 matrix. Thus, several chromium compounds appear to be present in our film.

Therefore, we can safely conclude that pure anatase samples deposited at temperatures below 600°C do not grant a good Cr dispersion inside the TiO_2 matrix nor a precise control over the phases present inside the films. On the other hand, the rutile-anatase films appear to be more sable from this point of view, granting an efficient Cr dispersion inside the titania lattice almost independent from the growth temperature.

Our characterization involves also the analysis of N 1s spectra, in order to investigate the behavior of these dopants as a function of growth temperature and crystalline structure. From the N 1s spectra (right side of Fig.6), nitrogen impurities appear to be more easily embedded in mixed rutile-anatase TiO_2, while pure anatase TiO_2 is capable of incorporating these dopants only when synthesized at high temperature (i.e. beyond 600°C). In fact, the spectra taken on the three mixed-phase TiO_2 films clearly exhibit a peak at 396 eV BE, indicating that the N atoms are present at substitutional sites inside the TiO_2 lattice. The only noticeable difference

(except for intensity variations) is the peak found at 402 eV BE in the 800°C sample and barely visible in the 550°C film. The origin of this component is somewhat unclear, even if it has been reported before and attributed to C-N interactions [Bertoti2002b], atomic N in N_2^+-bombarded Al_2O_3 [Barranco2001] and interstitial N_2 in CrN and $Ti_xAl_{1-x}N$ heated in O_2 atmosphere [Esaka1997, Esaka1999]. In our measurements, this peak appears only in the mixed anatase-rutile samples and its intensity seems to be dependent on the growth temperature. As reported by Esaka et al. [Esaka1999], N_2 formation in oxidized TM nitrides is favored by the contemporary presence of two distinct phases. In fact, the nitrogen atoms trapped between two different phases are thermodynamically unstable and can easily form N_2 molecules when the temperature rises (beyond 500°C, in our case). Thus, we tentatively ascribe this spectral feature to N_2 molecules forming at the grain boundaries during the film synthesis.

On the other hand, the core level spectra taken on the anatase TiO_2 grown below 600°C only exhibit a small bump centered around 399 eV that can be related to interstitial N, as discussed in details in the previous chapters. An identical feature also appears in pure, undoped TiO_2 (black spectrum in Fig.6b). Thus, we attribute this feature to residual molecular N originating from the exposition to air pressure after the samples' preparation. On the contrary, the XPS data collected on the 800°C anatase film confirm a much larger concentration of N atoms in the film. The N 1s spectrum is constituted by a broad peak, resulting from (at least) two different components centered around 396 and 398 eV BE. The first is due to nitrogen dopants substituting oxygen atoms inside the titania lattice. The attribution of the second component is still controversial: it has been reported for both Cr-rich nitrides [Bertoti2002a, Emery1999], and titanium nitrides [Esaka1997], but a final statement about its origin cannot be made, at this point. Through the analysis of the integral intensities of the N 1s and the Cr 2p peaks, we can estimate the concentration of the dopants inside the films. For this purpose, only the components corresponding to atoms substitutionally embedded in the TiO_2 lattice are considered (i.e. the 396 eV BE component for N 1s, and the 577 eV BE structure for Cr $2p_{3/2}$ spectra). Our results are presented in table A.

The core level analysis suggests that both Cr and N impurities are more easily injected in the 800 °C anatase sample or in the mixed-phase. The Cr atoms, once successfully doped in substitutional sites, exhibit an uniform concentration, almost independent of the crystal structure. The N atoms appear to be much more affected by the surrounding crystallinity of the TiO_2 matrix, being more easily embedded in single-phase TiO_2 films. In pure anatase samples, N atoms are found only when the deposition temperature allows a well-ordered phase (left column in table B). Interestingly, also the Cr concentration increases when N is substitutionally incorporated in the film as well. This aspect suggests that the contemporary presence of both dopants enhances the solubility of the two species, in agreement to what predicted by Zhu et al [Zhu2009].

In mixed rutile-anatase films, the highest N concentration is found for low-T° samples, when the only crystal phase present is rutile (as indicated by XRD results shown in chap. 5.1.2, Fig. 4), while this concentration decreases when both anatase and rutile are present at the same time (800°C sample).

Pure anatase				**Anatase-rutile**			
Growth T°	N %	Cr %	N/Cr	Growth T°	N %	Cr %	N/Cr
250° C	absent	3.2 %	-	350° C	2.8 %	4.8 %	0.6
550° C	absent	3.5 %	-	550° C	3.1 %	4.9 %	0.64
800° C	3.5 % (6.5 %*)	5.5 %	0.65 (1.18)	800° C	1.3 %	5.5 %	0.24

Table B – Concentration of N and Cr dopants inside the different samples as estimated from XPS analysis. *This value is obtained considering the 398 eV and the 396 eV BE components.

Another important aspect is the N/Cr ratio, since it can reveal whether the N and Cr atoms are forming n-p doping pairs, as predicted by Zhu et al. in their calculations (see the introduction to Chap. 4 for details)[Zhu2009]. In this case one would expect a N/Cr ratio close to 1. Looking at the values reported in Table B it appears that there is a discrepancy between our estimated values and the theoretical prediction.

Nonetheless, one should consider that these samples where measured *ex situ*, after an additional thermal treatment up to 500°C that could have caused variation in the as-deposited dopants concentrations. Therefore, we can safely exclude the Cr-N pair formation just for the low-T° anatase films (no N found in the film), and for the high-T° anatase-rutile one (the estimated ratio appears to be too distant from the expected value). On the other hand, the ratios obtained for the single-phase samples (anatase 800°C, anatase-rutile 550°C) appear to be compatible at least with a partial Cr-N pair formation.

5.2 Band gap tuning

5.2.1 Band gap narrowing: optical absorption

The main goal of the Cr-N doping of TiO_2 remains the band gap narrowing for photovoltaic and photocatalytic applications. Thus, our investigation is now focused on the optical absorption capabilities of such codoped films, with respect to what found in N-only and Cr-only doped TiO_2 and also in Cr-N-TiO_2 nanoclusters. The sample analyzed hereafter are pure anatase films, grown at 700°C. This choice is consistent with the XRD and XPS results presented in the previous sections, where the anatase thin film grown at temperatures higher than 600°C granted the highest dopants‘ concentration and crystal quality.

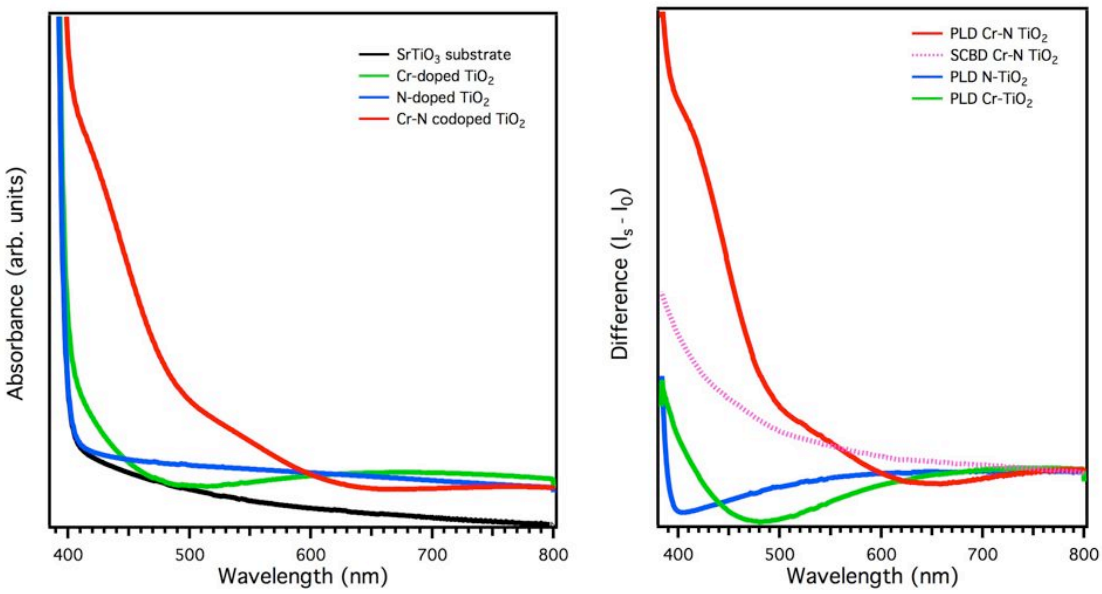

Figure 11 – (*left*) Optical absorption spectra taken on epitaxial PLD N-only, Cr-only doped and Cr-N codoped films along with a reference spectrum taken on the bare substrate ($SrTiO_3$, band gap ~ 3.5 eV [ref]). (*right*) Difference between spectra taken on the samples and the ones taken on the corresponding bare substrates [Eres2009].

The absorbance spectra taken on the bare substrate ($SrTiO_3$, black spectrum), on the N-only doped (blue), on the Cr-only doped (green) and Cr-N codoped TiO_2 (red) samples are plotted in left panel of Fig. 11. The right side of Fig. 11 shows the difference between each spectrum and the substrate's one. This subtraction is necessary in order to allow a comparison between the PLD samples and the SCBD one discussed in Chap. 4.2.2 (dotted purple spectrum). In fact, the latter was deposited on $LaAlO_3$ instead of $SrTiO_3$ and this aspect could have generated spurious contributions to the absorbance spectra.

All the spectra exhibit a sharp cut-off at 400 nm that is due to the main band-to-band absorption in TiO_2 (λ= 400 nm corresponds to an energy gap of 3.1 eV, i.e. the undoped TiO_2 band gap). The N-only doped sample does not exhibit any other feature, indicating that N-only doping does not effectively reduce the band gap with respect to undoped TiO_2. The Cr-only doped sample has a small but noticeable shift of the absorption edge to ~460 nm, corresponding to a band gap value of 2.7 eV. This result resembles the STS data presented by Zhu et al. [Zhu2009] and discussed in details in Chap. 4. However, the most striking result is the dramatic difference

found in the Cr-N codoped film. In fact, it is clear that the doping process strongly affects the optical behavior, shifting the absorption edge up to ~610 nm, that corresponds to a band gap of 2.0 eV. Two major contributions can be isolated in the latter spectrum, one, more intense, centered around 440 nm and a second one centered around 550 nm. Putting in comparison these three spectra with the SCBD sample discussed in Chap. 4.2.2 (dotted purple line in the right panel of Fig. 11), one can clearly see that both the codoped films (PLD and SCBD) exhibit a stronger absorption in the visible range, with the epitaxial film exhibiting the strongest spectral changes.

This result clearly demonstrates that the Cr-N codoping approach dramatically reduces the optical band gap in the titania epitaxial films. Moreover, from the comparison with the single doped samples, we can argue that this result is not a mere superimposition of the two doping channels. On the contrary, it is evident that a completely different mechanism is responsible for this strong reduction of the band gap. As suggested by Zhu et al., Cr-N pairs formation upon doping appears to be the most sensible explanation, even if more work is needed to definitely confirm the dopants coupling.

This result suggests that the Cr-N codoping approach can be a real breakthrough in artificially adjusting the titanium dioxide's band gap, possibly boosting the performances of any device based on this material.

In order to better analyze the mechanism responsible for such a strong band gap narrowing in the PLD Cr-N sample, a detailed analysis of both the top of the VB and the bottom of the CB is need. This is presented in the next sections.

5.2.2 Filled states: valence band photoemission

Optical absorption demonstrates that PLD Cr-N-TiO_2 possesses a remarkably smaller band gap, compared to undoped and single doped TiO_2. It is fundamental, at this point, verifying whether this narrowing is related to new filled states at the top of the VB and/or empty states at the bottom of the CB.

Therefore, our discussion involves now valence band photoemission data taken on the pure anatase and anatase-rutile samples characterized in the 5.1.2 and 5.1.3 sections with XRD and XPS. This will allow to study the possible appearance of new filled states and evaluate the role of the film's crystal structure.

The VB photoemission spectra measured on both the anatase (top) and anatase-rutile (bottom) Cr-N-TiO_2 films are presented in Fig.12 along with the analogous spectrum taken on undoped TiO_2 (black spectrum).

The mixed phase samples present a homogeneous lineshape, with the two main components related with O 2p – Ti 3d bands centered around 8 eV and 5.5 eV BE, as already seen for SCBD N-TiO_2 and Cr-N-TiO_2 (see Chap.4.2.1). Interestingly, the 800°C film exhibits a sharper distinction of the two main peaks, this is related to a higher crystal quality of the film, as also indicated by XRD results presented in Fig. 4 (see also [Caruso2007]).

The pure anatase films are subject to a more complex lineshape evolution, as already seen also in core levels photoemission data. The low-T° sample possesses a broad feature in the 9 eV – 4 eV BE region, where the two main contributions are not well resolved. Once again, this region is very sensitive to the epitaxial quality of the film, so the smearing of the VB spectrum is due to the absence of long-range order in the crystal lattice. This conclusion is in agreement with our XRD data that indicate that no extended epitaxial growth is allowed when the temperature is lower than 500°C (see Fig. 4). When the film is deposited beyond the 500°C threshold, the lineshape of the VB spectrum is more defined, with the strongest contribution centered around 7.5 eV BE and a shoulder at 5.5 eV BE. These spectra exhibit a different lineshape compared to what observed for rutile-anatase samples. This is ascribed to the purely anatase phase of these films. In fact, pure anatase TiO_2 is known to have a slightly different lineshape with a more intense peak in the high-BE region and a less intense shoulder on the low-BE side [Chambers2009], as also evident in our data taken on the undoped anatase sample (black spectrum in Fig.12). On the contrary, pure rutile TiO_2 presents two contributions with similar intensity [Diebold2003].

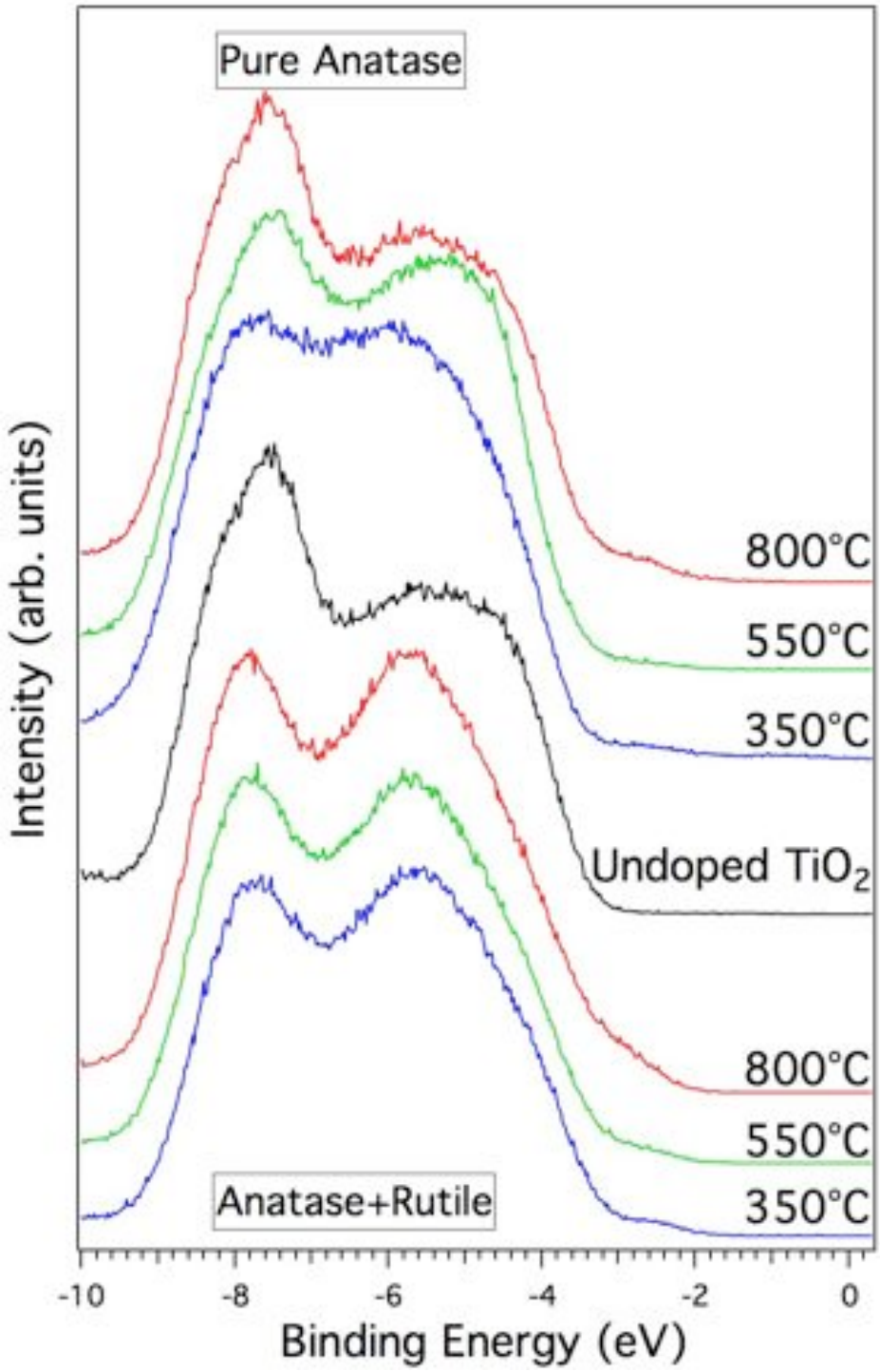

Figure 12 – VB photoemission spectra taken on Cr-N codoped TiO_2 along with a reference spectrum taken on a PLD undoped TiO_2 sample.

Besides the effects related to the crystallinity of the films, no other major differences can be detected in the O 2p – Ti 3d spectral region. On the other hand, much more

information can be gained by looking at the 6 eV BE – Fermi level region, depicted in Fig. 13. Here a magnification of the top of the VB for the pure anatase (top panel) and the anatase-rutile (bottom) samples is presented along with the reference taken on the undoped TiO_2 film. The pure anatase film grown at 800°C presents a quite intense shoulder extending up to 1.8 eV BE, thus shifting the VB cut-off of more than 1.3 eV. Moreover, the low-BE part of the large O 2p – Ti 3d band seems to be more intense than what measured for single doped and undoped TiO_2. The component found around 2.6 eV BE is compatible with what observed for SCBD Cr-N TiO_2 nanoclusters (see Chap. 4.2.1), that we attributed to Cr 3d states, as also done in literature [Osterwalder2005, Nolan2009].

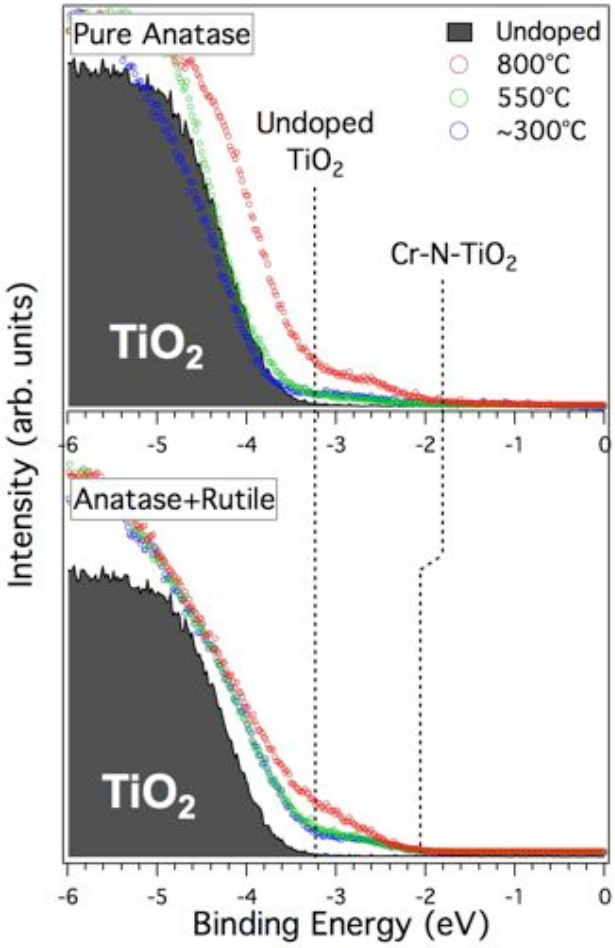

Figure 13 – VB photoemission spectrum taken on the Cr-N doped TiO_2 samples along with a reference spectrum taken on a PLD undoped TiO_2 film. A shift of the VB's cut-off of more than 1.2 eV is evident.

Comparing these results with what measured for N-doped TiO_2 and Cr-doped TiO_2 it appears that N 2p states can contribute to the increased intensity of the O – Ti band in the 3.3 – 4.4 eV BE region [BatzillPRL2006]. Based on these results is not clear whether N 2p and Cr 3d levels can be partially hybridized forming an impurity "band" as predicted by Zhu et al. in their calculation [Zhu2009]. Nonetheless, we can conclude that both the dopants significantly contribute to narrow the titania band gap, shifting the top of the VB of more than 1.3 eV. The anatase samples grown below 600°C do not show such an evident band shrinkage, presenting only a low-intensity tail at the very top of the VB. The O – Ti band does not appear to be affected by the codoping, and this confirms that a shift of this band's cut-off is, at least indirectly, related with N 2p states, as measured for the 800°C sample. Thus, the absence of any substitutional N inside the low-T° films, as shown in Tab. B, leaves the O – Ti band's edge aligned to the undoped sample's value, as evident in the top panel of Fig. 13.

VB spectra acquired on anatase-rutile films grown below 600°C are essentially identical, both exhibiting a component at ~2.6 eV BE. This result can be explained in terms of the N 2p and Cr 3d states, as discussed for pure anatase films, even if the VB's cut-off is now ~2.1 eV BE instead of the 1.8 eV found for the pure anatase films. This difference can be related with the different crystal structures present in the films. Nonetheless, the behavior is usually reversed with respect to what is being observed here, with rutile structure exhibiting the lowest band gap value (3.0 eV) and the anatase the highest (3.2 eV) [Diebold2003].

It is important to bear in mind that the dopants' concentration in these two samples is very similar (Table B), as are the corresponding VB spectra. This gives a further confirmation that the top of the VB is dominated by the N 2p and Cr 3d impurity levels. The anatase-rutile sample grown at 800°C shows a remarkably higher intensity of the impurity levels, that appear also to be slightly shifted towards higher BEs. Our data do not allow quantitatively evaluation of this shift, but one should consider that the 800°C sample is the only sample truly composed by both rutile and anatase phases, as clearly indicated by XRD (see Fig. 4 and the following footnote).

Thus, we tentatively interpret the different lineshape of the anatase-rutile grown at 800°C as originating from the superposition of impurity states in a rutile and in an anatase configuration. The intensity of such components appears to be higher than what measured on the films grown at lower temperatures. This cannot be entirely explained with the slightly higher Cr concentration in the 800°C sample (Table B). In fact, N concentration is remarkably smaller compared to the lower T° samples.
On the other hand, a possible contribution can arise from the tail of the low-BE peak of the O 2p – Ti 3d band, that is significantly more intense in anatase-rutile than in pure anatase samples (see Fig 12). This aspect cannot be completely explained only on the basis of this photoemission characterization, but it seems reasonable that also the peculiar mixed crystal phase of the 800°C film could play a role.

5.2.3 Empty states: X-ray absorption spectroscopy

In the previous two sections, we presented strong evidence that new electronic states appear inside the TiO_2 band gap due to the Cr-N codoping. We identified some of them as positioned right at the top of the VB and extending more than 1.2 eV inside the gap.
In this section, we will discuss the possible appearance of empty electronic states in the CB, analyzing NEXAFS data taken on some of the PLD Cr-N codoped samples.
The NEXAFS results presented hereafter were obtained on PLD samples grown at high temperature (i.e. T ~800°C, red spectra) and low temperature (T ~350°C, blue spectra) for both the pure anatase and the mixed anatase-rutile sets described in Chap. 5.1.2. The analogous NEXAFS spectra discussed in details in Chap. 4 and 3 for the SCBD samples (N-doped and Cr-N-doped, light blue and green spectra) and the undoped TiO_2 samples (black) are presented as a reference.
Ti L-edge absorption spectra taken on the mixed phase codoped samples (bottom part of Fig.14) do not show any appreciable variation as a function of the deposition temperature. The overall lineshape resembles what already found for both undoped PLD samples and doped SCBD samples (see Chap. 4.1.3 and 3.4.3). The t_{2g} and e_g

peaks are well resolved in both the L_3 and L_2 edges. These spectral features are narrower than what measured in the SCBD films, because of the less defected structure of the PLD samples compared to the SCBD one. No other features can be isolated in pre-edge region, with respect to what found for undoped TiO_2 (black spectra), and this suggests that the Ti LUMOs are essentially not affected by the Cr-N codoping.

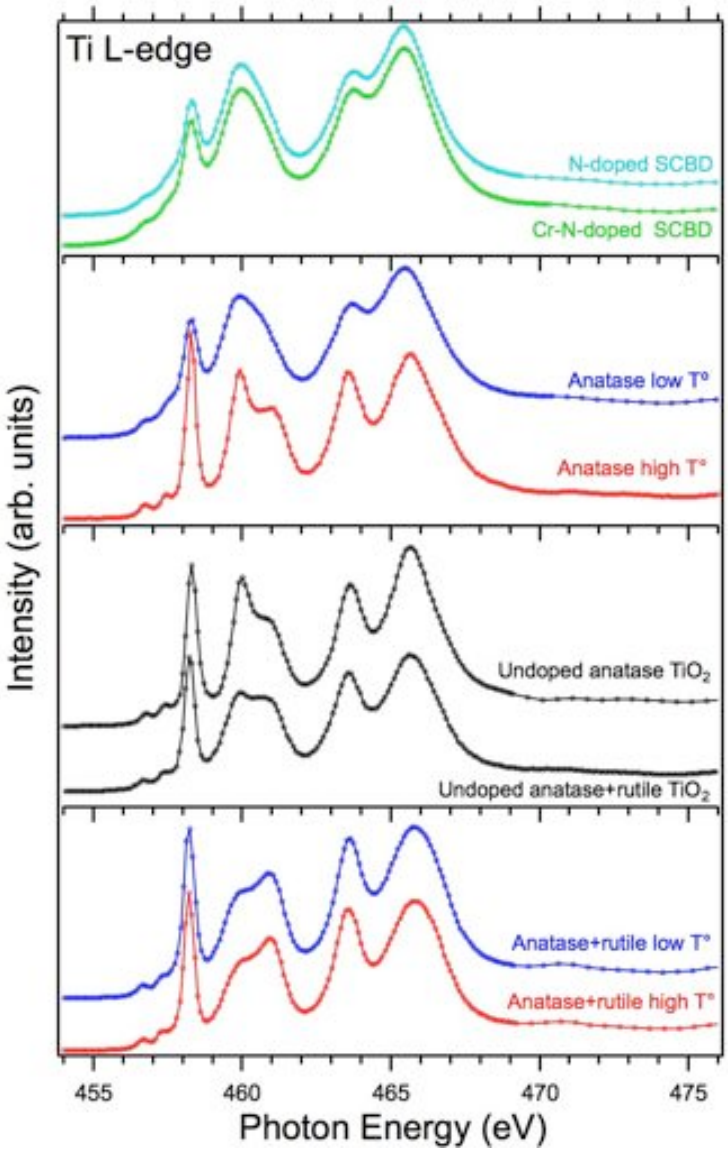

Figure 14 – Ti L-edge (left panel) and O K-edge (right panel) NEXAFS spectra taken on the PLD Cr-N codoped samples. Both the pure anatase and the mixed anatase-rutile samples are displayed (blue spectra when deposited at low temperature, red spectra when deposited at high temperature). The corresponding data taken on SCBD samples (green and light blue) and undoped TiO_2 (black spectra) are also presented as a reference.

The only noticeable difference between the Cr-N anatase-rutile and the undoped TiO_2 data is an inversion in the intensity ratio between the two e_g components in the 459-462 eV range. This spectral region is very sensitive to the long-range order of the film, and it strongly depends on the crystalline phase as well [Kucheyev2004]. Thus, we attributed this difference to a slight variation in the anatase-to-rutile percentage inside the Cr-N doped samples with respect to the mixed-phase undoped samples.

On the other hand, the pure anatase samples exhibit a quite strong variation going from a low-T° to a high-T° deposition (blue and red spectra in the upper part of Fig.14). While the high-T° spectrum perfectly resembles the undoped anatase TiO_2 data, the low-T° film lineshape is closer to what was found for the SCBD samples rather than for the other anatase films. This difference is compatible with the XRD results presented earlier (Chap. 5.1.2), in which no extended crystalline growth is evident for anatase samples grown at temperatures lower than 400°C. These results confirm that Ti L-edge is strongly affected by the crystalline order, thus giving a very similar result for a cluster-assembled film and a nearly amorphous PLD film. On the contrary, the high-T° anatase film is well ordered, with a single crystalline phase present, and that the Ti lattice do not show any variation due to the contemporary presence of the Cr and the N dopants.

A similarity between the SCBD films and the low-T° anatase sample is also evident in the O K-edge absorption spectra presented in Fig. 15 (blue spectrum). In fact, the two samples exhibit a nearly identical lineshape, with a noticeable broadening of the t_{2g} and the e_g features in the 530-535 eV range, with respect to the other samples.

The codoped anatase PLD film grown at high temperature exhibits a quite different NEXAFS spectrum, with two well resolved peaks at 531.5 (t_{2g}) and 534 eV (e_g) along with the two O 2p – Ti 4sp features found at 539 and 544 eV. The most evident difference with respect to the other samples considered is a much more intense t_{2g} component. Once again, this part of the O K-edge spectrum is very sensitive to the long-range order of the crystal structure and strong variations of the t_{2g}/e_g intensity

ratio have been recently reported even for different surfaces of anatase single crystals [Thomas2007]. Thus, we can safely interpret this result as originating from an extended, well ordered anatase crystalline phase marking this PLD film grown at high temperature.

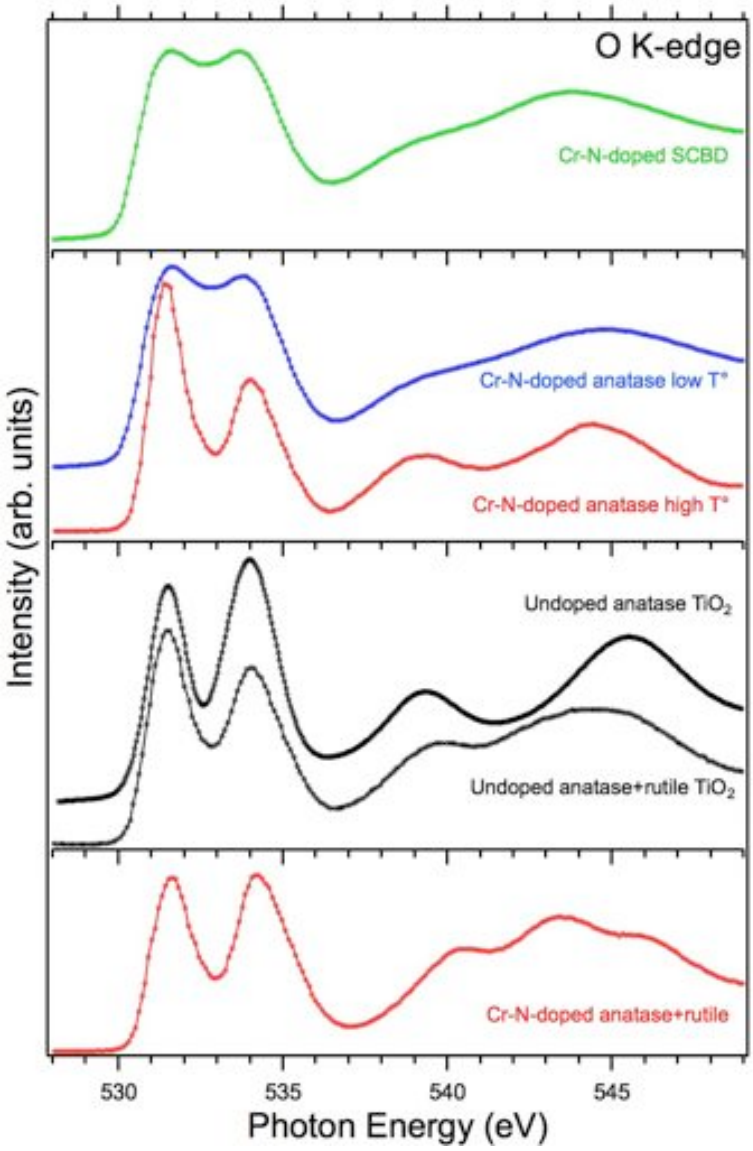

Figure 15 – O K-edge NEXAFS spectra taken on the same samples described in Fig. 14

As also previously found for Ti L-edge, our O K-edge NEXAFS data indicate that no differences can be detected among the mixed-phase PLD films grown at low and high temperatures. Thus, we only report the high-T° deposited film in the bottom part of Fig.15, as representative of both specimens. The spectrum resembles what

measured on the corresponding undoped sample, only with an increased intensity of the e_g feature and a better overall resolution of the high-energy region (538-548 eV). As discussed before for Ti L-edge, these features are attributed to small differences in the crystal lattice of the codoped and the undoped PLD films, rather than originating from the Cr-N doping.

So far, the Ti and O NEXAFS data show no strong effects of the Cr-N codoping on the Ti- and O-derived LUMOs. As we pointed out before, these two absorption spectra are very sensitive to the long-range order of the titania lattice. Therefore, this is a further confirmation that the Cr-N codoping does not affect the overall quality of the deposited films.

To gain more information on possible impurity bands appearing in the CB due to the dopants, also the N K-edge and the Cr L-edge absorption spectra were measured. Moreover, these NEXAFS data could help to possibly clarify whether the Cr and N species are coupled forming pairs, as predicted by Zhu et al. [ZhuPRL2009].

The NEXAFS results taken at the nitrogen absorption edge are presented in Fig.16. It is evident that neither the pure anatase nor the anatase-rutile PLD samples exhibit a lineshape similar to what found for the N-doped and Cr-N codoped SCBD films. The pure anatase film grown at low T° (blue spectrum, central panel) confirms what already concluded after XPS characterization: no N is injected inside the film when synthesis takes place below 400°C. In fact, the absorption spectrum is compatible to what measure on undoped TiO_2 (black spectrum), where the very small signal detected can be attributed to residual nitrogen remained on the surface due to prior air exposure. On the contrary, the anatase film deposited at high T° exhibits two quite broad features around 398 eV and 408 eV. Unfortunately, this spectrum has been recorded on a different experimental setup (i.e. a different beamline) possessing a lower resolution. This fact hampers a direct and reliable comparison between this measurement and the other spectra presented in Fig. 16. Nonetheless, it is interesting to note that this particular sample exhibited a very broad N 1s core level spectrum as well (see Fig.6). This broadening could be related with a strong delocalization of the N orbitals, possibly originating from the Cr-N codoping.

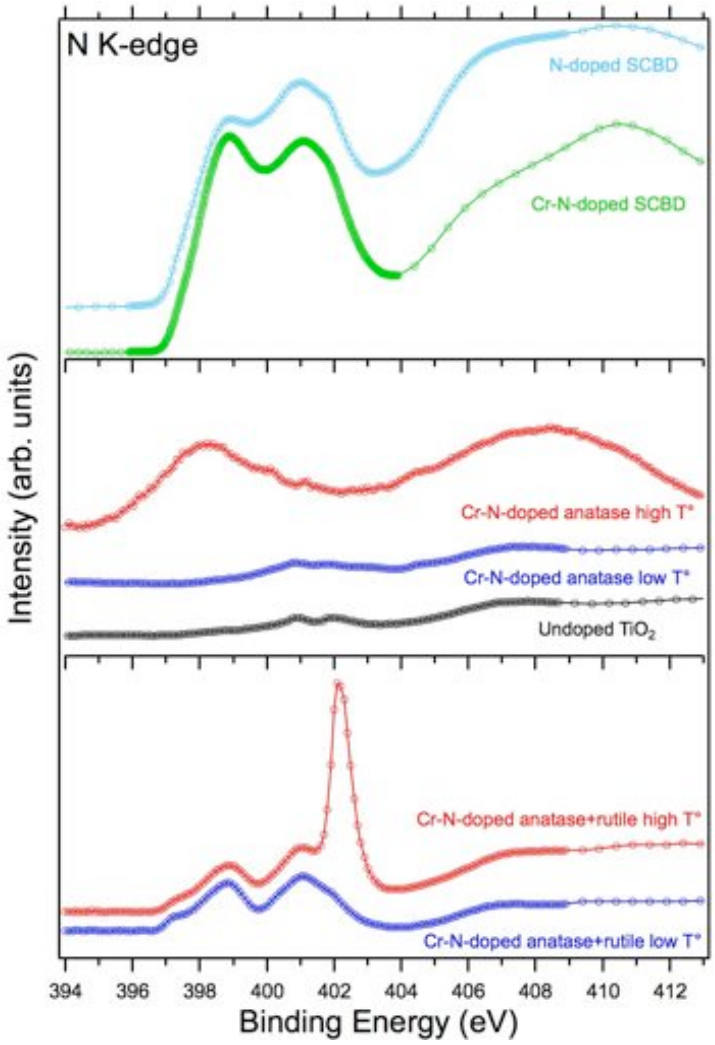

Figure 16 – N K-edge NEXAFS spectra

The N K-edge spectra taken on the anatase-rutile samples (Fig.16 bottom) share a common lineshape, except for the addition of a narrow and quite intense peak in the high T° case (~402.5 eV). The rest of the spectrum is still showing the typical splitting caused by the crystal field, with two main features centered ~399 and 401 eV. The high-energy features are attributed to N 2p – Ti 4s sub-bands and they appear to be much broader than what found in the SCBD cases. The 402 eV component present in the high T° spectrum has been found in several oxidized TMs nitrides such as TiN, CrN and $Ti_xAl_{1-x}N$ [Esaka1997, Esaka1996 and Esaka1999] and it is attributed to N_2 formed at the grain boundaries in films containing different phases. This result confirms our previous attribution based on the XPS data, where a

new peak in the N 1s spectrum was found for anatase-rutile samples grown beyond 500°C (see Chap. 5.1.3).

The low N concentration inside these films results in a very weak absorption signal that hampers an accurate analysis of the NEXAFS spectra. Therefore, we can not distinguish, based on these data, whether the N species are predominantly coupled to Cr atoms or rather diluted uniformly throughout the TiO_2 lattice. Nonetheless, it is interesting to compare our results with N and O K-edges measured with NEXAFS and Electron Energy Loss Spectroscopy (EELS) on different chromium nitrides (Fig. 17).

Excluding the molecular N peak at ~402 eV in the high T° specimen, the mixed-phase NEXAFS spectra are comparable to what has been measured for CrO_xN_{1-x} (Fig.17a), especially in the x=0.5 case (solid bold line). In fact, this particular spectrum presents two well resolved components separated by roughly 2 eV, compatible with the two main structures found at 399 and 401 eV. Moreover, it appears that the two lineshapes share at least a common trend, compatible with the presence of a (partial) Cr-N coupling.

On the other hand, our NEXAFS spectrum acquired on the high T° anatase film is very similar to the CrO_xN_{1-x} case (with x=0.1, x-markers spectrum in Fig.17a) and also with a pure CrN specimen (Fig.17c). All these three N K-edge spectra present only one broad component in the low-energy region, with a barely noticeable shoulder on the high-energy side of the peak. This component is separated by roughly 11 eV from another broad feature in the high-energy side of the spectrum. Even if these similarities are not conclusive due to the low resolution of our measurements, it is evident that such results are compatible with a somewhat extended Cr-N coupling taking place inside the anatase PLD film, as predicted by Zhu et al. [ZhuPRL2009].

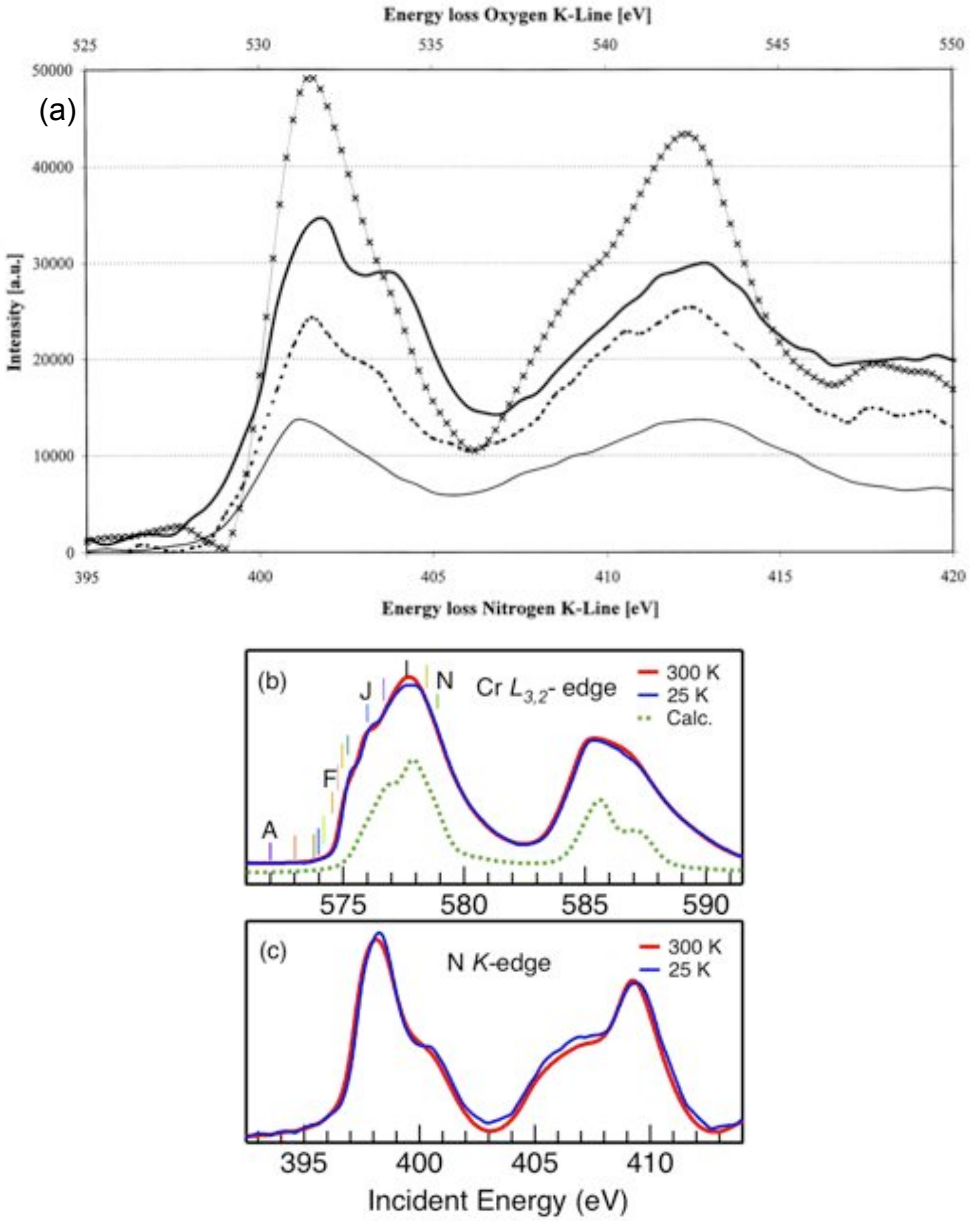

Figure 17 – (a) Background corrected and deconvoluted EELS spectra of N and O K-edge in CrO_xN_{1-x} films. Line with **x** markers represents the spectrum for the nitrogen K-edge in the $CrO_{0.1}N_{0.9}$ film. Solid bold line – nitrogen K-edge, and dashed bold line -- oxygen K-edge of the $CrO_{0.5}N_{0.5}$ film. Solid thin line – oxygen K-edge in Cr_2O_3 [Wilhartitz2004]. (b) Cr L-edge and (c) N K-edge NEXAFS of pure CrN grown at 25°K (blue) and RT (red) along with calculated Cr L-edge spectrum (dotted green spectrum in b) [Bhobe2010]

If the Cr-N pairs formation is the dominant mechanism driving the dopants injection in these films, one would expect to measure a somewhat different behavior also in the Cr L-edge absorption spectra. More precisely, the lineshape should deviate (at least partially) from the standard Cr(III) case due to the additional Cr-N interaction,

ideally matching the chromium nitride (CrN) absorption spectrum. Our Cr NEXAFS data confirm this idea, as can be seen comparing Fig. 17b with Fig. 18. In the latter the L-edge absorption spectra taken on the high and low T° mixed-phase samples, the Cr-N-doped SCBD (see Chap. 4.1.3 for a detailed description) and the low T° anatase film results are presented. Unfortunately, some issues during the NEXAFS experiments prevented to acquire the Cr L-edge spectrum on the high T° anatase sample.

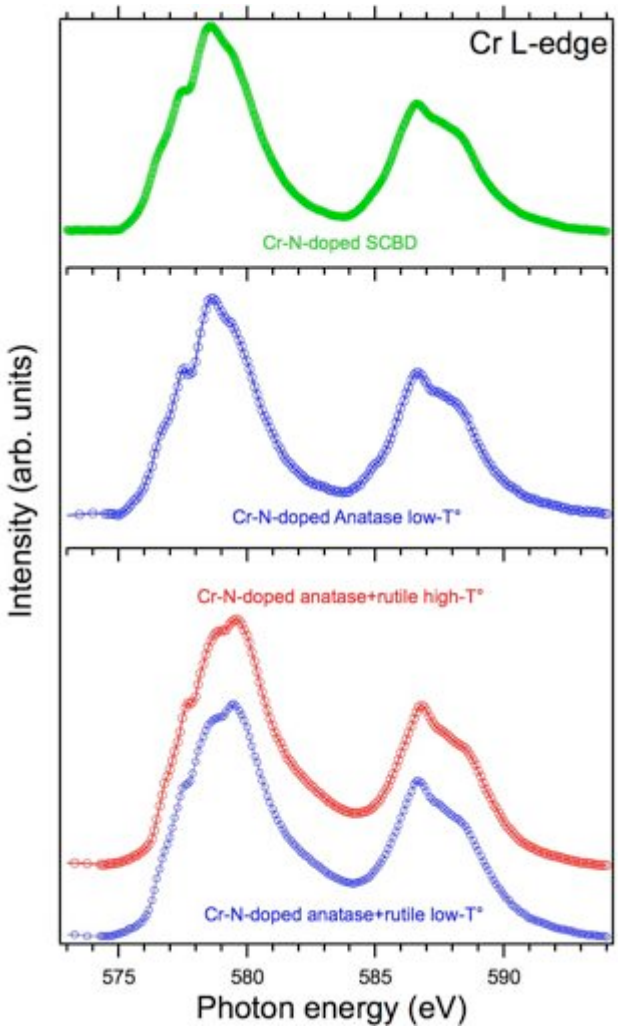

Figure 18 – NEXAFS spectra taken on the Cr L-edge for Cr-N codoped SCBD sample (top panel), pure anatase (central) and anatase-rutile (bottom panel) samples

Low T° anatase (not containing any substitutional nitrogen) and the SCBD data are essentially identical to what measured on other chromium (III) oxides (see Chap.

4.1.3). On the contrary, the lineshape found in the anatase-rutile codoped films is remarkably different, especially in the L_3 region (575-582 eV). In fact, it appears that in the SCBD and in the low T° anatase spectrum the most intense component is centered around 578.5 eV. On the other hand, in both the anatase-rutile samples this feature is only found as a shoulder, and the most intense component is now found around 1 eV higher in energy (580 eV). This results in a noticeable lineshape variation, that becomes very informative when putting in comparison these spectra with the reference taken on pure chromium nitride (CrN) showed in Fig.17b. In fact the two lineshapes are very similar, suggesting that a major fraction of the Cr present inside the codoped films is in direct interaction with N atoms, with a CrN-like coordination.

This is a strong confirmation that Cr-N pairs are forming inside the film, and it may also explain the remarkably stronger optical response of the codoped films with respect to the Cr-only and N-only doped samples (see Chap. 5.2.1). In fact, the formation of the Cr-N pairs may be responsible of inducing major variations in the TiO_2 band gap, reducing its value much beyond what obtained by a superposition of Cr- and N- single doping. This is also in agreement with our VB photoemission and optical absorption data.

5.2.3 Conclusions

Cr-N doped TiO_2 films grown by means of PLD are highly epitaxial, as demonstrated by XRD analysis. The subsequent XPS and NEXAFS analysis suggest that the injection of both the dopants is strongly dependent upon the deposition conditions. In fact, the N atoms are not found in the anatase samples synthesized at low temperatures (i.e. below 600°C). On the contrary, the rutile-anatase mixed phase samples are able to retain both the dopants more easily. Strong variations in the occupied states at the top of the VB are found for the codoped samples with respect to what measured for the undoped TiO_2; especially when the dopants are efficiently injected inside the titania matrix (i.e. at high temperatures). These variations in the

electronic states strongly reduce the band gap of the thin film, as also confirmed by optical absorption measurements. The optical results indicate that such reduction is much stronger in the Cr-N codoped sample than what measured for N- and Cr-only doped TiO_2. This finding suggests that our result is more than a simple superposition of the two single-doped effects. One possible explanation is the creation of Cr-N pairs upon doping, as suggested by Zhu et al. [Zhu2009]. This explanation is also compatible with our NEXAFS results. Nonetheless, more work is needed to fully characterize the transport performances of such thin films and to establish whether the Cr-N coupling is the main responsible for the high photo-activity found in our PLD samples.

References

[Messiah] Messiah A., *Quantum mechanics*, Dover ed. (1999).

[Rao1998] Rao C.N.R. and Raveau B., *Transition Metal Oxides* 2nd edn (1998).

[Warusawithana2003] Warusawithana M.P., Colla E.V., Eckstein J.N. and Weissman M.B., *Phys. Rev. Lett.* **90**, 1586 (2003).

[Lee2005] Lee H.N. et al., *Nature* **433**, 395 (2005).

[Willmott2004] Willmott P.R., *Prog. Surf. Sci.* **76**, 163 (2004).

[Christen2008] Christen H.M. and Eres G., *J. Phys.: Condens. Matter.* **20**, 264005 (2008).

[Ohnishi2005] Ohnishi T. et al., *Appl. Phys. Lett.* **87**, 241919 (2005).

[Eres2002] Eres G. et al., *Appl. Phys. Lett.* **80**, 3379 (2002).

[Shen2004] Shen J., Gai Z., Kirschner J., *Surf. Sci. Rep.* **52**, 163 (2004).

[Toro2010] Toro R.G. et al., *Chem. Vap. Deposition* **16**, 143 (2010).

[Ohsawa2009] Ohsawa T., Lyubinetsky I., Du Y., Henderson M.A., Shutthanandan V. and Chambers S.A., *Phys. Rev. B* **79**, 085401 (2009).

[Chen2007] Chen X. and Mao S.S, *Chem. Rev.* **107**, 2891 (2007).

[Kholmanov2003] Kholmanov I.N. et al, *Nanotechnology* **14**, 1168 (2003).

[Gall2002] Gall D. et al., *J. Appl. Phys.* **91**, 3589 (2002).

[Fisher2006] Fisher P. et al., *Microelectronics Journal* **37**, 1493 (2006).

[Dachille1968] Dachille F. el al., *Am. Mineral.* **53**, 1929 (1968).

[SaLi2009] Sa Li and Jena P., *Phys. Rev. B* **79**, 201204(R) (2009).

[Unveren2004] Unveren E. et al., *Surf. Interface Anal.* **36**, 92 (2004).

[Chambers2001] Chambers S.A. and Droubay T., *Phys. Rev. B* **64,** 075410 (2001).

[Niemeyer2002] Niemeyer D. et al., *J. Mater. Chem.* **12**, 667 (2002).

[Gupta1975] Gupta R.P. and Sen S.K., *Phys. Rev. B* **12**, 15 (1975).

[Ilton2003] Ilton E., deJong W. and Bagus P., *Phys. Rev. B* **68**, 125106 (2003).

[Shuttleworth1980] Shuttleworth D. et al., *J. Phys. Chem.* **84**, 1629 (1980)

[Bertoti2002a] Bertoti I., Mohai M., Mayrhofer P.H. and Mitterer C., *Surf. Interface Anal.* **134**, 740 (2002).

[Bertoti2002b] Bertoti I., *Surf. Coat. Tech.* **151**, 194 (2002).

[Emery1999] Emery C., Chourasia A.R. and Yashar P., *J. Electr. Spectr. Rel. Phenom.* **104**, 91 (1999).

[Esaka1997] Esaka et al., *J. Vac. Sci. Technol. A*, **15** 2521 (1997).

[Zhu2009] Zhu W. et al., *Phys. Rev. Lett.* **103**, 226401 (2009).

[Caruso2007] Caruso T. et al., *Surf. Sci.* **601**, 2688 (2007).

[Klebanoff1986] Klebanoff L.E. and Shirley D.A., *Phys. Rev. B* **33**, 5301 (1986).

[Zimmermann1998] Zimmermann R. et al., *J. Electron Spectrosc. Relat. Phenom.* **96**, 179 (1998).

[Chambers2009] Chambers S.A., Ohsawa T., Wang C.M., Lyubinetsky I. and Jaffe J.E., *Surf. Sci.* **603**, 771 (2009).

[Diebold2003] Diebold. U., *Surf. Sci. Rep.* **48**, 53 (2003).

[Osterwalder2005] Osterwalder J. et al., *Thin Solid Films* **484**, 289 (2005).

[Nolan2009] Nolan M., Mulley J.S. and Bennett A., *Phys. Chem. Chem. Phys.* **11** 2156 (2009).

[BatzillPRL2006] Batzill M., Morales E.H. and Diebold U.; *Phys. Rev. Lett.* **96**, 026103 (2006)

[Kucheyev2004] Kucheyev S.O. et al., *Physical Review B* **69** 245102 (2004).

[Wilhartitz2004] Wilhartitz P., Dreer S. and Ramminger P., *This solid films* **447**, 289 (2004).

[Thomas2007] Thomas A.G. et al., *Phys. Rev. B* **75**, 035105 (2007).

[Bhobe2010] Bhobe P.A. et al., *unpublished data* (2010).

[Braun2010] Braun A. et al., *J. Phys. Chem. C* **114**, 516 (2010).

[Diwald2004] Diwald O. et al., *J. Phys. Chem B* **108**, 6004 (2004).

[Kaspar2005] Kaspar T.C. et al., *Phys. Rev. Lett.* **95**, 217203 (2005).

[Livraghi2006] Livraghi S. et al., *J. Am. Chem. Soc.* **128**, 15666 (2006).